Formation and Stabilization of Pores in Bilayer Membranes: Induced by stress and Amphiphilic copolymers

DISSERTATION

zur Erlangung des akademischen Grades
Doctor rerum naturalium
(Dr. rer. nat.)

vorgelegt der

Fakultät für Mathematik und Naturwissenschaften der
Technischen Universität Dresden

von

Ankush Checkervarty
geboren am 27. Feb 1991 in Una, India

Leibniz-Institut für Polymerforschung Dresden e.V.
Dresden, 2018

Abstract

All organisms have cell membranes which are composed of lipids. The length of lipids affects the elastic properties of the cell membrane which play an important role in cell's survival. For instance, membrane flexibility controls the amount of stress that a membrane can sustain before pore formation. In the bacterial cell membranes, the pore formation is also induced by naturally occurring peptides and synthetic amphiphilic copolymers. For this reason, they are one of the most anticipated novel antimicrobial materials. Understanding the mechanism of their action is essential for their use against microbes. Using coarse-grained simulations and a mean field model, we study lipid bilayer membranes under the variation of stress and tail length, as well as their interaction with flexible amphiphilic copolymers.

We used a polymer brush model to describe the free energy of the membrane in terms of entropic contributions and hydrophobic interactions. As the stress is increased on the membranes, at high stresses, the membrane transits to a stable pore state in agreement with simulation results. The increased hydrophobic interaction energy at the interface at high stresses leads to the formation of a pore. The hydrophobic interactions induce a contraction stress and the entropy of lipid tails induces a repulsive stress on the membrane. The simulations show that the entropic contribution to the stress, at its positive values, decreases as the length of lipid tails is increased. This increases the tendency of the membrane with the longer lipids to withstand larger stresses before rupturing into pores, as the internal repulsive stress is reduced.

We show that copolymers can enhance the pore stability by decreasing the line tension due to the weak adsorption along the rim of the pore. The bilayers studied in our simulations do not require high copolymer concentration at the pores nor any self-organization of the copolymers to open the pore. This is in contrast to the commonly known barrel stave model where the copolymers are assumed to be strongly localised at the rim of the pore. In the presence of the copolymers, we observe a meta-stable pore state of membrane. This happens at a specific concentration of copolymers depending upon the stress acting on the membrane. If the concentration is further increased from this value, then, the membrane shifts to a stable pore state. An increase in the probability of pore formation is observed as the length of copolymers or stress on the membrane are increased. Both the solvent and copolymer permeability increase as the pore becomes stable.

Acknowledgements

I would like to express my gratitude to my supervisor Jens-Uwe Sommer for providing a professional, yet, informal environment nourishing scientific curiosity. I also gratefully acknowledge the help and support by all my colleagues, who have contributed in the successful completion of this work. I would like to thank Marco Werner, Hauke Rabbel, Olesksandr Dolynchuk, Markus Koch, Ron Dockhorn, Martin Wengenmayr, Jan Domurath, and Yachong Guo for fruitful discussions and for sharing their experiences and thoughts on various topics. I further thank Vladimir Baulin for hosting me in his group in Tarragona and for interesting discussions. A special thanks goes to Hauke Rabbel and Ron Dockhorn for creating the package LeMonADE, without which this work would not have been possible. I thank the Leibniz-Society and the SNAL Initial Training Network for financial support.

Contents

Abstract ii

Acknowledgements iv

1 Introduction 1
- 1.1 Composition of the membrane 3
- 1.2 Transport across membranes 4
  - 1.2.1 Protein channels 4
  - 1.2.2 Transport without protein channels 5
  - 1.2.3 Solubility-diffusion model 7
- 1.3 Model membrane systems and coarse-graining 12
- 1.4 Outline of the thesis 14

2 Simulating the lipid bilayers 17
- 2.1 Monte Carlo Simulations 17
  - 2.1.1 Bond fluctuation method 19
- 2.2 Lipid bilayers in BFM 20
  - 2.2.1 Hydrophobic Effect 20
  - 2.2.2 Self assembled bilayers 22
- 2.3 Bending Potential 24
  - 2.3.1 Phase transition in bilayers 25
- 2.4 Conclusion 29

3 Lipid bilayer membranes under stress 31
- 3.1 Stress and variation of area per lipid 31
- 3.2 Helfrich Model and Fluctuation Tension 33
- 3.3 Mechanical Tension 39
- 3.4 Comparison between the two tensions 44
- 3.5 Polymer brush model (PBM) 46
- 3.6 Solvent permeability and the stress 52
- 3.7 Conclusion 56

4 Interaction of lipid Bilayer Membranes with Amphiphilic Copolymers 59
- 4.1 Introduction 59
- 4.2 Simulation setup 65
- 4.3 Types of copolymers 65

4.3.1 Micellization of copolymers . . . 65
4.4 Polymer brush model with a pore . . . 69
4.5 Results and discussions . . . 71
4.5.1 Potential of mean force . . . 71
4.5.2 Size and probability of finding pores . . . 74
4.5.3 Distribution of polymers with respect to the pore centroid . . . 75
4.5.4 Average Solvent Permeability . . . 81
4.6 Conclusion . . . 82

5 Summary and Outlook 84
5.1 Summary . . . 84
5.2 Outlook . . . 86

Appendices 89
A.1 Chemical potential of bilayer as a function of stress . . . 89
A.1.1 Thermodynamic Integration . . . 89
A.1.2 Ghost Chain Method . . . 90
A.1.3 Chemical potential of bilayer . . . 92

Bibliography 95

List of Figures 107

List of Tables 115

Chapter 1

Introduction

Cells are the smallest living units of all the living organisms. For its survival, a typical cell has a membrane to separate its inside from outside, while allowing the transport of necessary molecules at the same time. The existence of the cell membrane has been known since the 19th century. The earliest identification of the cell membrane was suggested using the light microscope by Hartig, 1844 [1]. Later, in the second half of the 19th century, more evidence accumulated, pointing towards the presence of a membrane by the observation of the osmotic pressure. It was found to be generated by a membrane characteristic which restricts the passing of large molecules like sucrose but not small molecules like water [2, 3]. Overton, 1895 [4] suggested that the properties of the constituents of a membrane, i.e. lipids, are oil-like. This conclusion was made on the basis of the observation that the permeability of specific tested molecules depended upon their partition coefficient between oil and water. It took another 30 years to realize the bilayer structure of membranes through an indirect proof by Gorter et. al. 1925 [5]. The authors concluded that membrane exists in the form of a double layer with hydrophilic heads pointing towards the aqueous solution and hydrophobic tails from both layers pointing towards each other, Fig.(1.1). Even for inner cell organelles like the nucleus, the presence of nuclear membrane was already suggested by Brown, 1833 [6]. This was later confirmed with the experiments of Flemming, 1882 [7]. However, for the other organelles like mitochondria, Golgi apparatus etc. membrane was only found in the second half of 20th century because of the limitations of light microscopy. With the invention of electron microscopy in the 1930s, it was possible to get the resolutions in the range of 1 *pm*, whereas the light microscope's resolution is limited to only around 200 *nm*.

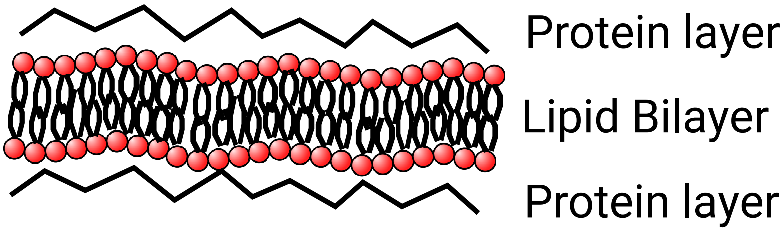

FIGURE 1.1 Scheme of the model for the cell membranes suggested by Robertson 1959 [8] and Danielli et. al. 1935 [9]. Adapted from Robertson 1959.

Fluid mosaic model

In 1959, J. D. Robertson [8] confirmed the double layer structure suggested by Gorter et. al. 1925 [5] using the electron microscopy. However, his description of the structure was similar to Danielli et. al. 1935 [9], in which he concluded that lipid molecules were sandwiched between two layers of proteins, Fig.(1.1). The proteins were assumed to align their hydrophilic parts towards the aqueous environment and hydrophobic parts towards the membrane.

This assumption of the structure was later disproved by Singer's group [10, 11]. In Singer et. al. 1972 [12], the final form of the fluid mosaic model was summarised, which is an accepted model to a large degree even today. Fig.(1.2) shows the major considerations in the model described in Singer et. al. 1972, which are:

- The membrane is a two dimensional fluid (no long-range orders) of phospholipids.
- Integral proteins are embedded in the membrane and phospholipids may interact differently (in a non-fluidic manner) with these proteins.
- Peripheral proteins are weakly adsorbed at the surface of the membrane.

Further in this model, the spatial structure of integral proteins was understood to be largely globular with some fraction of molecule forming alpha-helical conformations. In Singer et. al. 1972, the authors mention that immediately after the model was introduced, it was opposed by the scientific community of that time. The opposition was motivated by the contrast between the existence of a great diversity of membrane compositions in the different type of cells and the simplification suggested by the model [12].

The diversity of the different components of the membrane and their role in the transport of materials is discussed in section 1.1 and section 1.2. The section 1.3 explains how the simplification of membranes in various model systems along the lines of the *fluid mosaic model* helps in the understanding the function of these various components.

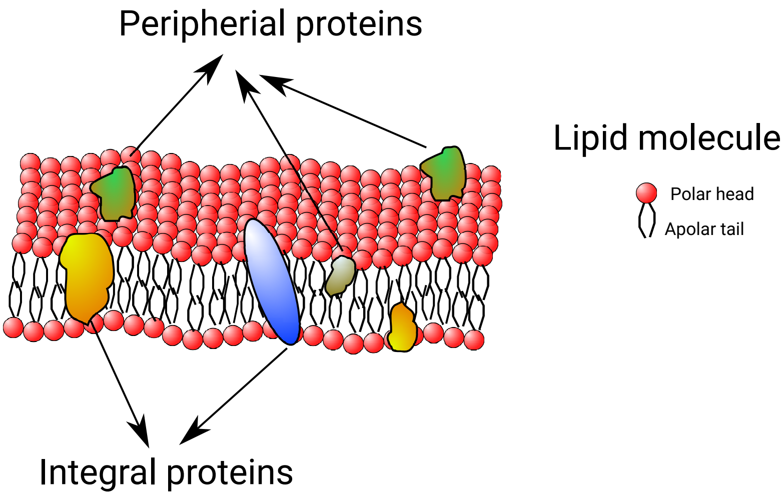

FIGURE 1.2 Schematic representation of the fluid mosaic model showing phospholipids and proteins. Inspired by Singer et. al. 1972 [12]

1.1 Composition of the membrane

The cell membrane contains several different kinds of molecules like phospholipids, sterols, ceramide glycolipids, gangliosides, proteins etc. These molecules are expected to play some role in the different functions that the membrane performs. The membranes on the average have 50% proteins and 50% lipids by mass, with tiny percentages of carbohydrates [13]. Furthermore, phospholipids are almost 50% of all the lipids in the membrane and 20% of them are cholesterols. These figures, however, only give a rough estimate. The composition of lipids can vary to a large extent, not only between two different organisms but even between two leaflets of the same membrane (for example, human red blood cell) [14].

In the basic structure of a phospholipid molecule, the head region contains a phosphate group, Fig.(1.3). This head group is attached to the oxygen of one of the alcohol sites of glycerol molecule via the phosphate group. There are two fatty acids attached to the other two alcohol sites of the glycerol molecule. The head region could be zwitterionic, anionic, or neutral depending on which group of atoms are attached to the phosphate group on the side opposite to glycerol molecule. The alkane part varies both in the number of double bonds and length. Some examples of these lipids have been shown in Fig.(1.3).

The composition of lipids is also controlled by environmental parameters like temperature and pressure in which an organism is grown. For example, the *bacillus subtilis*, which is a bacterium, can be grown at different temperatures (within the limits of its survival). The experiments show an increase in lipid tail chain length and degree of unsaturation with increased growth temperature [16]. The unsaturation of tails tends to increase the liquid-gel phase transition temperature of membranes. The deep sea

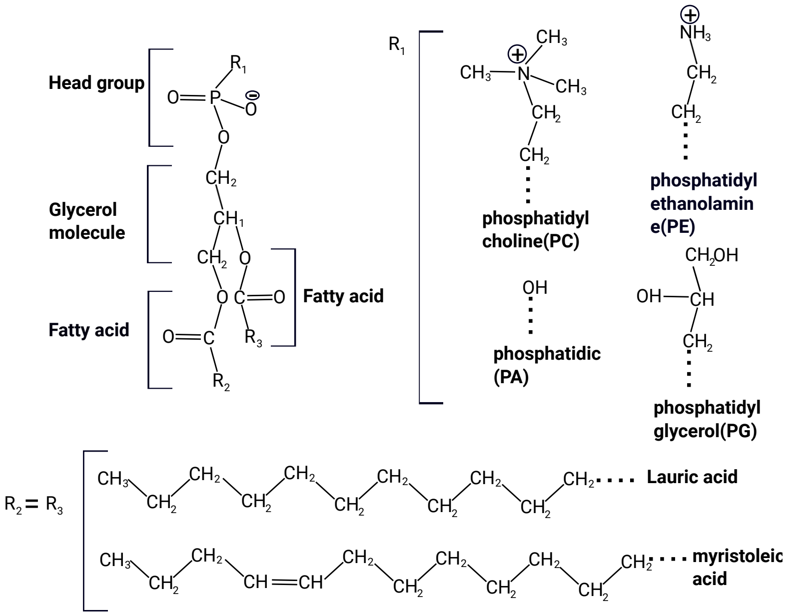

FIGURE 1.3 *Top left*: A typical phospholipid containing head group represented by R_1 connected with glycerol molecule and two fatty alkane chains, represented by R_2 and R_3 connected with other two alcohol sites of the glycerol molecule. *Top right*: Examples of typical head groups *Bottom*: Examples of typical alkane chains. A more detailed review of the structure of the phospholipids can be found in Heimburg 2007 [15].

bacterium adapt to increase the percentage of unsaturated lipid to cope with increasing hydrostatic pressure [17]. The environmental parameters like pH and the changes in the concentration of organic solvents like ethanol, acetone, etc. also affect the composition.

1.2 Transport across membranes

1.2.1 Protein channels

The fluid mosaic model, considers two types of proteins: peripheral and integral. The integral proteins predominantly assume an alpha-helical structure in the membrane. They help in the translocation of the ions, and other neutral molecules across the membrane. The various mechanisms of transport are described in the Fig.(1.4) and Fig.(1.6). The mechanisms by which these proteins translocate these materials have been classified as: active and passive transport. Passive transport occurs in which material is moved from the high concentration of the material to the low concentration. The active transport takes the material in the opposite direction of concentration gradient with the consumption of energy. For example, by the conversion of adenosine triphosphate (ATP) into ADP, oxidation or absorption of photons, Fig.(1.4) [18, 19].

In the passive transport, there are further two categories: (i) passive transporter proteins and (ii) ion channels. The passive transporter proteins change their conformation

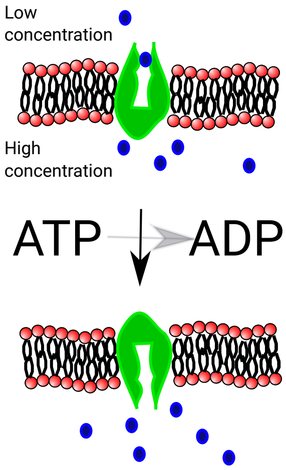

FIGURE 1.4 Active transport proteins working against the concentration gradients by consuming energy. Adapted from Demarche et. al. 2011 [19]

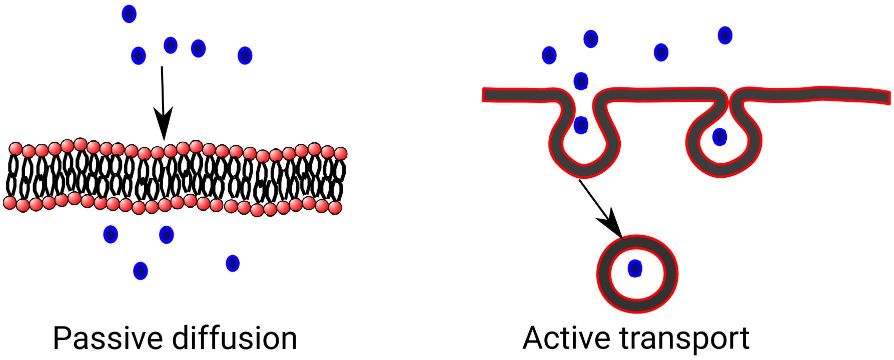

FIGURE 1.5 The schematic diagram of the cargo transport through a membrane without the protein channels. *Left Panel*: Passive diffusion *Right Panel*: Active transport. Active transport without protein channels include processes like endocytosis and exocytosis

to move the material from one side to the other, Fig.(1.6(a)). However, ion channels open and close a pore, depending upon types of ions which arrive on the surface. The ions, thus, pass through this pore. The different type of channels only let the specific type of ions to pass through. The ions can either reverse the potential across the membrane, Fig.(1.6(b)), bind to a ligand of a channel, Fig.(1.6(c)), or create mechanical stress, Fig.(1.6(d)), in order to pass through the membrane.

1.2.2 Transport without protein channels

Transport of materials through membranes can also occur without the protein channels. Similar to protein channels, the transport, here, can be categorised as active and passive transport. Passive transport of the small molecules like CO_2, O_2, N_2 and the large molecules like amphiphilic peptides can occur through phospholipid matrix without the consumption of any of the cell's energy, Fig.(1.5). The membrane generally acts as a

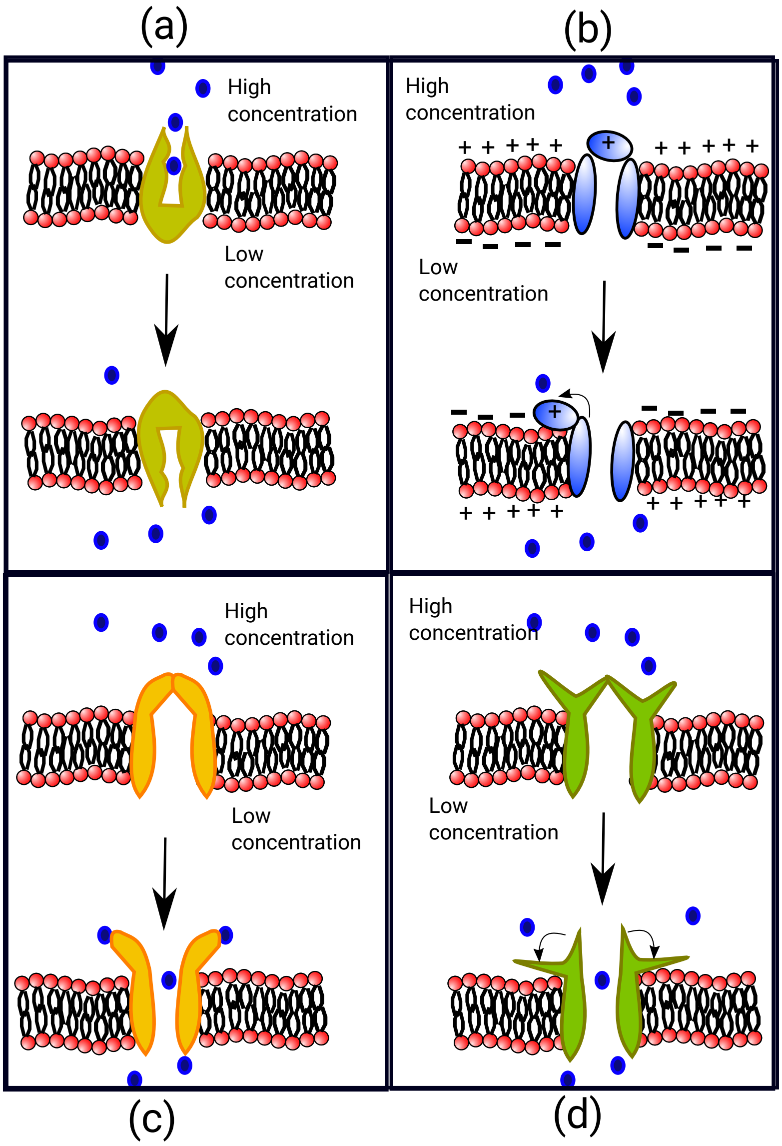

FIGURE 1.6 Passive transport in the direction of gradient (a) Passive transporter proteins (b) Voltage-gated ion channel (c) Ligand-gated ion channel (d) Mechanosensitive ion channel. Adapted from Demarche et. al. 2011 [19]

barrier for diffusion of materials through it, however, the small neutral gases like CO_2, O_2 etc. have substantial permeability rates. The small ions like K^+ and Na^+ can also transport, although their permeability rates through the phospholipids matrix are known to be comparatively lower than neutral gases [20]. The oligomers like peptides can transport by creating metastable or stable pores in the phospholipid matrix, Chapter 4.

Active transport through membranes without channels takes place by the processes like endocytosis or exocytosis, Fig.(1.5). In this, a lipid vesicle is formed which carries the material inside it, and then vesicle moves passively or actively using motor proteins.

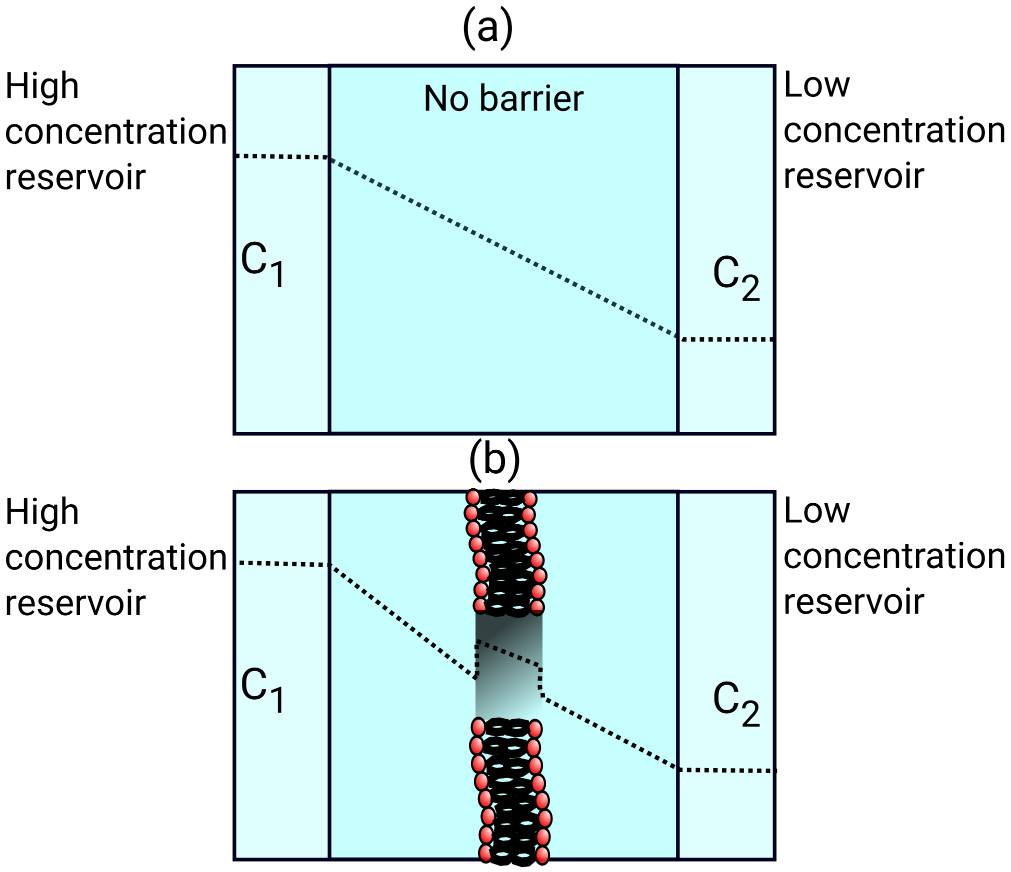

FIGURE 1.7 (a) The concentration profile in between two concentration reservoirs with no barrier in between them. (b) The concentration profile when a membrane like barrier is placed in between the reservoirs. The sudden jump in concentration profile at the membrane interface is theoretically explained by the adsorption of solutes at the interface. However, a more gradual increase has been observed in experiments.

1.2.3 Solubility-diffusion model

The *solubility diffusion model* is used to describe the transport across a generic lipid bilayer. The observations by Overton 1895 [4] and Meyer 1899 [21] that permeability of small solutes depended on their partition coefficient between oil and water lead to the proposition of this model [22–24]. The main assumption of the model is that a membrane is a homogeneous liquid layer of hydrocarbons (oil) sandwiched between aqueous solution. The process of permeability of a solute explained by this model as:

- The solute particles first dissolve into membrane on one side.
- Once dissolved, they diffuse through the liquid hydrocarbon membrane core.
- Finally, to complete the translocation, they dissolve back into the solvent environment on the other side.

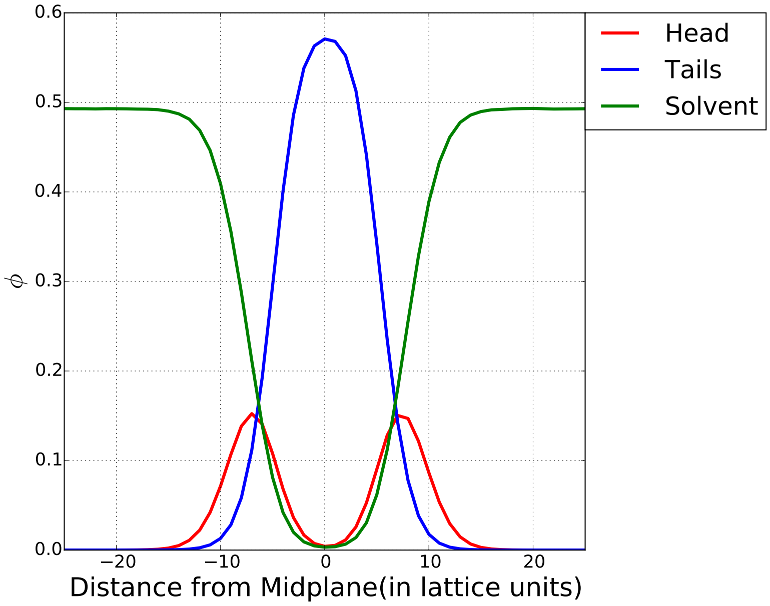

FIGURE 1.8 The density profiles of head, tail and water monomers in a self assembled membrane simulated using the bond fluctuation model, Chapter 2. The profiles are shown for a membrane at a tensionless state.

The rate of flow of any solute, j, through the membrane can be written as

$$j = P(c_1 - c_2) \tag{1.1}$$

where c_1 and c_2 are the concentrations of solute on the either side of the membrane. P is the permeability coefficient.

$$P = \frac{DK}{d} \tag{1.2}$$

where D is diffusion constant of solute in the hydrocarbon film, K is the partition coefficient of the solute between oil and water, and d is the thickness of hydrocarbon film. This model has been widely successful in explaining permeability in polymer membranes [25]. Similarly, a few applications of this model can also be found in experiments based on lipid membranes [26, 27].

The inhomogeneity of the membrane was realised by Diamond et. al. 1974 [28] using dimyristoyl lecithin vesicles in the nonpolar solvents. Furthermore, in Marrink et. al. 1994 [29], it was argued that the quantitative values of permeability from Eq.(1.2) satisfied experimental results only by the orders of magnitude. The contrast to the “homogeneous” assumption has been observed in many simulation studies [30](see Fig.(1.8)), and has also been verified experimentally [31]. A more generalised model was provided, in Diamond et. al. 1974 [28], which assumes the membrane as a heterogeneous medium. The Fick’s first law of diffusion in one dimensions states:

$$j_{fick} = -D\frac{\partial c}{\partial z} \tag{1.3}$$

where z is the Cartesian coordinate perpendicular to the membrane. Eq.(1.3) is valid for a particles diffusing in the homogeneous material. For example, in the case of solute diffusing between two concentration reservoirs, in Eq.(1.3), both D and j are constant, therefore the concentration will linearly decrease from higher concentration to lower concentration reservoir, Fig.(1.7(a)). To consider a variable (inhomogeneous) environment due of the presence of membrane, diffusion constant, D has to be modified as a function of z; $D = D(z)$, Fig.(1.7(b)). Secondly, a solute particle is subjected to a drift force, f_d, by thermal fluctuations from environment while performing a Brownian motion [32]. The drift force is a function of free energy, $F(z)$, varying along z,

$$f_d(z) = -\nabla F(z) \tag{1.4}$$

In one dimension, ∇ is equal to $\partial/\partial z$. The drifting solute goes through a large number of collisions from neighbouring molecules, which applies a frictional force, f_{fric}, against the drift force. This is a function of velocity of solute, v, acting in direction opposite to it.

$$f_{fric}(z) = -\xi v(z) \tag{1.5}$$

Considering the two forces on the solute described above, and Newton's second law:

$$m\frac{dv}{dt} = f_{fric} + f_d = -\frac{\partial F}{\partial z} - \xi v(z) \tag{1.6}$$

In an over damped regime, the acceleration is assumed to be zero

$$v(z) = \frac{1}{\xi}\frac{\partial F}{\partial z} \tag{1.7}$$

Finally, the flux of the solute considering the change in environment due to presence of membrane:

$$j_{mem} = v(z)c(z) = -\frac{c(z)}{\xi}\frac{\partial F}{\partial z} \tag{1.8}$$

The total diffusion flux of solute is the sum of concentration gradient, Eq.(1.3) and presence of membrane environment

$$j_{tot} = j_{fick} + j_{mem} = -D(z)\frac{\partial c}{\partial z} - \frac{c(z)}{\xi}\frac{\partial F}{\partial z} \tag{1.9}$$

Eq.(1.9) is the generally known as *Nernst-Planck equation*, if the free energy variation along z, $F(z)$, is generated by the electric field (applicable for ions and electrolytes). For the systems being discussed, the free energy variations occur due to the changes in the hydrophobic effect in the presence of the membrane. Since the hydrophobic effect along z does not change in the bulk solvent environment, and the changes in the free energy only start at the interface, it is reasonable to assume the free energy in the solvent medium as the reference, $F_\Delta = F(z) - F_{solvent}$. The partition coefficient, which is the ratio of miscibility between two mediums, namely membrane and water, should also be a function of z as the water density varies along z, Fig.(1.8). It is a function of the free energy,

$$K(z) = \exp(-F_\Delta(z)/k_BT) \tag{1.10}$$

Returning back to Eq.(1.9), the coefficient of friction force, ξ, is related to diffusion constant by Einstein's relation, $D = k_BT/\xi$. Thus, the Eq.(1.9) can be written as

$$j_{tot} = -D(z)\left(\frac{\partial c}{\partial z} + \frac{c(z)}{k_BT}\frac{\partial F_\Delta}{\partial z}\right) \tag{1.11}$$

For an ideal solution, the chemical potential, $\mu = \mu_{\text{ideal gas}} + k_BT\log(c)$. The ideal gas contribution come from the momentum part of the free energy, which is insignificant in an over damped system. In the solution, the presence of membrane, reduces the effect of the concentration gradient due to the demixing, which could be incorporated in chemical potential by

$$\mu = k_BT\left(\log(c(z)) - \log(K(z))\right) \tag{1.12}$$

Using Eq.(1.12), and Eq.(1.10), Eq.(1.11) can rewritten as

$$j_{tot} = -K(z)D(z)\frac{\partial(c(z)K(z)^{-1})}{\partial z} = -\frac{D(z)c(z)}{k_BT}\frac{d\mu}{dz} \tag{1.13}$$

The equation formed by the first two terms can be solved for the steady state, which means j_{tot} is not a function of z. Integration from the arbitrary point z_1 to z_2 in space:

$$\left(\frac{c(z_2)}{K(z_2)} - \frac{c(z_1)}{K(z_1)}\right) = j_{tot}\int_{z_1}^{z_2}\frac{dz}{K(z)D(z)} \tag{1.14}$$

If z_1 and z_2 are assumed to be in the solvent medium on the different sides of the membrane, then $K(z_1) = K(z_2) = 1$, as the $F_\Delta = 0$ in solvent medium. This makes the right hand side of Eq.(1.14), as just $(c(z_1) - c(z_2))$. Comparing with Eq.(1.1),

$$P = \left(\int_{z_1}^{z_2}\frac{dz}{K(z)D(z)}\right)^{-1} \tag{1.15}$$

Assuming $K(z) = const.$ and $D(z) = const.$ drives back the expression for homogeneous membrane environment, Eq.(1.2).

Four region model

In Marrink et. al. 1994 [29], using molecular simulations, it was confirmed that the assumption of homogeneous membrane environment is too rough to describe the real

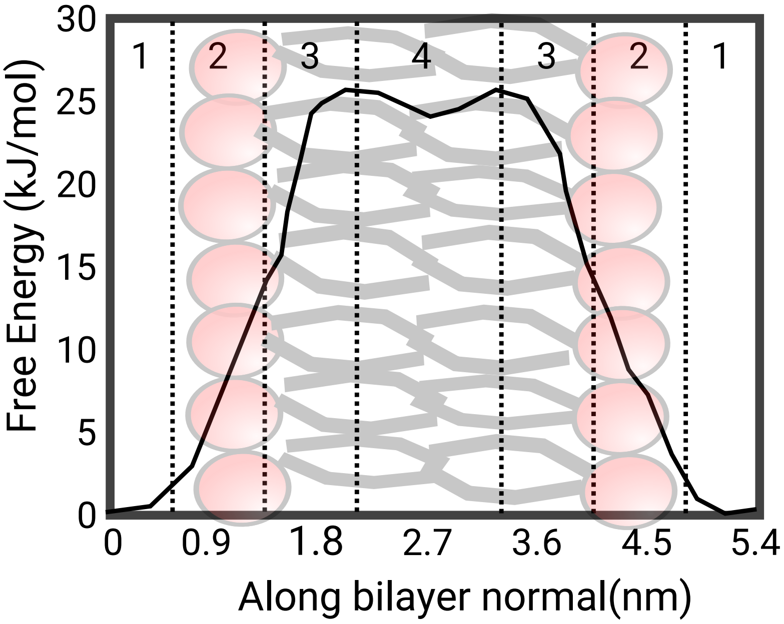

FIGURE 1.9 The four region model presented by Marrink et. al. 1994 [29]. The y axis represents the free energy of the water molecule at different positions normal to of membrane. Adapted from Marrink et. al. 1994 [29].

situation. The authors purposed a *four region model*, for the mechanism of permeation of small uncharged solute. Using Eq.(1.13), the authors calculated permeation rates of water in different regions, Fig.(1.9) and came to the following conclusions:

1. *Bulk solvent*: This region is insignificant for permeation unless the permeants are charged, like ions, etc. In the case of the charged molecules, they adsorb at the membrane surface and create a layer of $\sim 20\mu m$ at the interface, also called "unstirred layer" [33]. This layer exists even if the mechanical stirring is done on either side of the membrane and causes a potential barrier for the permeants to diffuse through the membrane.

2. *Bound solvent*: This region is characterized by high density of the head monomers and negligible but noticeable ($\sim 1\%$) water density. In this region, the diffusion of water is about 90% slower than in the *bulk solvent region.* The diffusion in this region involves breaking of strong water-water hydrogen bonds and making new hydrogen bonds with head monomers.

3. *High tail density region*: This region has the slowest diffusion of all the regions. With a high tail density, the chance of forming a hydrogen bond is not possible for the translocating water molecule. The only possibility of favorable hydrogen bonds is with the oxygen of the carbonyl group, see Fig.(1.3).

4. *Midplane low tail density region*: This region still has a low diffusion, however, it is slightly faster than region 3. There is a decrease in total normal pressure and an

increase in the lateral pressure which makes the tails more disordered and opens up more free volume pockets for the movement of solute.

Thus, this model provides a general picture of how a solute molecule diffuses through a lipid bilayer.

1.3 Model membrane systems and coarse-graining

In the previous sections, we discussed how components like the proteins channels, phospholipid matrix, unsaturated lipids, longer lipids etc. play an important role in the functions that a cell membrane performs. Generally, the diversity of the components of membranes, makes the mechanisms of the various functions of membrane complex. Simpler model systems have been created to separate the roles of these components in order to better understand the elementary mechanisms. Few examples of such model system are giant unilamellar vesicles (GUV), vesicles tethered to supported bilayers, bilayer tethered to solid support etc. Some of these membrane model systems have been extensively reviewed in Chan et. al. 2007 [34].

A GUV is a spherical container whose walls are made up of single species of lipids or a mixture of lipids, Fig.(1.10). Their size varies from a diameter of $1\mu m$ to $10\mu m$. GUVs have been predominately used to understand the phase behavior of binary and ternary lipid mixtures [35]. They are the key instruments to understand *lipid rafts*: small islands of liquid-ordered lipids in the bulk of the fluid-disordered lipids. Lipid rafts are believed to contribute to many membrane functions like signaling, trafficking etc. The existence of the rafts in the actual biological membranes is still discussed controversially among the scientists in the field. Even the studies, which suggest their existence, disagree on their size, lifetime and the other properties [36].

Another model system slightly more complex than GUV is the GUV with proteins. In the experiments, the only known way to study them is by extracting giant plasma membrane vesicles (GPMV) from the biological cell membranes [37]. These are the same membrane vesicles described in section 1.2, formed during endocytosis or exocytosis. For this thesis, the most relevant model systems are closely related to simple lipid GUVs or supported bilayer system, Fig.(1.10).

Coarse graining

Similar to model membranes, coarse-grained models have been used in the computer simulations to reduce the complexity of the biological membranes. Coarse-graining (CG)

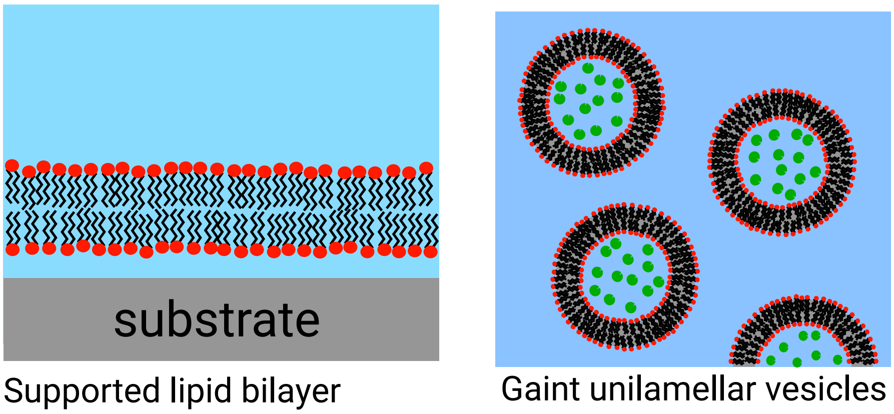

FIGURE 1.10 Schematic diagrams of model systems related to the thesis. These systems have been studied in fundamental experimental studies to simplify the membrane related problems. *Left Panel*: A supported bilayer with substrate. *Right Panel*: Unilamellar Vesicles. Source: Wikipedia (public domain)

is the removal of the atomistic details such that the relevant physics is reproduced and could be investigated. There are several approaches of coarse-graining. In a *bottom-up* CG approach, the atoms are systematically united into a single larger bead and at the same time effective potentials are constructed by appropriately averaging the detailed potentials. In *many body potential of mean force*, the many-body potentials arising from quantum mechanics are averaged using regression algorithms to save computation time. The *knowledge-based* CG uses a large amount of information collected in protein data banks. A generalized protein structure is constructed by statistically averaging many specific protein structures. In the *top-down* approach, the generalized potentials are parametrized without explicit considerations of atomistic details. The potential used in these models are not intended as well-defined approximations of the detailed physical system. An excellent review of all these approaches can be found in Noid 2013 [38].
For the present work, the approach of interest is the top-down (TDA). The interaction potentials in this approach are built on the basis of abstract physical principles. An example of such potential is the Lennard-Jones potential [39]. The models based on TDA have been widely successful in reproducing structural and thermodynamical properties of various biomolecular systems and especially the membrane systems. The macroscopic properties like self-assembly, interfacial tension, bending rigidity, translocation properties of polymers and nanoparticles etc. calculated using these models have provided useful insights to the details of these properties over the course of last two decades [38]. This approach addresses generic questions of the physics of many particle systems in which properties are dominated by cooperative behavior rather than the individual properties of the constituents.
An advantage of using TDA over the more detailed atomistic model is that longer time and space scales are reached. For example, Arkhipov et. al. 2006 [40] simulated a reovirus core which has a very high density of atoms. In their CG method, the authors

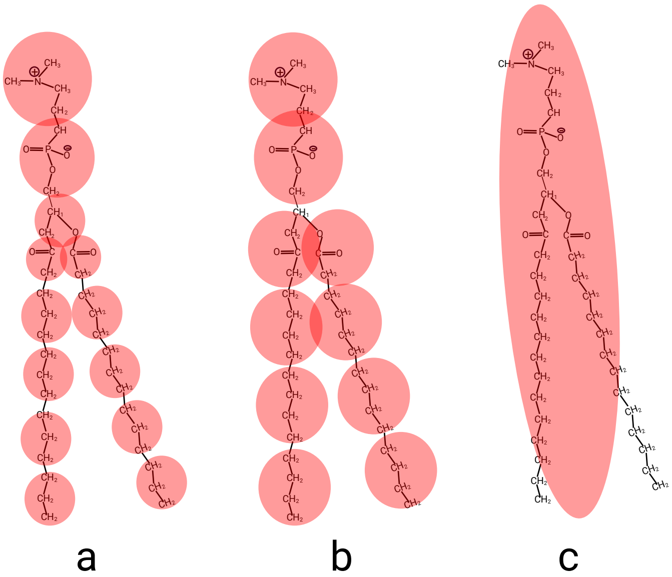

FIGURE 1.11 Coarse-grained model (a) by Shelley et. al. 2001 [41], absorbing $3CH_2$ into a single bead. (b) By Marrink et. al. 2004 [42] absorbing $4CH_2$ into a single bead. (c) By Ayton et. al. 2009 [43] absorbing all phospholipid into a single bead. Adapted from Ingólfsson et. al. 2014 [44]

were able to increase the integration step by 200 times in comparison with the all atomistic method. Recently, new hardware like Graphical Processing Units have been used for molecular dynamic simulations of fully detailed systems. These hardware speed the process up by about 10 folds, but it is nothing compared to speed boost using coarse-graining. A further point to note is that for specific problems, full atomistic simulations or quantum mechanical calculations are not even required. An example of such a property is self-assembly. For example, Ayton et. al. 2009, Fig.(1.11(c)) had one ellipsoidal bead for one lipid with an analytical potential. This structure was enough to observe self-assembly for their model system.

In this thesis, we coarse grain lipid bilayers based on TDA. This is implemented using the Bond fluctuation model and is explained in more details in the next chapter.

1.4 Outline of the thesis

In the chapter 2, a model for simulating lipid bilayer using BFM is explained. In section 2.3, an implementation of bending potential on the tails of membrane is described. The increasing strength of bending potential, leads to a phase transition in the membrane which is characterised by the bond order parameter. This is equivalent to gel-liquid phase transitions in GUVs in which the control parameter is temperature.

In the chapter 3, the section 3.1 describes changes in the various properties of membrane as the stress or length of tails of lipids are modified. The section 3.5 introduces a polymer brush model which takes in account the entropic and interaction contributions to a lipid bilayer.

In the chapter 4, the interaction of amphiphilic copolymers with the membranes at appropriate stresses has been described. The section 4.4 modifies the polymer brush model introduced in the section 3.5 to include a pore. The simulations results and interpretations of the results are summarised in the section 4.5.

Finally, the chapter 5 presents a summary of the results and the future perspectives.

Chapter 2

Simulating the lipid bilayers

This chapter provides a general literature review of the Monte Carlo (MC) methods, hydrophobic effect, and role of bending potential in molecular simulations and especially in lipid bilayers simulation. The bond fluctuation method (BFM) which has been used for performing the simulations in this work has been explained in section 2.1.1. The section 2.2 provides the model based on BFM used to simulate lipid bilayers. The section 2.3 provides an application of bending potential on the tails of lipid bilayers. The phase transition with the magnitude of the bending potential as the control parameter is described in section 2.3.1.

2.1 Monte Carlo Simulations

The basic aim of the MC method is to solve integrals by integrating over a random sample of points. For example,

$$I = \int_a^b f(x) \approx \frac{b-a}{S} \sum_{i=0}^{S} f(i) \tag{2.1}$$

where S is the total number of random sample of points between a and b. It can be easily realized that MC integration converges to a precise result as the number of points, $S \to \infty$. In the statistical mechanics, the dimensionality of the integrals depends on the number of the degrees of freedom. In a system of N particles with coordinates q and momenta p at temperature T, the canonical ensemble average of an arbitrary observable, A, can be found by [45]

$$\langle A \rangle = \frac{\int dp^N dq^N \exp(-\mathcal{H}/k_B T) A}{\int dp^N dq^N \exp(-\mathcal{H}/k_B T)} \tag{2.2}$$

where $\mathcal{H}$ is the Hamiltonian. The integral in the denominator is the partition function, $Z = \int dp^N dq^N \exp(-\mathcal{H}/k_B T)$. Since the kinetic energy, $K = p^2/2m$, has a simple quadratic relation with momenta, integral over momenta can be easily calculated and only integration over DN (D dimensional space) configuration space is required. However, even with this simplification, it involves a high computational cost to integrate even the systems as small as containing only 100 particles. The probability of a configuration, in general, with coordinate q is defined by

$$\mathcal{P}(q) = \exp(-U(q)/k_B T)/Z_q \tag{2.3}$$

where $U(q)$ is the potential energy at q and Z_q is the partition function with only contributions from the configuration space. Note here, $P(q) \to 0$ implies $U(q) \to \infty$. In the commonly studied systems, a large portion of the sample space has a little or negligible contribution to the integral in Eq.(2.2), because of its negligible probability (or high $U(q)$).

Therefore, for MC integration, instead of distributing points randomly all over configuration space, a better process would be to only consider the configurations which are most significant in the distribution of $\mathcal{P}$. This process is called *importance sampling*. First, an initial configuration is chosen which already has $\mathcal{P}(q_i) > 0$. Then any new configuration with q_n is accepted with a transition probability $\mathcal{T}(i \to n)$. Now, $\mathcal{T}(i \to n)$ has to be such that it prevents the visits to the configurations where $\mathcal{P} \to 0$. On the other hand, it should also preserve the equilibrium distribution of states, which is

$$\mathcal{P}(q_i)\mathcal{T}(i \to n) = \mathcal{P}(q_n)\mathcal{T}(n \to i) \tag{2.4}$$

known as the *Detailed balance* condition. There are many ways to choose $\mathcal{T}$, but one of the most effective and commonly used method is the *Metropolis criterion* [39]. In this criterion, $\mathcal{T}(i) = \exp(-U(q_i)/k_B T)$. Hence:

$$\mathcal{T}(i \to n)/\mathcal{T}(n \to i) = \mathcal{P}(q_n)/\mathcal{P}(q_i) = \exp(-(U(q_n) - U(q_i))/k_B T) \tag{2.5}$$

This choice of $\mathcal{T}$ satisfies both *Detailed balance* condition and makes the configurations with $\mathcal{P} \to 0$ to be visited less often. Additionally, $\mathcal{T}$ should also not exceed 1, therefore:

$$\begin{aligned} \mathcal{T}(i \to n) = \exp(-(U(q_n) - U(q_i))/k_B T) \quad & U(q_n) > U(q_i) \\ \mathcal{T}(i \to n) = 1 \quad & U(q_n) \leq U(q_i) \end{aligned} \tag{2.6}$$

Most general implementation of the Metropolis method generates a sequence of configurations which are correlated to each other. If the move from one to another configuration reflects the local physical movement of the system, then, the correlated configurations

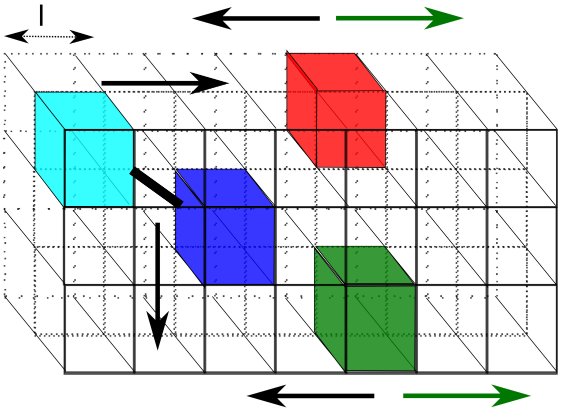

FIGURE 2.1 Schematic representation of monomers as cubes on a simple cubic lattice in the bond fluctuation method. The thick black line connecting the cubes represents a bond. The green arrows denote where moves are possible for a certain monomer on the lattice and the black arrows represent where they are forbidden because of one of the two constraints, i.e. either the bond vectors or the excluded volume.

are quite appropriate to study the dynamic properties of that system. There is a class of methods called *static MC* methods in which every new configuration is statistically independent of the old one. These are better if the objective of the study is just to find out the static properties of the system as decorrelation is not a problem. However, in the present work, we use a *dynamic MC* method which can be used to investigate both dynamic and static properties. In general, *dynamic MCs* can be performed by lattice models and off-lattice models. However, the lattice models are better in their computational efficiency. Time and length scale substantially longer than the single monomer length scale can be easily probed using lattice models. If in a specific system, the contributions from the scales comparable to the monomer scale are important, off-lattice models might be used. A more detailed review of static, off-lattice, and lattice models can be found in literature [46–48].

The lattice models have been used to simulate polymer chains. In the earliest lattice models which were used to simulate the polymer systems, there was one monomer occupying a single site on a simple cubic lattice. These models suffered from non-ergodicity in long self-avoiding walks [49]. Some configurations existed which were frozen. These configurations could not be accessed by any set of the random moves from any other configuration in the sample space. Bond fluctuation method helped in solving this problem as explained in the following.

2.1.1 Bond fluctuation method

The bond fluctuation method (BFM) was first introduced by Carmesian et. al. 1988 [50] in 2 dimensional lattice. It was further applied to 3 dimensional polymer mixtures by Deutsch et. al. 1991 [51]. A modification from the earlier lattice models in the BFM was that a monomer occupies a cube (8 lattice sites) in a simple cubic lattice, Fig.(2.1). It was shown by Carmesian et. al. 1988 [50] that BFM is ergodic and reproduces both the static and dynamic properties of polymer chains. The excluded volume in BFM monomers is realized by restricting a lattice site to only a single monomer. Another constraint is kept on the bond lengths between the monomers by restricting them to the value of $\sqrt{10}l$ or less (excluding $\sqrt{8}l$). Here, l is the lattice constant. These bond length restrictions in the simple cubic lattice generate a set of 108 bond vectors

$$\vec{b} \in \{P(2l,0,0), P(2l,l,0), P(2l,l,l), P(3l,0,0), P(2l,2l,l), P(3l,l,0)\} \tag{2.7}$$

where $P(a,b,c)$ denotes all the possible directions of bond vectors with the same magnitude, which is $\sqrt{a^2+b^2+c^2}$. In order to keep simulations ergodic, initial configurations have to be constructed in such a way that they include vectors either from $P(2l,2l,l)$ or $P(2l,l,l)$, but not from both sets, simultaneously. Thus, BFM preserves the computational efficiency of lattice models. At the same time, it also has features closest to any off-lattice model because of the larger set of bond vectors than the previous lattice models. In an elementary step, a monomer is randomly picked and it is checked if it is possible to move in either one of the 6 directions in $\vec{D}$,

$$\vec{D} \in P(l,0,0) \tag{2.8}$$

If new position (old position+$\vec{D}$) satisfies both the excluded volume and the new bond vector is in the set in Eq.(2.7), then the move is applied. Fig.(2.1) illustrates the mentioned constraints. The light bluish monomer on the top left on the lattice is forbidden to move in $D = (l,0,0)$ as it violates excluded volume and similarly, the dark blue monomer bonded with it cannot move $D = (0,l,0)$ because the new bond formed is not in the set in Eq.(2.7). Both red and blue monomers cannot move in $D = (-l,0,0)$ because of excluded volume and free to move in the $D = (l,0,0)$ as there are no constraints which are violated. Finally, a finite interaction energy could be also easily introduced using Eq.(2.6).

2.2 Lipid bilayers in BFM

2.2.1 Hydrophobic Effect

Hydrophobic effect is the tendency of hydrophobic substances (like hydrocarbons and lipophilic groups in solutes) to de-mix in an aqueous medium. It has been named as such because of the observation of the apparent repulsion between water and hydrocarbons [52]. The origins of this repulsion are not well understood but it is most commonly attributed to entropic forces. In a homogeneously mixed state of hydrocarbons with water, the water molecules do not form hydrogen bonds with apolar hydrocarbons. The entropy of the water molecules decreases due to the loss of hydrogen bonds. In order to minimize these water-apolar interactions, hydrocarbons form aggregates in water.

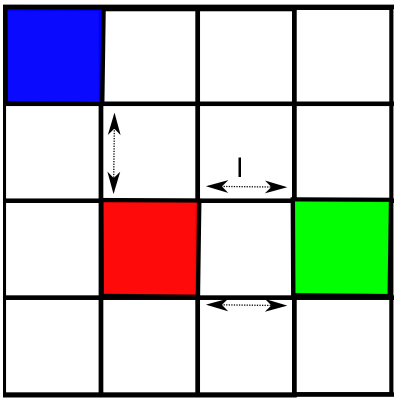

FIGURE 2.2 Schematic representation of the implementation of hydrophobic effect via nearest neighbour repulsion in a two-dimensional BFM. In this figure, the double-headed arrows represent the number of the nearest neighbour interactions between various monomers.

In this work, we realize the hydrophobic effect by implementing the nearest neighbor repulsion on the lattice between the monomers of the different species, for example, between lipid hydrocarbon tails and explicit solvent. The nearest neighbor repulsion implies that if one vertex from each of two monomer cubes are exactly one lattice unit away, they face an energy penalty of ϵ and similarly if two vertexes of these monomers are exactly one lattice unit away, they face double energy penalty, 2ϵ, etc. This is described in the schematic diagram of Fig.(2.2). In this figure, red and blue monomers have the potential energy of $U = \epsilon$ and red and green monomer have $U = 2\epsilon$. In principle, the position of any vertex of the cube can be assigned as a position of the monomer. In the three dimensions, the potential of interaction as a function of distance d between two monomers can be described by the following:

$$\begin{aligned} U &= 4\epsilon \qquad \text{for} \qquad d = 2l \\ U &= 2\epsilon \qquad \text{for} \qquad d = \sqrt{5}l \\ U &= \epsilon \qquad \text{for} \qquad d = \sqrt{6}l \\ U &= 0 \qquad \text{for} \qquad d > \sqrt{6}l \end{aligned} \tag{2.9}$$

In its first appearance, when the interaction energy was implemented in BFM, the value ϵ (instead of 4ϵ, 2ϵ etc.) was chosen for all the distances in Eq.(2.9). Moreover, an attractive potential was chosen ($\epsilon < 0$) [51]. The authors of this study concluded that only at the low values of ϵ, the simulation results could be explained. At stronger attraction potentials, the “blocking layer” of strong monomer contacts were formed at the interface, which their theory could not explain. The choice of an attractive potential also leads to artificial freezing on the lattice. Explicit solvent, with the repulsive interaction, takes care of many-body solvent effects (not possible with an implicit solvent).

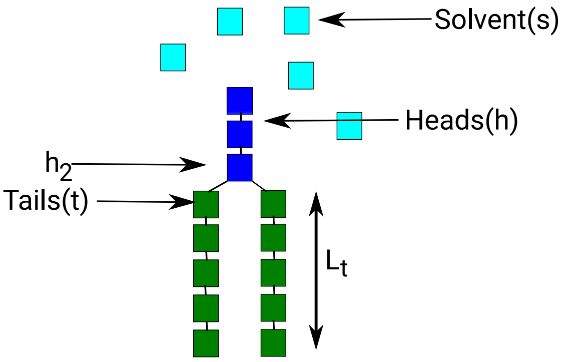

FIGURE 2.3 The schematic diagram of lipid structure showing 3 head monomers and two tails with 5 tails monomers each, $L_t = 5$, introduced by Werner et. al. 2012 [54]. The h_2 is the head monomer which is connected both the tails. This monomer is relevant for the discussion in section 2.3 and section 3.6.

It has been found to be important in some polymer system related studies [53]. Repulsive interactions ($\epsilon > 0$) of the potential scheme in Eq.(2.9) and an explicit solvent has been used to model and reproduce various properties of different polymer systems and lipid bilayer membranes [54–56]. This repulsion between solvent and a monomer of any substance (like polymer) can be scaled from 0 to some arbitrary value ϵ_0, to implement a hydrophobicity scale as described below. In the previous studies [54, 57, 58] and this work, this arbitrary value has been chosen to be

$$\epsilon_0 = 0.8 k_B T \tag{2.10}$$

This hydrophobicity scale between a monomer of species α and the solvent is characterized by H_α, thus,

$$\epsilon_\alpha = H_\alpha \epsilon_0 \tag{2.11}$$

$H = 0$ corresponds to a completely hydrophilic and $H = 1$ to a completely hydrophobic monomer. The interaction energy between some monomer α and monomer β is given by

$$\epsilon_{\alpha\beta} = \mid H_\alpha - H_\beta \mid \epsilon_0 \tag{2.12}$$

This scale is used in simulating the lipid bilayers in the following.

2.2.2 Self assembled bilayers

Self-assembly of amphiphilic lipids is the one of the most important property that a model for simulating bilayer should follow. There are some models which have successfully investigated various properties of the self-assembled amphiphiles using BFM

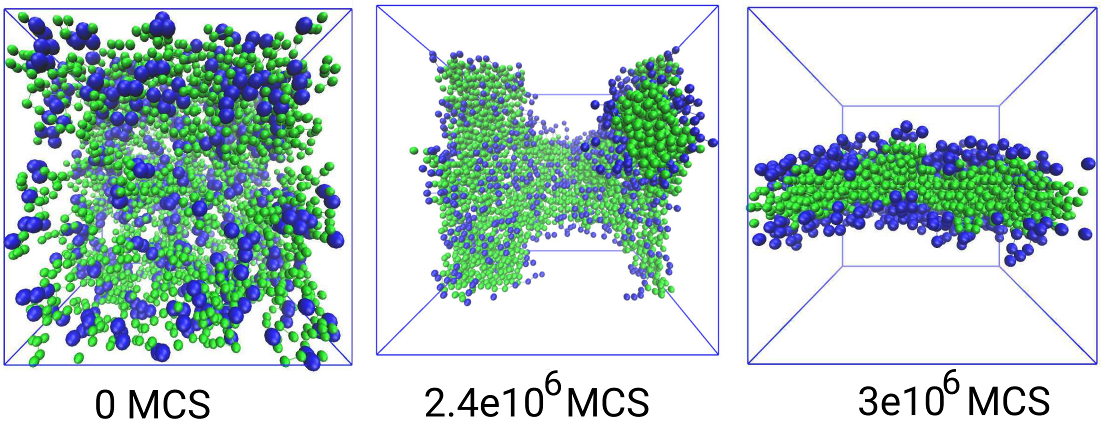

FIGURE 2.4 Simulation snapshots showing the self-assembly of 300 lipids into a bilayer at 3×10^6 MCS after starting with a random configuration at 0 MCS in a periodic box of $64l \times 64l \times 64l$. The solvent has been made invisible for convenience.

[59–61]. In this work, we use the model presented by Werner et. al. 2012 [54] for simulating membranes. The model has been used to study the interaction of the membranes with homopolymers [62], random copolymers [58, 63], triblock copolymer [64] and nanoparticles [57]. In all the previous works, the lipid molecule consisted of 3 hydrophilic head monomers and two hydrophobic tails with 5 monomers each, Fig.(2.3). The lipid molecule can be seen to have similar characteristics to the different coarse graining techniques shown in Fig.(1.11). Hydrophobic repulsion between tail monomer and the solvent is implemented using the equations in Eq.(2.9). The only interaction between head monomers and solvent monomers is the excluded volume (section 2.1.1). Any substance, which can interact with membranes, like a homopolymer or nanoparticles, can have different hydrophobicity ($H \in [0, 1]$) on a scale defined in section 2.2.1. The distribution of the head, tail monomers and solvent of an self assembled lipid bilayer can be seen in Fig.(1.8). In the first appearance of the model, Werner et. al. 2012 used this scale to simulate the homopolymers with monomers at different hydrophobicities. The authors studied the interaction of these homopolymers with the lipid bilayer. Werner et. al. 2012 concluded that homopolymers with monomers at $H_{trans} \simeq 0.68$, can pass through the bilayer with facing negligible free energy barrier. In other words, at H_{trans}, the membrane is transparent with respect to the homopolymers. The reason for the requirement of slightly more hydrophobic monomers $H > 0.5$ is attributed to a insertion barrier of the membrane that exists for large macromolecules like polymers. The results from simulations were able to reproduce the experimental properties and more detailed off-lattice simulations. It essentially points out that the model is sufficient for analyzing the physics of the lipid systems.

In this thesis, the simulations are set up by arranging lipids in the form of a bilayer and randomly placing the solvent as an initial configuration. The box is filled to the mean

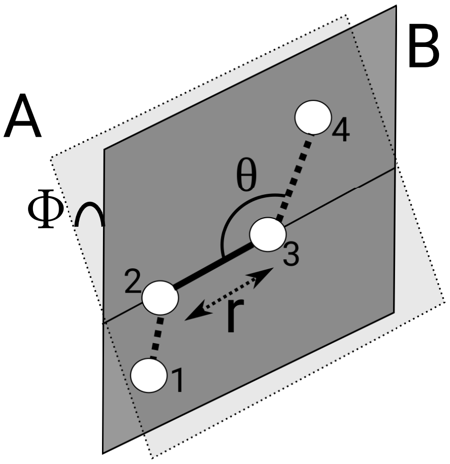

Figure 2.5 The geometry of a polymer chain molecule. Monomer 1 is on the plane A and monomer 4 is on the plane B, whereas monomer 2 and 3 lie on the line formed by the intersection of planes A and B. r is the bond length, θ is the bending angle formed by monomers 2, 3 and 4 and ϕ is the torsional angle formed by monomers 1, 2, 3 and 4.

lattice occupancy of 0.5, which is considered as a dense state in BFM. The volume of the box is maintained at, $V = 64l \times 64l \times 64l$. All the simulations are performed in the (N_{lipids}, V, T) ensemble unless mentioned otherwise.

2.3 Bending Potential

In the real molecules, several intramolecular bonding interactions are involved. The quantum mechanical calculations suggest restrictions on bending angles (θ), torsion angles (ϕ) and on bond lengths (r), see Fig.(2.5). In studying properties of many molecular systems, all the details of the angular potential are required, for example, *gauche* and *trans* angles in aliphatic chains, dihedral angles in azo-benzenes, synthetic molecular motors etc. The molecular force fields for simulating these systems are constructed using quantum chemical calculation along with the help of experimental data. More details on the field of molecular modeling could be found in literature [65–67].

The off-lattice coarse-grained models quite often use harmonic form of intramolecular potential [68–70]:

$$\begin{aligned} U(r)_{bond\ length} &= k_{bond}(r - r_0)^2 \\ U(\theta)_{bending} &= k_{bend}(\theta - \theta_0)^2 \\ U(\phi)_{torsion} &= k_{torsion}(\phi - \phi_0)^2 \end{aligned} \tag{2.13}$$

where k's are positive constants signifying the strengths of the potentials and r_0, θ_0 and ϕ_0 are the equilibrium values of the parameters, where the potentials have the minima. The potentials of form in Eq.(2.13) have successfully described the physical properties of linear polymers chains, fitting well with the experimental data [71–73].

These potentials are rarely used in the lattice-based models because of the finite choices of the bond angles. The bending potential, $U_{bending}$, in BFM has been used in some

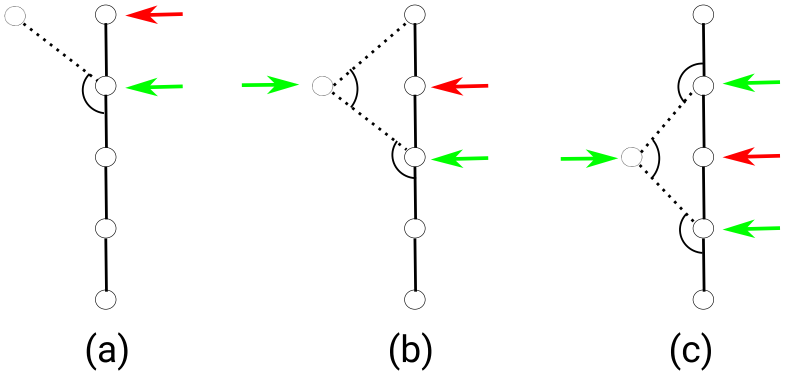

FIGURE 2.6 The implementation of the bending potential on a polymer chain in the MC simulations. Different bending angles are affected, depending on which monomer has been randomly chosen to be moved. (a) The monomer chosen is at the end of the chain. (b) The monomer chosen is at a position at one adjacent from the end of the chain. (c) The monomer chosen is neither at the position in (a) or (b). The red arrows show the chosen monomer and green arrows show the bending angles which would be affected.

occasions for studying the polymer systems. Bhawe et. al. 2004 [74], for the first time, used it to simulate the semiflexible polymer networks. Hsu 2014 [75] used the bending potential in long polymer chains ($N \sim O(10^4)$). They were generated in BFM with pruned-enriched Rosenbluth method to characterize their static properties. In these studies, the function of bending potential used was $U(\theta)_{bending} = k_{bend}(1 + cos(\theta))$. It has a minimum at π radians.

In this work, the conventional form of Eq.(2.13) for $U_{bending}$ has been used with $\theta_0 = \pi$. This choice makes the bonded monomers which are collinear to each other to have a minimum potential energy. This is described in the Fig.(2.6). For simplicity, let us assume the initial position of the chain to be linear. The calculation for energy penalty for a move depends on the random monomer's (which is supposed to be moved) position on the chain. Assuming that the randomly picked monomer is A. (a) If A is at the end of the chain, then only one bond angle has to be checked, which is formed by A and its two neighbors along the chain. (b) If A is present at the position one after the end, then two bonds have to be checked, one formed by A and its neighbors (shown by formed by dotted bonds) and the second one centered at the monomer adjacent to A. (c) If A is neither at the end nor one position after the end, three bonds have to be checked, one formed by A and monomers adjacent to A on of either side of A along the chain. This procedure has been used for discussion in the next section.

2.3.1 Phase transition in bilayers

In this section, a bending potential using Eq.(2.13) is applied on the tail chains with increasing strength, k_{bend}. In the real systems, increasing strength, k_{bend}, may represent

an increase in chain order, when the temperature is decreased, leading to a gel phase of membranes at low temperatures [15]. The typical temperature below which biological cell membranes transits into the gel phase is around 283-298K.
Generally, the balance between the strength of bending potential or θ_0, (Eq.(2.13)), and temperature plays a role in determining the phase of the membrane. For example, the chain ordering is disturbed by introducing unstaturation in the form of the *cis* state of acyl chains of lipid tails. Olbrich et. al. 2000 [76] in their experiments and Ollila et. al. 2007 [77] using their simulations, found a decrease in the chain order by increasing the number of *cis* bonds in the lipids of their bilayers, hence, a decrease in the gel-liquid transition temperature.

Simulation details

The following parameters are varied for membranes with length of tails, $L_t = 5$, see Fig.(2.3).

- $k_{bend} = 0$ to $k_{bend} = 7.8$ for $N_{lipids} = 300$

The choice of above parameters allows to observe the phase transition with respect to the control parameter of k_{bend} in terms of bond order parameter and fluctuations in internal energy.

Bond order parameter

The degree of orderliness of lipids tails can be calculated by tensor bond order parameter. The bond order parameter can be calculated using

$$\hat{Q}_{\alpha\beta} = \frac{1}{N_{lipids}} \sum_{i}^{N_{lipids}} (3o_{i\alpha}o_{i\alpha} - \delta_{\alpha\beta}) \tag{2.14}$$

α and β are direction components in Cartesian space. Here, o_i is the normalised orientation vector of lipids and δ is Kronecktor-delta. The calculation of o_i requires finding out the unit vector between the h_2 head monomer, Fig.(2.3), and the average of the lower most tail monomers, Fig.(2.7). The mean largest value of eigenvalue, λ_z (z component) of the matrix formed by $\hat{Q}_{\alpha\beta}$ is the measure of bond order parameter.

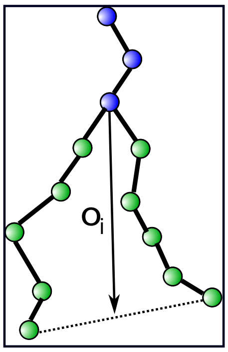

FIGURE 2.7 Schematic diagram showing the orientational vector used in Eq.(2.14).

Discussion

The primary indication of phase transition is the peak in fluctuations of internal energy which is calculated by adding the contributions from all the nearest neigbour contacts and the bending potential between the tail monomers. The fluctuations of internal energy, $\langle (U - \langle U \rangle)^2 \rangle$ is proportional to specific heat, c, by [45]

$$\langle (U - \langle U \rangle)^2 \rangle = k_B T^2 c \tag{2.15}$$

A peak in c is also observed at the second order phase transition of the ferromagnetic substances when the control parameter is temperature [45]. The increase in strength of bending potential, k_{bend}, is related to decrease in effective temperature. In another words, the effect of Brownian noise on the bending of tails is less prominent as k_{bend} is increased. Therefore, it is reasonable to assume that k_{bend} is a monotonically decreasing function of temperature ($k_{bend} \propto T^{-1}$). Fig.(2.8) shows the peak in internal energy fluctuations at $k_{bend} \sim 4.8 k_B T$. The value of k^P_{bend} symbolises the k_{bend} where membrane forms stable pore state. For the present system, $k^P_{bend} \approx 1.5 k_B T$. The phase transition occurs at $k_{bend} \gg k^P_{bend}$. The slope of c is discontinuous at $k_{bend} \sim 4.8 k_B T$, which implies that the second derivative of energy is discontinuous

$$\frac{\partial c}{\partial T} = \frac{\partial^2 U}{\partial T^2} \tag{2.16}$$

This points to a second order phase transition with respect to k_{bend}. A similar behaviour can be seen in the bond order parameter, Fig.(2.9). It jumps from $\lambda_z \lesssim 0.4$ to $\lambda_z \gtrsim 0.7$ in the small interval of $4 k_B T \leq k_{bend} \leq 5 k_B T$. This has a similarity with ferromagnetic phase transitions, where increase in the temperature leads to disorder in the spins of the molecules.

We note here, that, there might be artificial freezing effects (section 2.1.1) arising due to high k_{bend}. At high values, the snapshots show a negligible movement in the lipids. This is further characterised by the diffusion constant in Fig.(2.10) calculated using

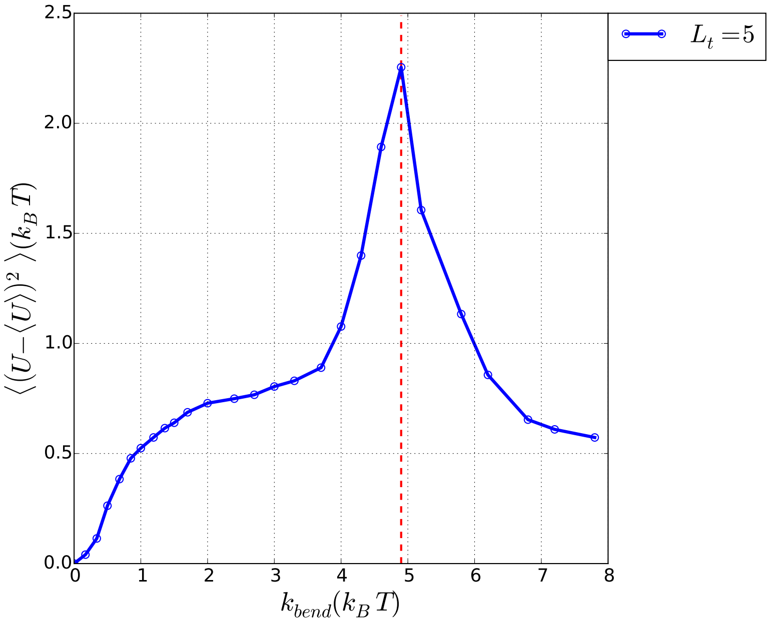

FIGURE 2.8 Variance of internal energy $\langle (U - \langle U \rangle)^2 \rangle$ as a function of bending potential magnitude, k_{bend}. The vertical red indicates the k_{bend} at which the phase transition occurs.

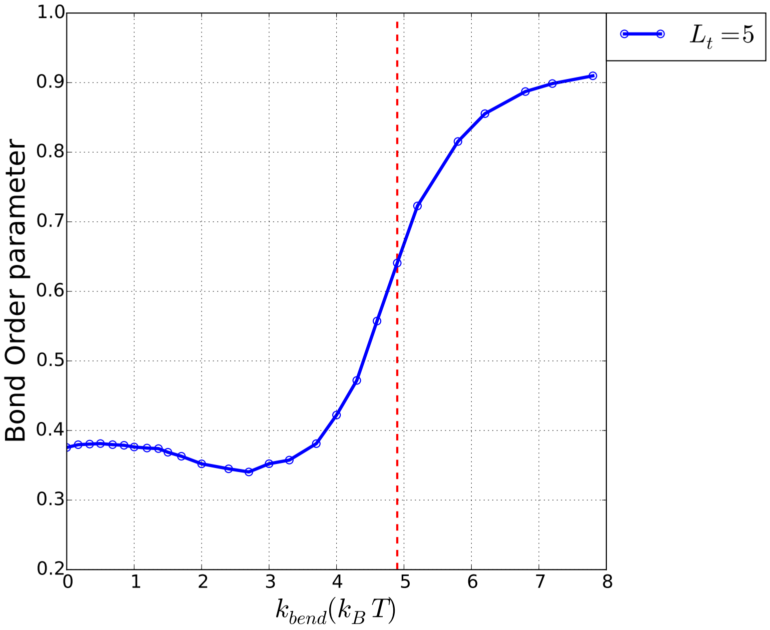

FIGURE 2.9 Bond order parameter as a function of bending potential magnitude, k_{bend}. The vertical dashed red line indicates the k_{bend} at which the phase transition occurs.

mean square displacements of lipids. The diffusion constant drops upto 10 times at $k_{bend} \gtrsim 4k_BT$ in comparison with the value at $k_{bend} = 0$. However, some degree of reduction in diffusion constant is also expected in the real systems [15]. A further investigation of these transitions using BFM might be considered in a future work.

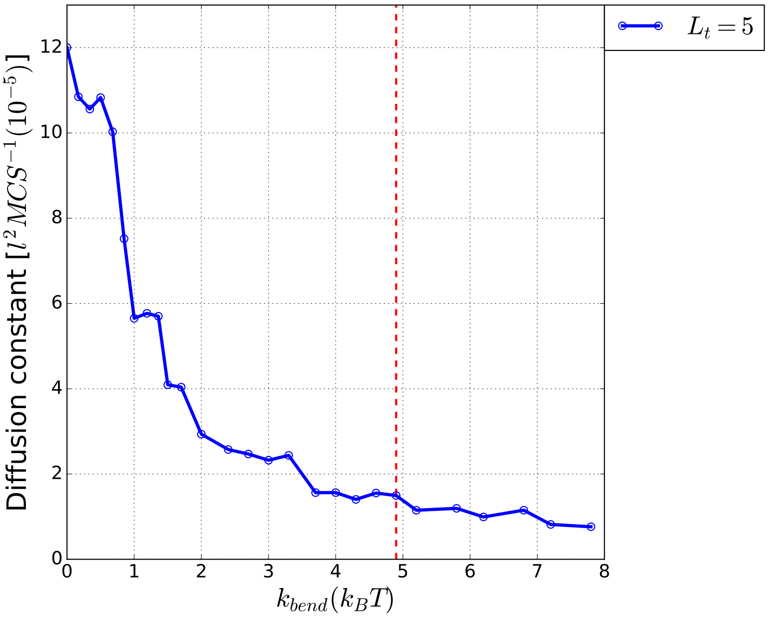

FIGURE 2.10 Diffusion constant of lipids as a function of bending potential magnitude, k_{bend}. The vertical dashed red line points indicates the k_{bend} at which phase transition occurs.

2.4 Conclusion

In this chapter, the model for simulating the membranes using the Bond Fluctuation model is introduced. A bending potential on the tails of lipid bilayer is implemented. The increase in the strength of the bending potential on the lipid tails leads to a liquid-gel phase transition. The strength of bending potential act as monotonically decreasing function of the temperature. The phase transition can be realised by changes in bond order parameter, fluctuations of the internal energy, and the diffusion constant.

Chapter 3

Lipid bilayer membranes under stress

In this chapter, the section 3.1 describes the generation of stress via the change of the number of lipids in the system in a constant area ensemble. The effect of lipid tail length on surface tension related to surface undulations is described in section 3.2 and surface tensions related to the stress tensors is described in section 3.3. The section 3.5 describes a simple polymer brush model which represents bilayer membranes by assuming tails of lipids as ideal polymer chains. The section 3.6 describes the solvent permeability and membrane thickness of membrane at different stresses and length of tails. Finally, all the results have been summarised in section 3.7.

3.1 Stress and variation of area per lipid

The stress plays a vital in role in the changes of the properties like shape, movement, fusion and fission of biological membranes [78, 79]. In simpler systems like lipids vesicles, the stress depends on the difference in the osmotic pressure on either side of the membrane [80, 81]. The lipid vesicles have been studied as tools of the drug delivery. There are characteristics of a vesicle, which determine its efficiency in drug delivery. For example, the encapsulation efficiency of the vesicle, its size, and its stability. These properties further depend upon the structure of lipids that form these vesicles [81]. As already discussed in section 2.3, the unsaturation of the lipid tails decreases the gel-liquid transition temperature. The length of tails has been found to affect the membrane's bending rigidity, area compressibility, rupture strength etc. and the response to changes in stress [82]. In the following, we analyse and study these properties of the membrane.

Simulation details

In the simulations described, a box of dimensions $64l \times 64l \times 64l$ periodic in all direction is chosen. The following parameters are varied:

- $N_{lipids} = 284$ to $N_{lipids} = 350$ for $L_t = 4$
- $N_{lipids} = 250$ to $N_{lipids} = 330$ for $L_t = 5$
- $N_{lipids} = 220$ to $N_{lipids} = 300$ for $L_t = 7$

This choice of the above range of N_{lipids} allows an access to three states (described below) which a membrane can achieve by varying the area per lipid enforced by the frame, a_f. For a bilayer in our simulations, it is defined as:

$$a_f = 2A_f/N_{lipids} \tag{3.1}$$

where A_f is area of frame to which the membrane could be supposed to be attached to, given by periodic simulation box. In the simulations presented here, we set $A_f = (64l)^2$. The factor 2 in the numerator arises because of the presence of two monolayers. At low value of N_{lipids} (or high a_f) a membrane with pores is present, Fig.(3.1)(a), and at high value of N_{lipids} (or low a_f) the buckled state is present, see Fig.(3.1)(c). At a certain moderate value of N_{lipids}, a *tensionless state* can be found Fig.(3.1)(b), where the change in the free energy with respect area per lipid, a_l,

$$\gamma = \partial F/\partial a_l \simeq 0 \tag{3.2}$$

vanishes. Typically, in simulations based on lipid membranes, tensionless membranes are used [54, 62–64]. The most commonly used parameter for controlling the tension in the membranes is a_f. An ideally flat membrane is defined by the relation, $a_f = a_l$ (a_l is area per lipid). A membrane in the buckling state can have a region where the surface makes an angle θ with the plane of frame, Fig.(3.2). The relation $a_l = a_f \cos(\theta)$ is followed in that region. If the membrane is in the pore state, then, $a_l = a_f - 2A_p/N_{lipids}$ (A_p is the area of the pore).

Two types of surface tensions are described in the sections below. The surface tension arising from the out of plane fluctuations of membrane is called *fluctuation tension* and the tension calculated from the stress tensor is called the *mechanical tension*. The comparison in between these two tensions will be discussed in the section 3.4.

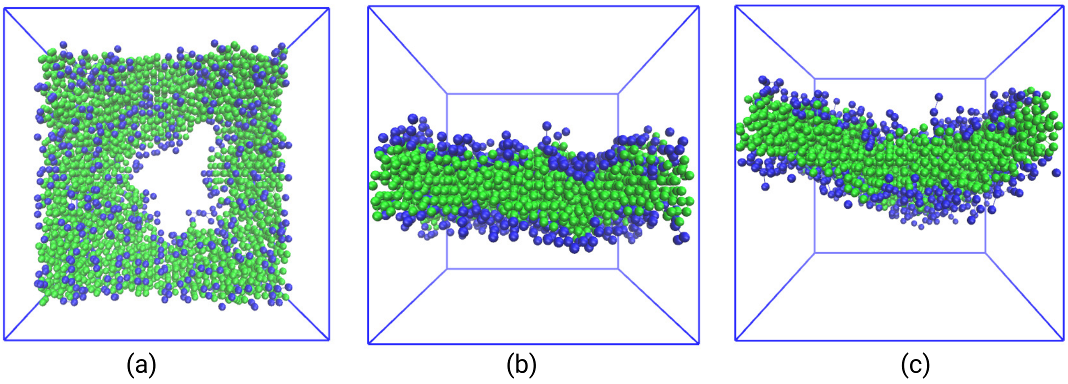

FIGURE 3.1 Simulation snapshots showing different states that membrane can assume depending on N_{lipids} in a constant projected area. (a) $N_{lipids} = 250$ (b) $N_{lipids} = 318$ (c) $N_{lipids} = 330$. Length of tails, $L_t = 5$. The solvent is not shown.

3.2 Helfrich Model and Fluctuation Tension

The surface tension plays an important role in determining the magnitude of out of plane thermal fluctuations of membranes (undulations). This was first realized in a study of egg lecithin bilayers by Helfrich et. al. 1984 [83]. In this study, the dependence of undulations of such membrane on their surface tension was successfully explained in analytical terms. It was an extension of the model previously put forward by Helfrich 1978 [84] in which curvature elastic energy density per area, h, in the terms of principle curvatures is defined as

$$h = \kappa \left(C_1 + C_2 - C_0\right)^2 /2 + K_s C_1 C_2 \tag{3.3}$$

where C_1 and C_2 are the principal curvatures of the surface. The curvature is defined by the inverse of radius, $C = 1/R$ of the circle made by two points infinitesimally close to every point (total three points) on a surface or a 2 dimensional curve, Fig.(3.2). The principal curvatures are inverse radii of the circles in the direction of eigenvectors of the shape operator [85]. The bending rigidity is represented by κ and the saddle splay modulus by K_s. The *Gauss-Bonnet theorem* states that $\oint dA\ K_s = 4\pi(1-g)$, where g is genus of the surface. Thus, for infinite membranes (no boundaries) and closed vesicles ($g = 1$), the integral $\oint dA\ K_s C_1 C_2 = 0$. It is, however, important to consider the integral in the case of the pores and point defects [83]. For the calculation of the total Hamiltonian, the second term can be neglected. All the membrane systems without any pores simulated in BFM satisfy this condition. The periodic boundaries make the membranes act as closed surfaces without any boundaries. The constant, C_0, is the spontaneous curvature. Its finite value would indicate asymmetry in two leaflets of the bilayers. The asymmetries which influence C_0 are, for example, different lipid composition, lipid concentration and the difference in the solvent medium facing

FIGURE 3.2 The schematic representation of the surface and the local angles it forms with xy plane. The R_1 and R_2 are the radii of two circles formed by the surface at an arbitrary point along the principal directions which are x and y axis in this case. The dotted circle is perpendicular to the plane of the paper. The tangents along these directions are denoted by red arrows. The θ is the angle formed by the local surface tangent with xy plane.

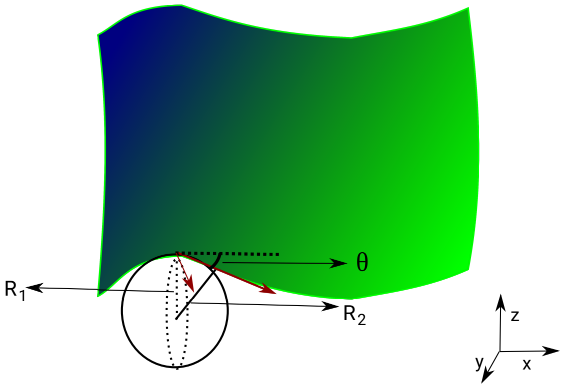

different leaflets of membrane etc. [83]. However, in the BFM membranes, both leaflets are generated symmetric, thus $C_0 = 0$ is used for our calculations. Hence, the total curvature elastic energy is

$$\mathcal{H}_{curv} = \int dA \ \kappa \left(C_1 + C_2\right)^2 /2 \tag{3.4}$$

To estimate the surface tension, the amplitudes of different modes are considered. The area of the surface should be much larger than the area per lipid, i.e. $A_f \gg a_l$. A surface could be defined in terms of $Z(x, y)$, where Z is the height of the membrane in z direction as a function of coordinates $\mathbf{r} = (x, y)$. It is assumed that the deviations from the flat membrane are small.

$$|\nabla Z(x, y)| \ll 1 \tag{3.5}$$

which simply implies $\partial Z/\partial x \ll 1$ and $\partial Z/\partial y \ll 1$. The value of $Z(\mathbf{r})$ could be decomposed into the different wave modes using *Fourier transform.*

$$Z(q) = \sum_r Z(r) \exp(-i\mathbf{r} \cdot \mathbf{q}) \tag{3.6}$$

In Eq.(3.6), $\mathbf{q} = (2\pi/L_b)(n_x, n_y)$, where L_b is the length of the simulation box, which is assumed to be equal in both x and y direction ($L_{bx} = L_{by} = L_b$). n_x and n_y are both equal sets of natural numbers which belong to the interval $[0, \lfloor L_b/b \rfloor]$. Here, b is the number of the bins in which surface is discretized for the fourier transform. For calculating the value of $Z(r)$ in each of these bins, z component of the center of mass of all the lipid monomers including heads and tails in a certain bin ($b_{xy} = b_{xy}(x, y)$) is calculated.

$$Z'_{b_{xy}} = \frac{1}{N_{b_{xy}}} \sum_{i=0}^{N_{xy}} \mathbf{R_{b_{xy}}} \cdot \mathbf{z} \tag{3.7}$$

Here, $\mathbf{R_{b_{xy}}}$ is the position vector of an arbitrary lipid monomer in bin, b_{xy}, and N_{xy} is the total number of lipid monomers in that bin.

The BFM membranes always have some diffusion in z direction (direction normal to the plane of membrane). To remove the effects of this translational motion from the $Z'_{b_{xy}}$, it is measured in the frame of reference of centre of mass of the membrane.

$$Z_{COM} = \frac{1}{N_{\text{monomers}}} \sum_{i=0}^{N_{\text{monomers}}} \mathbf{R} \cdot \mathbf{z} \tag{3.8}$$

Here, N_{monomers} is the total number of lipid monomers present in a membrane. Therefore, $Z_{b_{xy}} = Z'_{b_{xy}} - Z_{COM}$ is the Z value used for the *fourier transform*. Furthermore, the boundaries in z direction are periodic. This leads to erroneous results of centre of mass values in both Eq.(3.7) and Eq.(3.8), in the configurations where the membrane is close to any boundary in z direction ($z = 0$ and $z = L_{bz} - 1$). To avoid such problems, a random monomer which is on the membrane is chosen as reference point, $\mathbf{r_{ref}}$. Then, the centre of mass is calculated using

$$Z_{COM} = \mathbf{r_{ref}} + \frac{1}{N_{\text{monomers}}} \sum_{i=0}^{N_{\text{monomers}}} (\mathbf{R} \cdot \mathbf{z} - \mathbf{r_{ref}} \cdot \mathbf{z}) \bmod L_{bz} \tag{3.9}$$

The expression in the summation calculates the distance of the closest periodic image of an arbitrary point, $\mathbf{R}$, from a reference point, $\mathbf{r_{ref}}$, in the z direction. Similar procedure is used calculate the Eq.(3.7).

Returning back to Eq.(3.4), which only represents the energy contributions from curvature elasticity of membrane. The undulations also change the local area where they occur, ΔA. We define γ_{fluc} as the surface tension, which is the energy per unit area. Consequently, energy change, h', due to ΔA is

$$h' = \gamma_{fluc} \Delta A \tag{3.10}$$

The area element could be reparamaterised using $dA = dxdy\sqrt{1 + (\nabla Z)^2}$. Using Eq.(3.5) and Eq.(3.10), the total Hamiltonian is written as [86, 87]

$$\mathcal{H} = \frac{1}{2} \int_0^{L_{bx}} \int_0^{L_{by}} dxdy \left(\kappa (\nabla Z)^2 + \gamma_{fluc} (\Delta Z)^2 \right) \tag{3.11}$$

where L_{bx} and L_{by} are the lengths of the simulation box in x and y direction respectively. Total Hamiltonian can be written in the terms of modes q, using Eq.(3.6) [87–89]

$$\mathcal{H} = \frac{1}{2} L_b^2 \sum_q (Z(q))^2 \left(\gamma_{fluc} q^2 + \kappa q^4 \right) \tag{3.12}$$

The equipartition theorem states that each independent degree of freedom contributes $k_B T/2$ to the internal energy. Each mode in Eq.(3.12) is independent, thus,

$$\left\langle Z(q)^2 \right\rangle = \frac{k_B T}{L_b^2 \left(\gamma_{fluc} q^2 + \kappa q^4 \right)} \tag{3.13}$$

In our simulations, we obtained $Z(q)$ using Eq.(3.6) and discretized form of $Z(r)$ from the Eq.(3.7) and Eq.(3.8).

The discretized version of membrane in Eq.(3.7) leads to artifacts first noticed by Cooke et. al. 2005 [90]. In this study, it was observed that one dimensional curve divided into b bins suppresses the value of $Z(q)$ from continuous version by a factor of $\sin(\pi n/b)/(\pi n/b)$. Thus, a correction to Eq.(3.13) reads

$$\left\langle Z(q)^2 \right\rangle = \left\langle Z_{\text{discrete}}(q)^2 \right\rangle \left[\frac{\sin(\pi n_x/b)\sin(\pi n_y/b)}{n_x n_y (\pi/b)^2} \right]^{-2} \tag{3.14}$$

Discussion

The bin size is chosen to be 4. The membranes are simulated for total of 1×10^7 MCS and $Z(r)$ was sampled every 15000 MCS.

The results of the fluctuation spectrum for $L_t = 4$ from the simulations are shown in Fig.(3.3). The modes with $q > 2\pi/w$ (w is the thickness of the membrane) related to the protrusions in the membrane [91, 92]. These modes have not been experimentally observed [93]. Furthermore, Eq.(3.14) only holds for modes with low $|q|$ [90]. Therefore, we only consider the modes $q \lesssim 2\pi/w \sim 0.3$. The value of $\left\langle Z(q)^2 \right\rangle$ for low q increases with decreasing a_f (see legend). This implies that the intensity of low frequency modes increase with the release of tension. Tensionless state exists at $a_{f,0} = 24.38 l^2$ (solid black line). At the values of $a_f < a_{f,0}$, the intensity of these modes increases furthermore with decrease of a_f.

Fig.(3.4)(a) shows the values of γ_{fluc} obtained from fitting simulation data with Eq.(3.13) and with the correction from Eq.(3.14). Note that, here, we only consider the values of a_f where membranes do not have pores. The pore state cannot be identified with γ_{fluc}, as the expression of free energy used for analysis, Eq.(3.4) is only valid for boundaryless membranes. The value of γ_{fluc} increases linearly with a_f. The tension that a membrane can bear before rupturing into pores is highest for the membrane with the longest tails. This has also been observed by Rawicz et. al. 2000 [82] in their experimental studies. The dependence of tension on L_t is more convenient to observe in the units of the area expansion with respect to tensionless state, $(a_f - a_{f,0})/a_{f,0}$, Fig.(3.4)(b). Additionally, the slope of curves in this representation gives the *area compressibility modulus*, K_A, which is the magnitude of resistance of a membrane against the expansion or compression. The values of a_f where tension is negative do not behave linearly with a_f. Thus, the slopes were calculated only using simulation data for $a_f > a_{f,0}$. The values of K_A, $a_{f,0}$ and $\partial\gamma_{fluc}/\partial a_f$ could be found in table 3.1. These values increase as the length of tails is increased. In the section 3.5, using the polymer brush model, this increase has been explained.

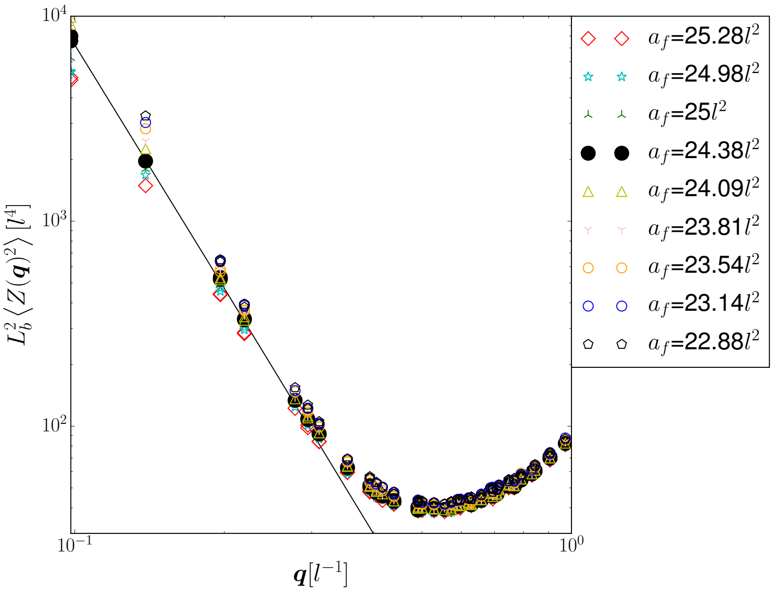

FIGURE 3.3 Spectral intensity, $\langle Z(q)^2\rangle$, as a function of wave number, $\mathbf{q}$, for different values of a_f. The legends are in order of decreasing a_f, thus, are also with decreasing stress. The tensionless state is at $a_f = 24.38l^2$ shown with black filled symbol, and the continuous black line shows the best fit of $\langle Z(q)^2\rangle$ obtained from simulation with the Eq.(3.13) at the tensionless state. The fit parameters give the values of $\gamma_{fluc} \simeq 0$ and $\kappa \simeq 1.3k_BT$. The value of γ_{fluc} and κ for different values of a_f can be found in Fig.(3.4) and Fig.(3.5) respectively. The length of tail has been chosen as $L_t = 4$.

The bending modulus is almost constant for $a_f > a_{f,0}$, but decreases at a_f where the tension is negative, Fig.(3.5). This decrease can be potentially explained by the increase in the intensity of low q modes, when the tension is negative, Fig.(3.3). A previous simulation study has also observed such behavior [94]. The bending modulus decrease due to the undulations has been suggested in analytical studies by Helfrich 1985 [95], L. Peliti et. al. 1985 [96] and K. Kleinert 1986 [97]. The average values of κ for all $a_f > a_{f,0}$ for different values of L_t has been given in table 3.1. The increase in the stiffness with the L_t has been reported by Rawicz et. al. 2000 [82]. The values of κ are, however, lower than the experimentally measured values from simple lipid membranes ($\sim 10k_BT$) [98]. The values obtained from our simulation belong to the lower bound of the spectrum of experimentally found values [99].

L_t	$a_{f,0}[l^2]$	$\partial\gamma_{fluc}/\partial a_f$ $[k_BTl^{-4}]$	$\kappa[k_BT]$	$K_A[k_BTl^{-2}]$
4	24.38	0.01	1.28	0.26
5	26.25	0.013	1.57	0.34
7	29.25	0.015	1.82	0.42

TABLE 3.1 The table showing the values of area per lipid enforced by frame at which tensionless state exists, $a_{f,0}$, slope of γ_{fluc} vs a_f curve, $\partial\gamma_{fluc}/\partial a_f$, bending modulus, κ, and area compressibility, K_A, for membrane with different L_t (see text).

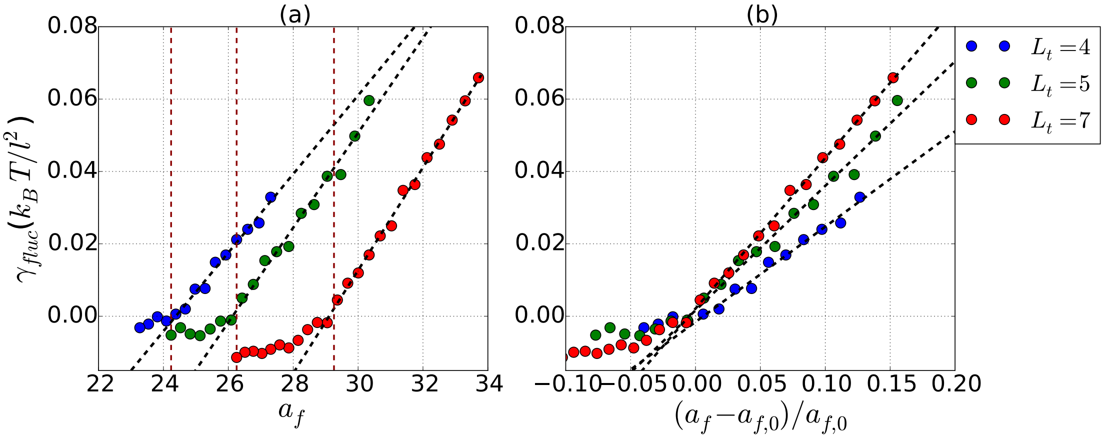

FIGURE 3.4 (a) Fluctuation tension as a function of area per lipid imposed by frame, a_f and L_t. The dark red vertical dashed lines point to the a_f where $\gamma_{fluc} \to 0$ (tensionless state), $a_{f,0}$. The black dashed line shows the linear behaviour of γ_{fluc} with a_f. The lines have been generated by least square fits for linear polynomial with the simulation data (only considering points which are $a_f > a_{f,0}$). (b) γ_{fluc} as a function of area expansion with respect to the tensionless state for each L_t respectively. The dashed black lines are best linear fits for all simulations the above the tensionless state. The magnitudes of slopes of these lines represent the area compressibility, K_A.

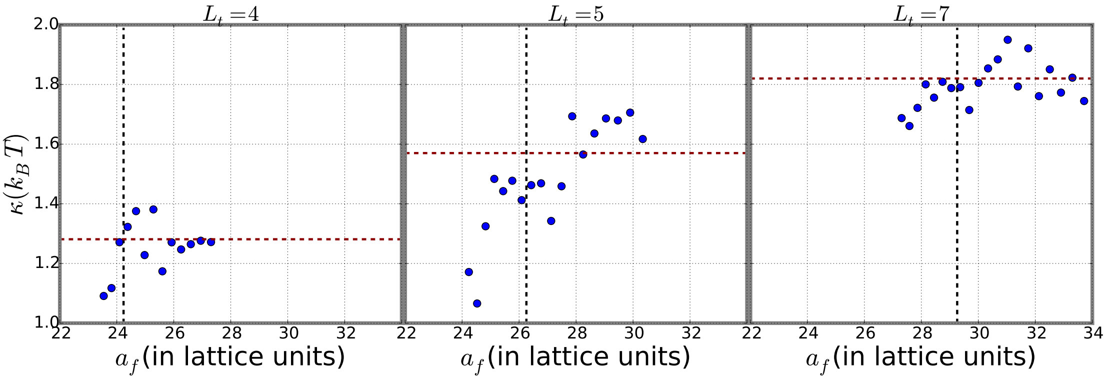

FIGURE 3.5 Bending rigidity, κ, as a function of the a_f for different length of tails, L_t. The black vertical dashed lines represent the tensionless state $a_{f,0}$. The horizontal lines represent the average of κ considering only points which are at $a_f > a_{f,0}$.

3.3 Mechanical Tension

The stress is defined as the force per unit area. The stress tensor for a system is defined as a tensor product, containing the contributions from kinetic energy and interaction energy, $\tau = 2\langle K \rangle + U$ [100, 101].

$$\tau = \sum_i m_i v_i \otimes v_i + \sum_{i>j} \frac{\nabla U_{ij} \otimes r_{ij}}{V} \tag{3.15}$$

where v is velocity, m is the mass of particles, V is the volume of the system. U_{ij} is the pairwise potential and r_{ij} is the distance between the particles i and j. Note, that the pairwise potential contains m-body contributions (with $m \geq 2$). However, in BFM membranes only nearest neighbor repulsion and bending potential have been implemented. Thus, we only consider the 2-body and 3-body terms. As the nearest neighbor interactions are short ranged, only bending potential contributes to the three body potential terms. In most simulation studies, the kinetic part of the tensor is neglected as its contribution is isotropic. Thus, the surface tension mainly depends only upon the interaction part [101]. In a three dimensional system, nine components are required to describe the tensor completely.

$$\tau = \begin{bmatrix} \tau_{xx} & \tau_{xy} & \tau_{xz} \\ \tau_{yx} & \tau_{yy} & \tau_{yz} \\ \tau_{zx} & \tau_{zy} & \tau_{zz} \end{bmatrix} \tag{3.16}$$

In τ_{ij}, the first index i represents the component of force acting on a body and j represents the orientation of the surface that it is acting on. For a fluid in equilibrium, τ_{ij} with $i \neq j$ vanishes as the stress in a direction other than normal to surface should be zero. We assume a membrane which is extended in xy plane and thus, has the normal in z direction. There is a translational invariance in xy plane, therefore, stresses in direction tangential to the membrane are equal, $\tau_{xx} = \tau_{yy} = \tau_t$ [102]. Thus, the stress tensor for the membrane is

$$\tau_{\mathbf{mem}} = \begin{bmatrix} \tau_t & 0 & 0 \\ 0 & \tau_t & 0 \\ 0 & 0 & \tau_n \end{bmatrix} \tag{3.17}$$

where τ_n is the stress along the normal direction of the membrane. Furthermore, the translational invariance in the xy plane implies that τ is only a function of z. The surface tension, γ_{mech}, for the system could be written as following [101, 102]

$$\gamma_{mech} = \int_0^{L_{bz}} dz\,(\tau_t(z) - \tau_n(z)) \tag{3.18}$$

where L_{bz} is the length of the simulation box in the z direction. The integrand is the stress profile defined as

$$\mathcal{S}(z) = \tau_t(z) - \tau_n(z) \tag{3.19}$$

Here, $\mathcal{S}(z)$ is the measure of the anisotropy in stress varying along the z direction. For example, if $\mathcal{S}(z) > 0$, it implies that the stress in the tangential direction is higher than the normal direction at z. Similarly, integrating $\mathcal{S}(z) > 0$ along the box in z direction gives a positive γ_{mech}. Thus, in this case, the total stress in the tangential direction is higher than in the normal direction for the whole system.
The macroscopic stresses τ_p can be derived from the microscopic component, T_p, by taking ensemble average [102]

$$\tau_p = \langle \mathrm{T}_p \rangle \tag{3.20}$$

where $p \in [t, n]$. The value of T_p is directly related to the interaction potential defined in Eq.(3.15). As already been discussed, we only consider 2 body and 3 body terms. To calculate the T_p in BFM, the space is divided into the slices in z direction of 2 lattice units and T_p is averaged over this slice to evaluate it as a function of z_s (coordinate of the slice) for two body potentials [102].

$$\mathrm{T}_p^{\{2\}}(z_s) = -\frac{1}{2V_{\Delta z}} \sum_{\langle j,k \rangle} \left(\nabla_j^p U^{\{2\}} - \nabla_k^p U^{\{2\}} \right) r_{jk}^p f(z_j, z_k, z_s) \tag{3.21}$$

$\sum_{\langle j,k \rangle}$ is the sum over all the possible pair of particles in the system. The value of r_{jk}^p symbolizes the distance between particle j and k in the p direction. $V_{\Delta z}$ is the volume of the slice. The function f has two cases: if one of the particle lies in the same slice as z_s and the other particle is in an adjacent slice, then, the value is given by $f(z_j, z_k, z_s) = 1/(2|z_j - z_k|)$. In the other case, if both particle lie in the same slice z_s, then, the value is $f(z_j, z_k, z_s) = 1$. Similarly, the three body potential dependent T_p can be written as [102]

$$\mathrm{T}_p^{\{3\}}(z_s) = -\frac{1}{3V_{\Delta z}} \sum_{\langle p,q,r \rangle} \sum_{\langle j,k \rangle} \left(\nabla_j^p U^{\{3\}} - \nabla_k^p U^{\{3\}} \right) r_{jk}^p f(z_j, z_k, z_s) \tag{3.22}$$

where $\sum_{\langle p,q,r \rangle}$ is the sum over all the possible triplets in the system. In BFM membranes, this sum is only done over bonded tail monomers and for the case when bending potential is applied. On the lattice, discrete form of $\nabla^p U$ for general particle is

$$\nabla^p U \simeq \frac{U(p+1) - U(p)}{p+1-p} \tag{3.23}$$

The above expressions for $\mathrm{T}_p^{\{2\}}$ and $\mathrm{T}_p^{\{3\}}$ are used in the Eq.(3.18) along with an ensemble average, Eq.(3.20). Thus, the mechanical tension, γ_{mech}, can be calculated.

Discussion

The simulations details for the time intervals are similar to the details mentioned in the section 3.2. The stress profiles here only have the contributions from the nearest neighbour interaction between the monomers. Fig.(3.6) shows different components of stress, $-\tau_n(z)$ and $\tau_t(z)$ at different a_f. A negative profile of τ_n is plotted in order to provide a comparison between two components which add up to give $\mathcal{S}$, see Eq.(3.19). The tendency of the lipid tails to minimize the hydrophobic contacts between solvent and tails leads to a contracting stress near the head region. Furthermore, there is a repulsive stress in bilayer core region due to the entropy of the tails (section 3.5). The relative changes in magnitude of stress along z can lead to different kinds of structures that the lipids self-assemble into, for example, micelles, vesicles or hexagonal phases [100]. In the lipid bilayer related experiments, measuring these profiles has been a difficult task, as the changes in stress profiles are too large within a small distances, 1-2 nm [100]. However, the simulation and analytical studies have investigated this problem in different conditions like in the presence of cholesterol, proteins and applied tension [101–103]. The small inset in Fig.(3.6) provides the results from molecular dynamic simulations of the Goetz et. al. 1998 [102] (at the tensionless state) for comparison, where the authors used Lennard Jones potential. A difference between stress profiles of membranes obtained with BFM and their method is visible at the midplane of the membrane. The profiles in Goetz et. al. 1998 have a value of zero at the midplane for τ_n and τ_t, which is not observed for the present model. The free energy barrier for solvent monomers in the case of our BFM is lower than in the simulations by Goetz et. al. 1998. The presence of a comparatively larger number of solvent monomers in the bilayer core leads to finite stress values at the midplane.

A positive area under the pressure anisotropy curve, $\tau_t(z) - \tau_n(z)$, for $a_f > a_{f,0}$, a negligible area at $a_f \simeq a_{f,0}$ and negative area for $a_f < a_{f,0}$ can be observed in Fig.(3.6). An enlarged plot for the same stress profiles have been provided in Fig.(3.7(a)). A positive $\tau_t(z) - \tau_n(z)$ profile implies that the contraction stress dominates the membrane. For $a_f > a_{f,0}$, the contraction stress due to the hydrophobic interactions is minimal at the midplane. For $a_f < a_{f,0}$, the repulsive stress dominates in the whole membrane, however, it is slightly lower in magnitude at the midplane. The positive and negative peaks at the bilayer-solvent interface represent the positive and negative interfacial tensions respectively.

Fig.(3.7(b)) shows the stress profiles near pore state stabilisation, $a_{f,\mathrm{pore}}$. This value represents the a_f, which is at the boundary of pore state and intact state. Thus, a slight increase in a_f in comparison with $a_{f,\mathrm{pore}}$ leads to stable pore state and slight decrease leads to stable intact state. The contraction stress at the midplane is considerably lower for a_f greater than but close to $a_{f,\mathrm{pore}}$, i.e. $a_f \gtrsim a_{f,\mathrm{pore}}$, in comparison with the stress

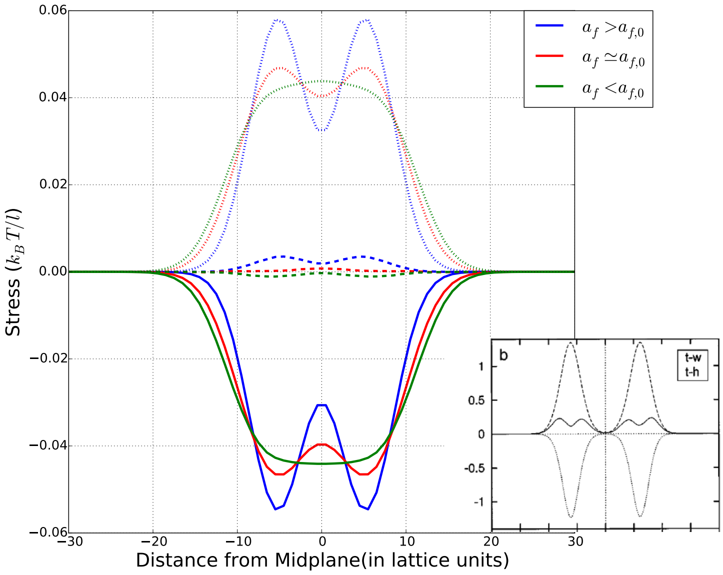

FIGURE 3.6 The stress profiles with different components, $-\tau_n$ and τ_t as a function of the distance from the midplane for $L_t = 5$ at different a_f compared to the tensionless state, $a_{f,0}$. The plots with dotted lines above x axis (positive) represent $-\tau_n$, solid lines below x axis (negative) represent τ_t and dashed lines in the middle represent a measure of anisotropy of the stress, $\tau_t - \tau_n$. The colors represent different tensions of the membrane. The blue color represents the membrane at a positive tension, $a_f > a_{f,0}$, red color represent the tensionless state, $a_f \simeq a_{f,0}$, and green color represent the membranes at a negative tension, $a_f < a_{f,0}$. The inset on right lower side shows results from molecular simulations by Goetz et. al. 1998 [102] available at http://www.mpikg.mpg.de for a tensionless state. This image shows the effect on stress profiles by considering Lennard Jones interactions between water-tail and tail-head monomers which is similar to nearest neighbour interaction in BFM.

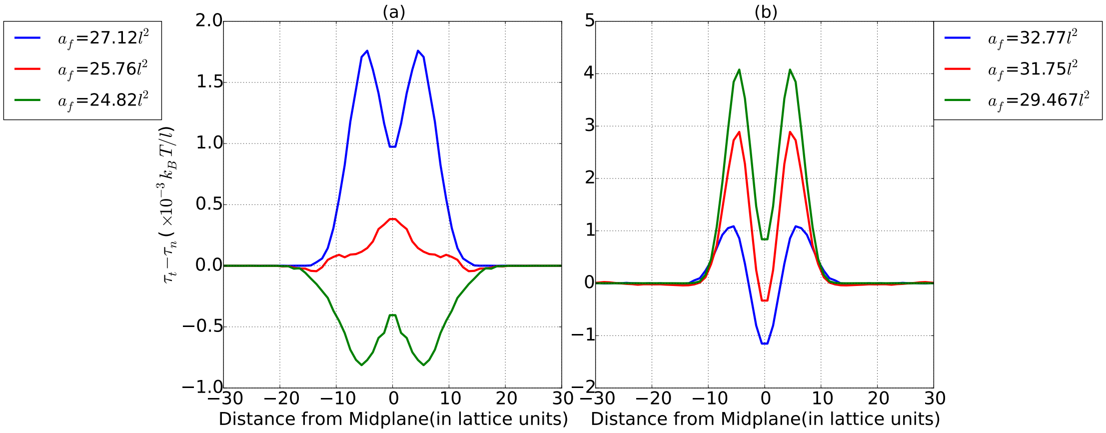

FIGURE 3.7 (a) $\tau_t - \tau_n$ profiles enlarged from Fig.(3.6) at different stresses close to tensionless state, here $a_f = 25.76l^2$ is tensionless state and thus, $a_f = 24.82l^2$ has a_f slightly smaller than tensionless state and $a_f = 27.12l^2$ is at the a_f slightly larger than tensionless state. (b) $\tau_t - \tau_n$ profiles close to the pore stabilisation state, $a_{f,\text{pore}}$(see text), $a_f = 31.75l^2$ is at $a_{f,\text{pore}}$, $a_f = 32.77l^2$ is slightly larger than $a_{f,\text{pore}}$ and $a_f = 29.467l^2$ is slightly smaller than $a_{f,\text{pore}}$

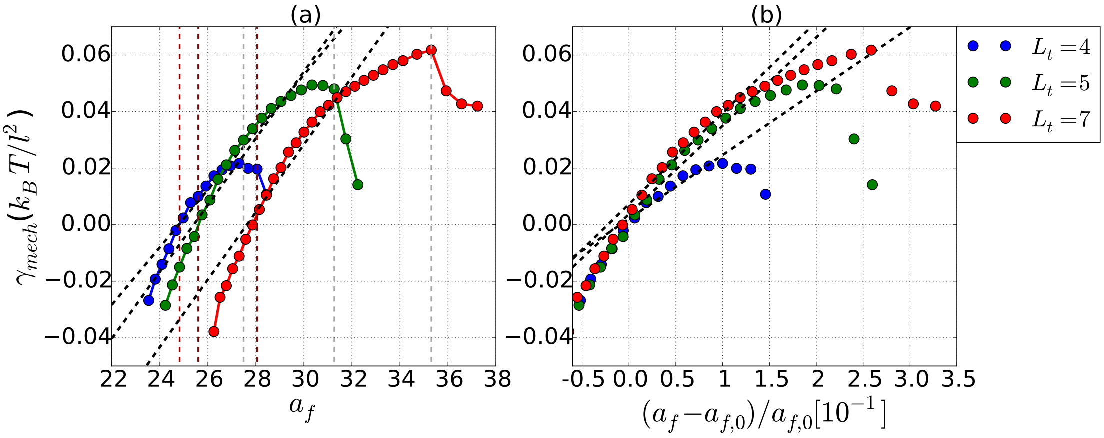

FIGURE 3.8 (a) The mechanical tension as a function of area per lipid imposed by frame, a_f, and L_t. The dark red vertical dashed lines points to the a_f where $\gamma_{mech} \to 0$ (tensionless state), $a_{f,0}$. The grey dashed line shows the area of pore state stabilisation, $a_{f,\text{pore}}$. (b) γ_{mech} as a function of area expansion with respect to the tensionless state for different L_t. The dashed black lines are best linear fits for all the points on x-axis as are considered in Fig.(3.4). The magnitudes of slopes of these lines represent the area compressibility, K_A.

profiles at $a_f \simeq a_{f,0}$, Fig.(3.7(a)). This happens as the probability of opening a pore is more likely at these values of a_f. The solvent occupying the pore induces a pressure towards the tails in lateral direction, which increases the repulsive interaction between tails. However, the total tension at this value of a_f is still positive because of the positive peaks at the interface. At $a_f = a_{f,\text{pore}}$, anisotropy of the stress at the midplane is almost negligible. Note that, $a_{f,\text{pore}}$ is characterised by the coexistence of the pore state and the intact state (without pores) within the range of natural thermal fluctuations of the system. This state will be discussed in more details in the next chapter. At $a_f > a_{f,\text{pore}}$, stable pore state is found, characterised by a more repulsive stress at the midplane. As explained earlier, the presence of the solvent in the plane of membrane, occupying the pore, leads to this observation.

The value of γ_{mech} for different L_t is shown in Fig.(3.8(a)). The pore state can be observed in the plots for all L_t, at $a_{f,\text{pore}}$ indicated by decreasing tension at values $a_f > a_{f,\text{pore}}$. The presence of the pore state is corroborated by sudden increase in the solvent permeability (see section 3.6) and snapshots from the simulation, as can be seen in Fig.(3.1). The net surface tension decreases as the total surface area reduces (by the pore area A_p) when the pore appears or stabilises. In Fig.(3.8(a)), the value of $a_{f,0}$ can be observed to highest for the membrane with the longest tails. Similar behavior is observed for $a_{f,\text{pore}}$. Fig.(3.8(b)) shows the x-axis in terms of area expansion with respect to tensionless state. The rupture expansion $(a_{f,\text{pore}} - a_{f,0})/a_{f,0}$ is higher for longer L_t. For $L_t = 4$, it is 10% , for $L_t = 5$, it is 18% and for $L_t = 7$, it is 21%. The increasing rupture expansion strength with increasing L_t have been observed in experiments [76]. The divergence of tension from linear behaviour at $a_f \gg a_{f,0}$ and close to $a_{f,\text{pore}}$ has

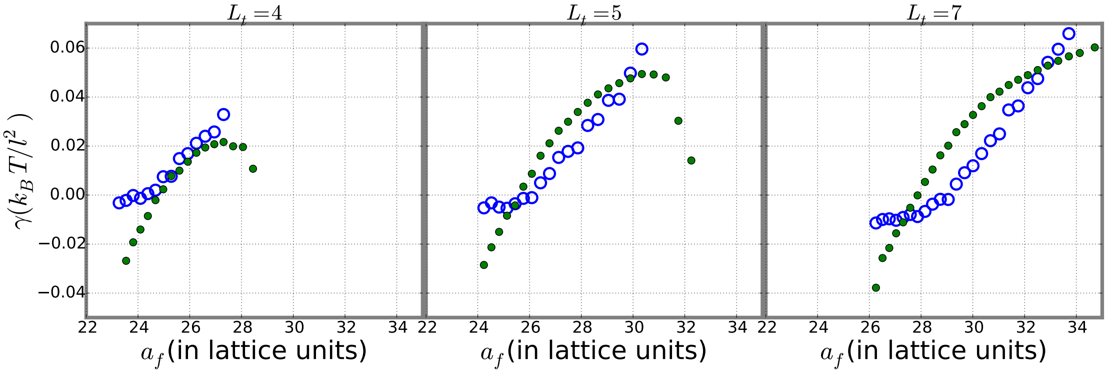

FIGURE 3.9 The plots showing the comparison between γ_{fluc} and γ_{mech} for different L_t. The open blue circles represent γ_{fluc} and closed green represent the γ_{mech}.

also been observed in experiments [82].

3.4 Comparison between the two tensions

The difference between γ_{fluc} and γ_{mech}, especially at the magnitudes of tension close to the tensionless state, has been a long ongoing debate. There has been studies which conclude that these two tensions are different [92, 93, 104, 105] and while other studies suggest that they are equivalent [94, 106]. To summarise section 3.2, the fluctuation tension is the measure of changes in free energy with respect to the changes in area due to shape fluctuations in the membrane. From section 3.3, the mechanical tension is the magnitude of the restoring force per unit length acting in the plane of the frame, which acts when the area of frame is perturbed from tensionless state [93]. At the value of a_f where mechanical tension vanishes, membrane has a zero restoring force as the frame area is changed. However, the shape fluctuations in the membrane are still possible with having a zero restoring force on the average. The difference between the tensions depend on the number of degree of freedom available for shape fluctuations, M_{free}. The value of M_{free} can be realised by observing the summation in Eq.(3.12),

$$M_{free} = \sum_q \tag{3.24}$$

In Schmid 2011 [106], this difference has been addressed. The author, using simulation of one dimensional membrane in two dimensional space, found that the difference, $\gamma_{mech} - \gamma_{fluc}$, at low tensions is directly proportional to M_{free}.

Fig.(3.9) shows the two tensions plotted together for different values of L_t. At the moderate positive tensions compared to the tensionless state, for $L_t = 4$, the results are equivalent to the results by Imparto 2006 [93]. The author showed that mechanical

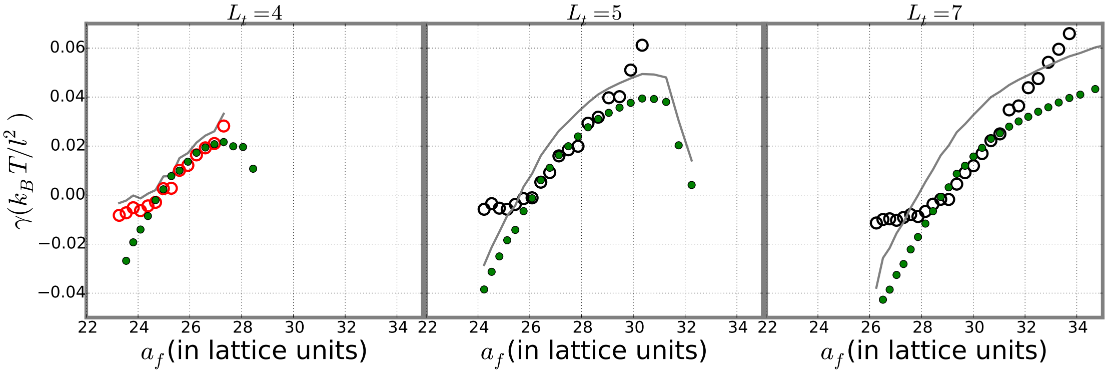

FIGURE 3.10 The plots show the collapse of data via the transformations of the form $\gamma_{mech} = C_1\gamma_{fluc} + C_2$ (see text) for different L_t. The grey lines show the old positions of tension as can be observed in Fig.(3.9). For $L_t = 4$, the transformation has been done from old γ_{fluc} (grey line) to the $C_1\gamma_{fluc} + C_2$ (open red circles). In this case $C_1 = \langle A\rangle / A_f$ chosen from Eq.(3.25) and $C_2 = -0.005 k_B T/l^2$. A similar value of C_1 has been chosen for $L_t = 5$ and $L_t = 7$, open black circles represent $C_1\gamma_{fluc}$ for these L_t. The old values of γ_{mech} is for $L_t = 5$ and $L_t = 7$ are shown by the grey lines. The transformation $\gamma_{mech} - C_2$ is shown by closed green dots for $L_t = 5$ and $L_t = 7$. The value of $C_2 = 0.01 k_B T/l^2$ for $L_t = 5$; and $C_2 = 0.017 k_B T/l^2$ for $L_t = 7$.

tension can be expressed in the terms of fluctuation tension as

$$\gamma_{mech} = \frac{\langle A\rangle}{A_f}\gamma_{fluc} - \frac{k_B T M_{free}}{2A_f} \tag{3.25}$$

where, $\langle A\rangle$ is the average real area. In Eq.(3.25), $\langle A\rangle$ can be found out by using

$$A = \int_{A_f} dxdy\sqrt{1 + (\nabla Z)^2} \tag{3.26}$$

where Z is same quantity on the left hand side in Eq.(3.6). In Eq.(3.25), it can be seen that assuming $\gamma_{mech} = 0$ implies $\gamma_{fluc} \propto M_{free}$. This corroborates to the above discussion, that γ_{fluc} (shape fluctuations) can exist even if γ_{mech} (restoring force) is zero. Furthermore, the shape fluctuations depend upon the number of degree of freedom to available to them.

The comparison between γ_{fluc} and γ_{mech} for $L_t = 5$ and $L_t = 7$ is opposite to the result for $L_t = 4$. The relation $\gamma_{fluc} < \gamma_{mech}$ is followed for the range of moderate tension. Neder et. al. 2010 [107] also observed similar behavior at extremely high tensions. However, there has not been any rigorous theory to account for these results. In our simulations, a parameter clearly contributing to such behaviour is the increase in the membrane thickness with longer L_t (section 3.6). In most of the previous analytical and simulations studies, the membrane is considered to be a thin two dimensional surface. The effect of membrane thickness has not been considered. In our simulations, the condition $A_f \gg w^2$ is still followed, however, some unexplained effects arise as w increases above a certain value within this limit. These effects might be considered in a future work.

Nonetheless, Eq.(3.25) predicts the functional form $\gamma_{mech} = C_1\gamma_{fluc} + C_2$, where C_1 varies with a_f and C_2 is a constant. If $C_1 = \langle A\rangle / A_f$ is kept the same as in Eq.(3.25) and C_2 is allowed to be a positive constant, a similar collapse of data for γ_{fluc} and γ_{mech} at the moderate tensions is found. The results are summarised in the Fig.(3.10).

On a side note, the relation $\gamma_{fluc} > \gamma_{mech}$ is followed at high tensions which was also shown by the analytical solution of Schmidt 2011. Similarly, at the negative tensions, a slower decrease of γ_{fluc} was also noted by Avital et. al. 2015 [94]. The reproduction of behaviours at the both extremes suggests the validity of results at the moderate tensions.

3.5 Polymer brush model (PBM)

In this section, we model lipid membranes by considering lipid tails as the freely jointed polymer chains. The elasticity of the membrane can be explained by a combination of the effect of the confinement of polymer chain entropy and the hydrophobic repulsion between tails and solvent at the interface of the membrane [82, 116, 117]. The probability distribution of the end to end distance, R_e, of a freely jointed chain can be approximated by a Gaussian function.

$$P(R_e) = \left(\frac{3}{2\pi N_m b^2}\right)^{3/2} \exp\left(-\frac{3N_m}{2}\left(\frac{R_e}{R_{max}}\right)^2\right) \tag{3.27}$$

Here, N_m is number of monomers in the chain, b is the effective statistical segment, also called *Kuhn* segment. If R_{max} is the maximum end to end distance that a polymer with N_m monomers achieves, then,

$$R_{max} = N_m b \tag{3.28}$$

The assumption made in the derivation of Eq.(3.27) is $R_e \ll R_{max}$. The free energy based on the Gaussian approximation is

$$F = \frac{3k_BTR_e^2}{2N_m b^2} + F_{R_e=0} \tag{3.29}$$

where $F_{R_e=0}$ is the free energy at $R_e = 0$. The free energy in Eq.(3.29) constitutes only the entropic contributions, since the interaction energy is not considered in the ideal chain [118]. However, this approximation fails for $R_e \simeq R_{max}$, as the Eq.(3.29) predicts finite probability even when $R_e > R_{max}$, which is non-physical. In the special case, if the chains are forced to stay elongated by constraints like in a polymer brush or a bilayer, then, free energy is calculated in a constant force ensemble. In this ensemble, the free

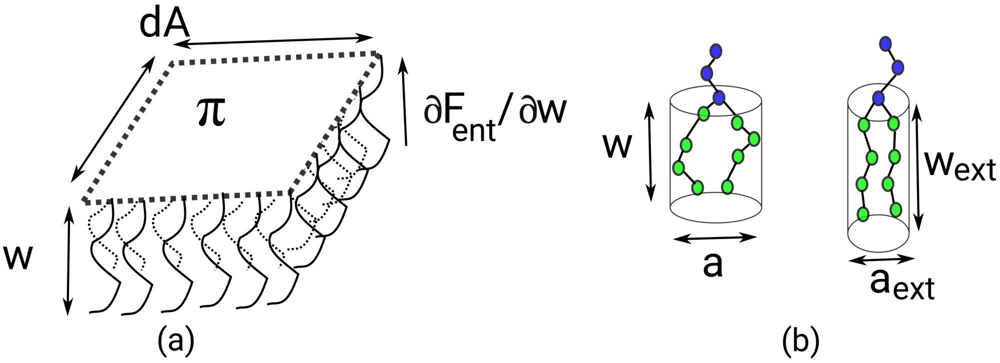

FIGURE 3.11 (a) The schematic diagram showing the force balance required at a small area element, dA. (b) The representation shows the difference in the confinement of tails in a general situation with area a, and in the reference state in which tail chains are maximally extended with area a_{ext}.

energy has a function [118].

$$G_{chain}(f) = -k_BTN_m\left[\ln\left(4\pi\sinh\left(\frac{fb}{k_BT}\right)\right) - \ln\left(\frac{fb}{k_BT}\right)\right] \tag{3.30}$$

where f is the constant force acting on the ideal chain. This is the exact form of the free energy of the ideal chain. The conjugate variable of f is the end to end distance, R_e.

$$R_e = bN_m\left[\coth\left(\frac{fb}{k_BT}\right) - \frac{1}{(fb/k_BT)}\right] \tag{3.31}$$

The function inside the large brackets is the Langevin function, $\mathcal{L}(\beta) = \coth(\beta) - \beta^{-1}$. The Langevin function predicts a saturation of R_e to R_{max} at large f. In contrast, Eq.(3.29) predicts linear change of R_e at all the magnitudes of the force. In the commonly studied systems, R_e is more readily measurable compared to f. Thus, the Legendre transform of $G(f)$ gives

$$F_{chain}(R_e) = -k_BTN_m\left[\ln\left(\frac{4\pi\sinh\left(\mathcal{L}^{-1}\left(R_e/R_{max}\right)\right)}{\mathcal{L}^{-1}\left(R_e/R_{max}\right)}\right) - \mathcal{L}^{-1}\left(\frac{R_e}{R_{max}}\right)\frac{R_e}{R_{max}}\right] \tag{3.32}$$

where $\mathcal{L}^{-1}$ is inverse of the Langevin function. Thus, $\mathcal{L}^{-1}(\mathcal{L}(\beta)) = \beta$. In this case, the free energy diverges at $R = R_{max}$.

For the polymer brush model, force generated by the surface pressure at an area element on the interface, $\Pi \cdot dA$, should balance the entropic force generated by the chains towards direction perpendicular to interface, z [82].

$$\Pi \cdot dA + \partial F_{ent}/\partial w \cdot dw = 0 \tag{3.33}$$

where dA is the microscopic area element on the interface, and dw is the length element in z direction, see Fig. 3.11(a). Note here, Π has units of k_BTl^{-2} instead of commonly known units of k_BTl^{-3}. Here, we follow the nomenclature from Rawicz et. al. 2000 [82]. The entropic free energy, F_{ent}, is directly proportional to chain free energy, F_{chain}. Thus, $F_{ent} = 2KF_{chain}$, where K is the constant of proportionality and factor of 2 arises due to two tails in a lipid molecule. The value of $\partial F_{ent}/\partial w$ represents the change in the free energy of lipid tails with respect to the change in end to end distance of tails in z direction, w. This quantity is proportional to the entropic force, f, in Eq.(3.31). For simplicity, we can assume $dA = a_l$. The membrane is assumed to be a $2D$ fluid which holds the incompressibility condition, implying $w \cdot a_l = constant$. Hence, if the area per lipid at the maximum extended state of tails, a_{ext}, is known, then, any arbitrary w and a_l will follow

$$w \cdot a_l = w_{ext} \cdot a_{ext} \tag{3.34}$$

where $w_{ext} = R_{max}$, Eq.(3.28), for the tails chains. In Rawicz et. al. 2000 [82], w_{ext} was chosen to be the condition in which both the tails of lipid have an all-*trans* state. The bond length in BFM is known to be $2.7l$ implying, $w_{ext} = 2.7L_tl$, see Fig. 3.11(b). As an example, we can find out a_{ext} for a system of BFM membranes with $L_t = 5$. For our simulation setup, at the tensionless state, $a_{f,0}$, thickness of a monolayer is $\simeq 5.39l$, for $L_t = 5$, Fig.(3.17). Therefore, for $L_t = 5$, using Eq.(3.34).

$$a_{ext}|_{L_t=5} = \frac{1}{w_{ext}} \times aw|_{a_{f,0}} = 10.30l^2 \tag{3.35}$$

A similar procedure finds $a_{ext} = 10.82l^2$ for $L_t = 4$ and $a_{ext} = 10.08l^2$ for $L_t = 7$. The pressure from Eq.(3.33) can be expressed as

$$\Pi = -\frac{2K\partial F_{chain}}{\partial w} \times \frac{\partial w}{\partial a_l} \tag{3.36}$$

Using Eq.(3.34), we obtain $\partial w/\partial a_l = -w_{ext}/(a_l^2 a_{ext})$. The chain extension ratio, x, is defined as $x = w/w_{ext} = a_{ext}/a_l$. In terms of x, for example, $\partial w/\partial a_l = -x^2 w_{ext}/a_{ext}$. The pressure in x using Eq.(3.32) can be written as

$$\Pi = \frac{2Kx^2L_t}{a_{ext}}\frac{\partial F_{chain}}{\partial w} = \frac{2k_BTKL_tx^2}{a_{ext}}\mathcal{L}^{-1}(x) \tag{3.37}$$

Finally, the interaction energy arising of the repulsion between solvent and tail monomers at the interface must be considered and total free energy of the membrane can be written,

$$F = \gamma_{surf}a_l + 2KF_{chain} \tag{3.38}$$

Note that, here γ_{surf} is not equal to either γ_{fluc} or γ_{mech}. Since, we do not consider any contribution from the shape fluctuations, a partial derivative of Eq.(3.38) with respect to a_l gives γ_{mech}.

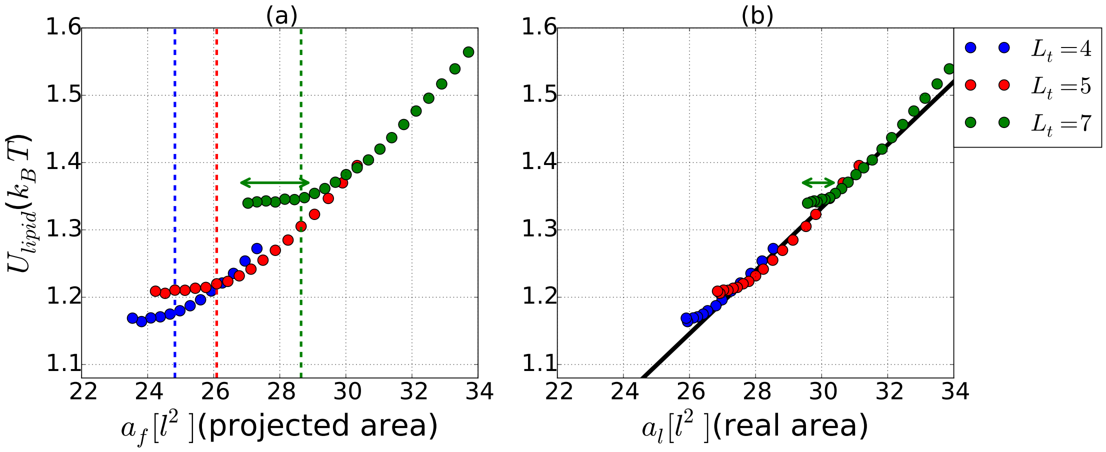

FIGURE 3.12 (a) Internal energy per lipid, U_{lipid}, considering only the tail and solvent contacts, as a function of a_f for different L_t. The vertical dashed lines represent the tensionless state, $a_{f,0}$. (b) U_{lipid} as a function of real area per lipid, a_l.

Discussion

Fig.(3.12(a)) shows the change of internal energy per lipid, U_{lipid}, with respect to a_f. It is calculated by averaging the nearest neighbour contact energy generated by the tail and solvent monomers. This is similar to the results of Werner et. al. 2012 [54]. However, in their work, authors also included the interactions between head and tail monomers. The first term on the right hand side of Eq.(3.38) is U_{lipid}, thus,

$$U_{lipid} = \gamma_{surf} a_l \tag{3.39}$$

In Fig.(3.12(a)), U_{lipid} is plotted versus the frame area per lipid, which is the projected area set by the simulation box. The value of U_{lipid} is almost constant for $a_f < a_{f,0}$. The reason for this behaviour can be understood by observing Fig.(3.3). At values $a_f < a_{f,0}$, the amplitude of low q modes is high, which is related to the shape fluctuations in the membrane. In this regime ($a_f < a_{f,0}$), any increase in a_f (via decrease in N_{lipids}) contributes to the suppression of these modes. To correct for underestimation of the surface area we display in Fig.(3.12(b)) the value of U_{lipid} with respect to area per lipid, a_l, calculated by using the real area, Eq.(3.26). One can observe that a_l changes negligibly in this regime. This is indicated by the shrinkage of double headed green arrow for $L_t = 7$ in Fig.(3.12(b)) in comparison with Fig.(3.12(a)). Thus, the negligible change in U_{lipid} is explained by a negligible change in a_l.

The increase of U_{lipid} with a_l in region with $a_f > a_{f,0}$, has also been observed in experiments, and increased contacts between solvent and hydrophobic tails at the interface at high a_f is considered to be a major reason for the increase in tension [117]. This increase of energy density at the interface explains the transition of bilayer into pore state. The increase in first term in Eq.(3.38) can be counteracted by the introduction of a pore. In a

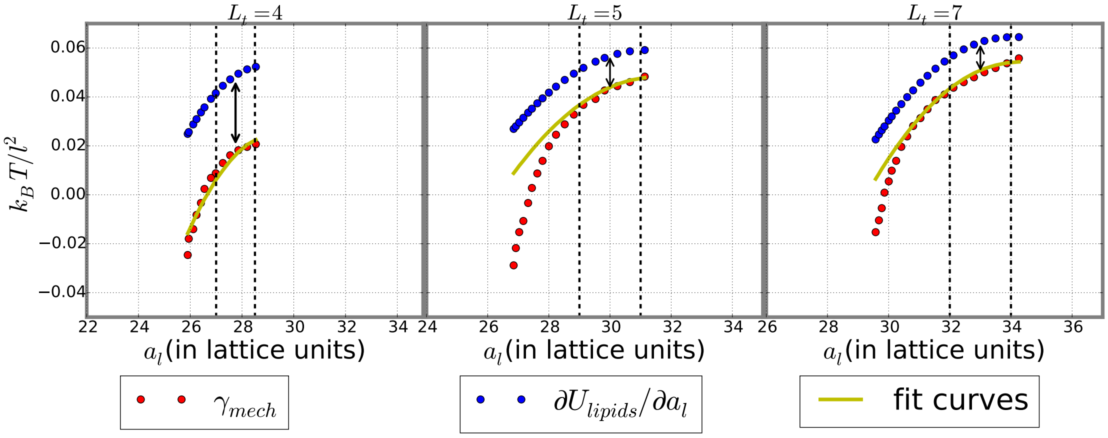

FIGURE 3.13 The blue dots represent the $\partial U_{lipid}/\partial a_l$ and red dots represent the γ_{mech} (see Eq.(3.42)) for different L_t. The value of $\partial U_{lipid}/\partial a_l$ is calculated by finding the slope of curves in Fig.(3.12(b)). The yellow fit curves corresponds to the finding best fits of K in Eq.(3.42). The value of K obtained for the fits for $L_t = 4$ is 0.24, $L_t = 5$ is 0.1 and $L_t = 7$ is 0.094.

membrane attached to a frame, the first term reduces to $\gamma_{surf} a_l \rightarrow \gamma_{surf}(a_f - A_p/N_{lipids})$, where A_p is the area of the pore. A detailed analysis of free energy of pore formation based on the polymer brush model (PBM) is discussed in the next chapter.

In Fig.(3.12(b)), one can observe that the data points of U_{lipid} (in the region where it is linear with respect to a_l) for all L_t lie almost along the same linear curve (black line). This implies that on average, the magnitude of γ_{surf}, Eq.(3.39), is almost equal for all L_t.

The value of U_{lipid} at $a_{f,0}$ is higher for longer L_t, see the intersection of vertical lines with the U_{lipid} in Fig.(3.12(a)). This could be potentially explained by differentiating Eq.(3.38) with respect to a_l

$$\gamma_{mech} = \gamma_{surf} + a_l \frac{\partial \gamma_{surf}}{\partial a_l} - \Pi \tag{3.40}$$

Π in the above expression can be explained by noticing that the second term of left hand side in Eq.(3.38) is $2KF_{chain}$. Thus, by Eq.(3.36), $\Pi = -\partial(2KF_{chain})/\partial a_l$. At the tensionless state, $\Pi = \gamma_{surf} + a_l \partial\gamma_{surf}/\partial a_l$. As discussed already, γ_{surf} behaves similarly for all L_t, therefore, $\Pi \sim k_B T a_l/l^4$. Here, $k_B T/l^4$ are the dimensions of $\partial\gamma_{surf}/\partial a_l$. Thus, at the tensionless state, using Eq.(3.37),

$$\frac{k_B T a_{f,0}}{l^4} \sim \frac{k_B T L_t a_{ext}}{a_{f,0}^2} \implies a_{f,0}^3 \sim L_t a_{ext} l^4 \tag{3.41}$$

where large extension limit, $w \sim w_{ext}$, has been used to expand $\mathcal{L}^{-1}(x) \simeq (1-x)^{-1}$. The term $L_t a_{ext}^2$ increases with L_t, using a_{ext} from Eq.(3.35) and the discussion below. This explains the larger value of $U_{lipids}(a_{f,0})$, and $a_{f,0}$ for longer tails.

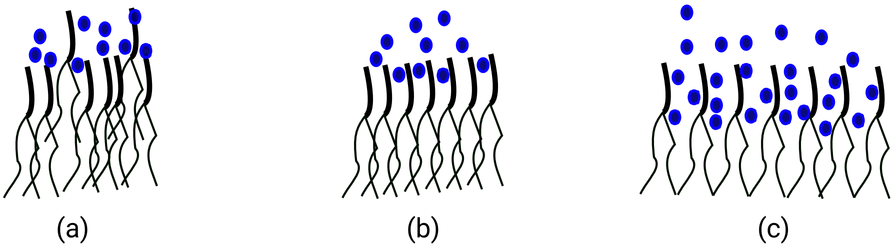

FIGURE 3.14 The schematic diagram showing the contribution of interaction and entropic part to the free energy of lipids tail in the membrane in the case of (a) $a_f < a_{f,0}$; entropic free energy is larger than interaction free energy (b) $a_f \simeq a_{f,0}$; entropic free energy almost balances the interaction free energy (c) $a_f > a_{f,0}$; interaction free energy is larger than entropic free energy.

The mechanical tension in PBM: It was found that for the discussion in this section, simulation results are better explained in the terms of a_l instead of a_f. Thus, we switch to area per lipid, a_l, for the rest of this section. Eq.(3.40) can be rewritten as

$$\gamma_{mech} = \frac{\partial U_{lipid}}{\partial a_l} - \frac{2k_B T K x^2 L_t \mathcal{L}^{-1}(x)}{a_{ext}} \tag{3.42}$$

Note that, in Fig.(3.12(a)), U_{lipid} appears to be linear in the region $a_f > a_{f,0}$, also in the corresponding curves with respect to a_l, Fig.(3.12(b)). However, if one notices the y axis in Fig.(3.12), the graphs are plotted in the order of magnitude of $10^{-1}k_BT$. The value of $\partial U_{lipid}/\partial a_l$ with respect to a_l is not constant at magnitudes comparable to $10^{-2}k_BT/l^2$. This can be seen in the Fig.(3.13). The data points for $\partial U_{lipid}/\partial a_l$ have been generated from Fig.(3.12(b)) using the *smoothing spline method*. The method is only implemented on the points where $\partial U_{lipid}/\partial a_l \neq 0$ and then extrapolated to the points with $\partial U_{lipid}/\partial a_l = 0$.

In fitting Eq.(3.42) with γ_{mech} from simulation data, the only unknown fitting parameter is K. It is mentioned in the caption of Fig.(3.13) for different L_t. The fittings are good in the region where the magnitudes of tension are larger than the tensionless state. In the regions with $a_f \lesssim a_{f,0}$, the tails are strongly stretched. In the region, $\gamma_{mech} < 0$, Eq.(3.42), the entropic pressure is higher than $\partial U_{lipid}/\partial a_l$, thus, the lipids spontaneously distort their collective planar geometry to relieve the entropic free energy, Fig.(3.14). These effects are not appropriately captured in the PBM. Therefore, the PBM does not fit well in this region. The contribution of total entropic force to the γ_{mech} decreases with L_t. This can be observed as the reduction of the difference (double headed arrows) between $\partial U_{lipid}/\partial a_l$ (blue dots) and the γ_{mech} (red dots) with L_t, Fig.(3.13). This can be qualitatively explained by the surface pressure related to an ideal chain.

$$\Pi_{chain} = \frac{k_B T x^2 L_t \mathcal{L}^{-1}(x)}{a_{ext}} \simeq \frac{k_B T a_{ext}^2 L_t}{a_l^3} \tag{3.43}$$

Here, we used small stretching approximation, $w \ll w_{ext}$, to expand $\mathcal{L}^{-1}(x) \simeq x$. The term $k_BTa^2_{ext}L_t/\bar{a}^3_l$ decreases with L_t. The value of $\bar{a}_l$ represents the average value of area per lipid in the small stretching limit shown by vertical lines in Fig.(3.13). The value of $\bar{a}_l$ increases with L_t (as $a_{f,0}$ increases with length of tails), which scales the Π_{chain} with the power of minus 3. Thus, Π_{chain} decreases with L_t. A simpler explanation, for this behavior of Π_{chain}, is evident from the extension ratio, $\bar{w}/w_{ext}$, which decreases with L_t. Here, the value of $\bar{w}$ represents the average of w in between the two dashed lines in Fig.(3.13).

This effect explains the increase in the surface tension with the length of lipids at $a_f \lesssim a_{f,\text{pore}}$, which implies membrane with longer lipids can resist larger stresses before transiting to a pore state.

3.6 Solvent permeability and the stress

The solvent translocation from one side of the membrane to other side (permeability) can be used to characterize various properties of the bilayers. Solvent permeability, P_s, is known to change with temperature, area per lipid, saturation of the tails and in the presence of antimicrobial peptides and cholesterols [108]. The dependence of P_s on the concentration of the antimicrobial peptides will be discussed in the next chapter. An example of the permeability change with temperature could be found in the study by Blicher et. al. 2009 [109], where the authors found that the solvent permeability maximizes at gel-liquid phase transition temperature. A more detailed review of the solvent permeability of the lipid bilayers under various conditions can be found in Shinoda 2016 [108]. In this section, the effect of tail chain length, L_t, and stress, a_l, (or a_f) on the P_s is discussed.

For the calculation of permeability in simulations, positions of solvent monomers are observed after every 100 MCS. If a solvent monomer follows a trajectory such that it starts at one side of the membrane midplane and finally ends at the other side, then it is considered as a single translocation event. The distances on the either side of the midplane from which the solvent monomers are observed depends upon the thickness of the membrane. The membrane thickness can be estimated using Gibbs dividing surface or the distance between two head density maxima along the normal direction of the bilayer, Fig.(1.8) [82]. Here, we use the standard deviation of lipid monomers along normal of the membrane to calculate the thickness, $SD_z = \sqrt{\langle z^2 \rangle - \langle z^2_{COM} \rangle}$. z_{COM} is calculated using Eq.(3.8). The membrane is divided into bins of area $8l \times 8l$. The midplane of all bins are found by using Eq.(3.7). $SD_z^{\{mem\}}$ is the average thickness of the membrane. $SD_z^{\{xy\}}$ is the thickness of membrane in a specific bin with coordinates

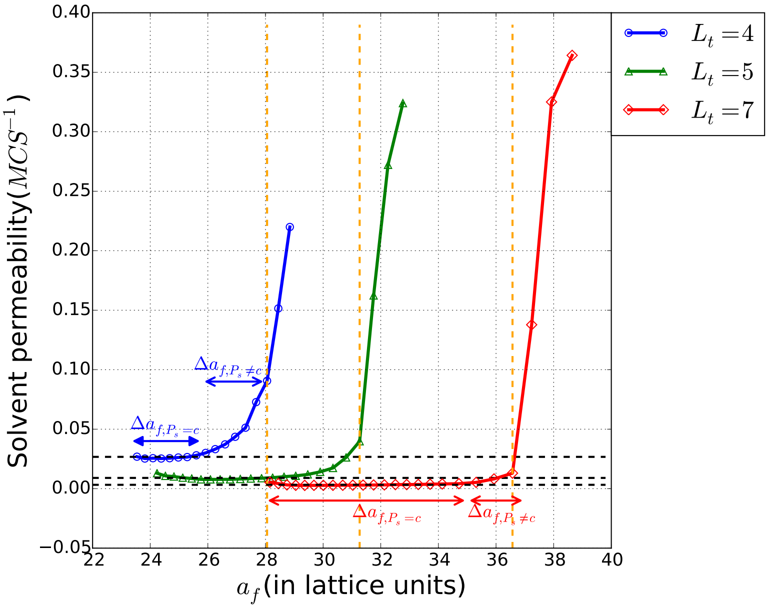

FIGURE 3.15 The solvent permeability as a function of the tail chain length L_t and a_f. The horizontal black dashed lines represent average of P_s for different L_t, where the P_s changes less than 10% of its value near the tensionless state. The range of a_f where P_s is constant with respect to a_f, $\Delta a_{f,P_s=c}$, is indicated by double headed arrows for $L_t = 4$ and $L_t = 7$. Similarly, the range of a_f where P_s changes non linearly with a_f, $\Delta a_{f,P_s\neq c}$, has been also indicated with double headed arrows for the same L_t. The vertical orange line represent the position of $a_{f,\text{pore}}$ for all the L_t.

(x, y). $SD_z^{\{mem\}}$ is calculated by averaging $SD_z^{\{xy\}}$ over all the bins. P_s is calculated by

$$P_s = N_{\text{solvent}}/\Delta t \tag{3.44}$$

where, N_{solvent} is the total number of solvent monomers passing through the distance of $z_{COM}^{\{xy\}} \pm SD_z^{\{mem\}}$ in time of Δt MCS. Note, there is a pore formation at large values of a_f (high stress). A bin is tagged as a pore bin if it has less than 30% of lipids compared to average lipids in other bins. The pore bin is then assigned the value of z_{COM}^{xy} of an adjacent bin if that bin is not a pore bin [57].

Fig.(3.15) summarises the results from the simulations. The abrupt change in P_s on the right side of the dashed vertical orange line indicates the pore formation. Close to the tensionless state the increase of a_f (or stress) has a negligible effect on P_s. This range of a_f where change in P_s is almost equal to zero; $\partial P_s/\partial a_f \simeq 0$, can be observed to be parallel to black dashed horizontal lines. The range of a_f, where this holds true is defined as $\Delta a_{f,P_s=c}$ (P_s = constant). This range increases with L_t. This can be observed in Fig.(3.15) by comparing $\Delta a_{f,P_s=c}$ for $L_t = 4$ and $L_t = 7$. The ratio, $\Delta a_{f,P_s=c}/a_{f,0}$, which is the area expansion compared to the tensionless area per frame is 0.06, 0.12, and 0.19 for $L_t = 4$, $L_t = 5$ and $L_t = 7$, respectively. In the experimental studies of Vitkova et. al. 2004 [110], the authors found a negligible change in the solvent permeability as

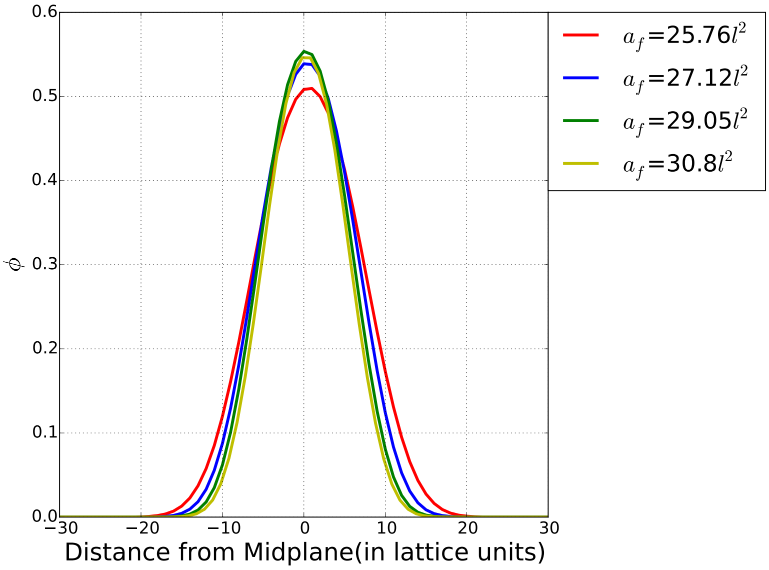

FIGURE 3.16 The fraction of lattice sites occupied by lipid monomers (heads + tails) in the plane of membrane (xy plane) as a function of distance from the midplane of the membrane (z direction). The presented graphs are for the membranes at different stresses (i) $a_f = 25.76l^2$ (red curve) is close to the tensionless state (ii) $a_f = 27.12l^2$ (blue curve) and $a_f = 29.05l^2$ (green curve) have increasing a_f (stress), but they are in the region $\Delta a_{f,P_s=c}$ (iii) $a_f = 30.8l^2$ (yellow curve) has the highest stress but is in region $\Delta a_{f,P_s\neq c}$ (see text). The value of L_t is chosen to be 5.

the area per lipid is increased near the tensionless state. This is similar to $\Delta a_{f,P_s=c}$ observed in our simulations.

Fig.(3.16) shows an increased density of lipids monomers near the midplane and a decrease in the thickness of the membrane as the value of a_f increases (*curves red* → *blue* → *green*). These two behaviour have an opposite effect on P_s. The increased midplane density reduces the solvent diffusion through the midplane. In contrast, the decreased membrane thickness enhances the solvent diffusion. The opposing effects on the solvent diffusion counteract each other which keeps the value of P_s almost constant. These effects were also noted by Gauthier et. al. 2007 [111] in their coarse grained model with more detailed lipids, and the atomistic simulations by Feller et. al. 1995 [112]. If the value of a_f is further increased above $\Delta a_{f,P_s=c}$, then the thickness decreases and but there is no increase in the density at the midplane, Fig.(3.16) (yellow curve). This leads to a non linear increase in the permeability which can be observed in the Fig.(3.15). This region is indicated by $\Delta a_{f,P_s\neq c}$,($P_s \neq$ constant) in Fig.(3.15). The area expansion $\Delta a_{f,P_s\neq c}/a_{f,0}$ is 0.06, 0.05 and 0.02 for $L_t = 4$, $L_t = 5$ and $L_t = 7$ respectively.

If the area expansion ranges $\Delta a_{f,P_s=c}/a_{f,0}$ and $\Delta a_{f,P_s\neq c}/a_{f,0}$ for different L_t are observed, one realises that the membranes with longer tails transit into the pore state (induced by stretching) more abruptly compared to shorter tail membranes. In Fig.(3.15), P_s for membranes with $L_t = 4$ is constant with respect to a_f for almost 50% of rupture

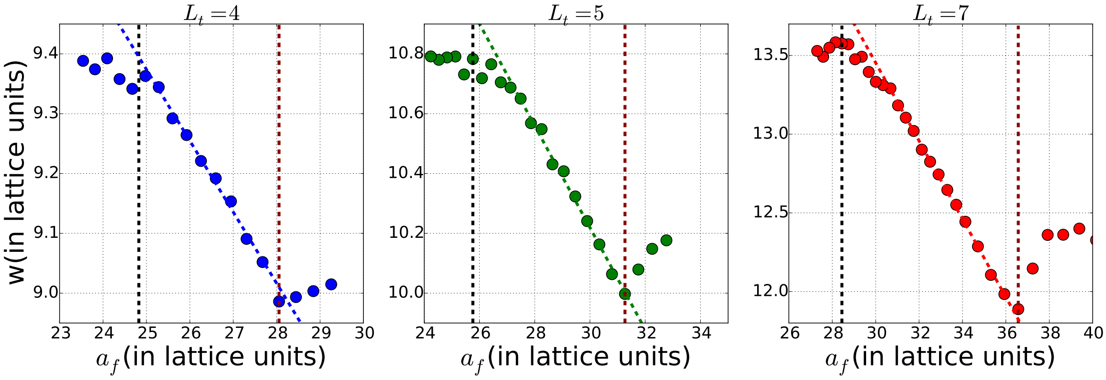

FIGURE 3.17 Membrane thickness as a function of the a_f and tail length. The black vertical dashed lines point to the tensionless state, $a_{f,0}$. The dark red dashed line shows the area of pore state stabilisation, $a_{f,\text{pore}}$.

area expansion $(a_{f,\text{pore}} - a_{f,0})/a_{f,0}$. In contrast, the membranes with $L_t = 7$, P_s stays constant for almost 91% of rupture area expansion.

Membrane thickness

To calculate membrane thickness, w, the average position of the h_2 head monomer, see Fig.(2.3), in the direction normal to membrane (z axis). To assign a particular leaflet to a lipid, the orientation vector is considered, Fig.(2.7). If z component of the orientation vector follows $\vec{o}_i \cdot \vec{z} < 0$, then, the lipid belongs to the upper leaflet and vice versa. The difference in the average position of the h_2 in between two leaflets determines the thickness of membrane.

The relation of thickness with respect to a_f can seen to be different in three section divided by the vertical lines in Fig.(3.17). In the region, where $a_f < a_{f,0}$, the thickness is almost constant with respect to the change in a_f. The strength of shape fluctuations can potentially explain the reason for the average width to stay constant in this region, Fig(3.3).

For $a_f > a_{f,0}$ and $a_f < a_{f,\text{pore}}$, a linear decrease with respect to a_f. The linear decrease corresponds to the incompressible fluid condition of the membrane, Eq.(3.34). As the area per lipid increases, the membrane thickness decreases in order to keep the volume per lipid constant.

The increase in the thickness for $a_f > a_{f,\text{pore}}$, with the increase in a_f, is the result of finite area provided to the membrane by the periodic box. At $a_f > a_{f,\text{pore}}$, the area of the pore is occupied by the solvent, the increase in the lateral stress by the solvent which results in the increased membrane thickness, see Fig.(3.18). The magnitude of $w(a_f)$ increases monotonically with L_t, which is a general observation in literature [111–115].

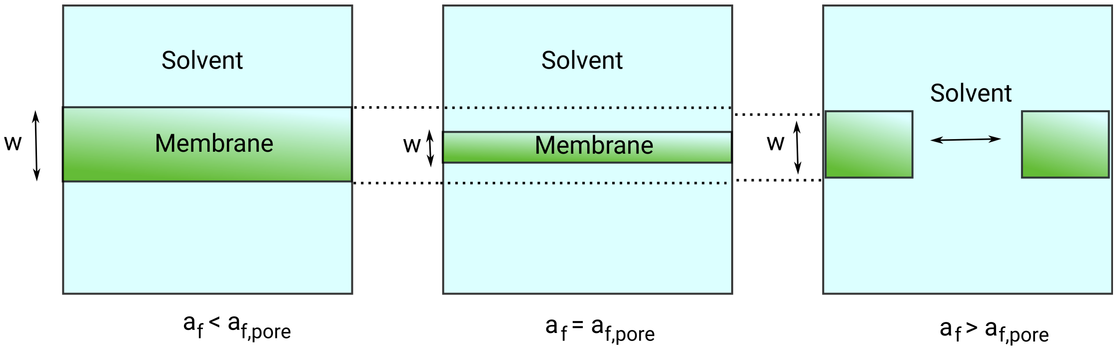

FIGURE 3.18 The schematic diagram showing membrane at different a_f with respect to $a_{f,\text{pore}}$. The membrane thickness decreases from $a_f > a_{f,\text{pore}}$ to $a_f = a_{f,\text{pore}}$. The pore stabilizes at $a_f > a_{f,\text{pore}}$, thus, the solvent is filled in the pore. This increases the membrane thickness.

3.7 Conclusion

In this chapter, we have considered the stress acting on the simulated model membranes. In the simulations, we fixed the total (frame) area while the number of lipids and the tail lengths was varied.

By changing the number of lipids, N_{lipids}, and consequently area per lipid enforced by frame, a_f, three states of the membrane can be observed. These are membranes with pore state, tensionless state, and buckled state. The fluctuation tension, γ_{fluc}, can characterize the tensionless state ($\gamma_{fluc} = 0$) and buckled state ($\gamma_{fluc} < 0$). The procedure used to calculate γ_{fluc} is not valid for membranes in a pore state. The value of a_f at which tensionless state is observed, $a_{f,0}$, increases as the length of tails, L_t, of the lipids in the membranes is increased. Using the slopes of γ_{fluc} versus area expansion, $(a_f - a_{f,0})/a_{f,0}$, area compressibility, K_A, is found. The expression for the fluctuation spectrum obtained from Helfrich model also finds the bending rigidity, κ. The elastic constants, K_A and κ for the membranes simulated here, are on the lower end of the spectrum of observed experimental values. However, their relation with L_t and stress (a_f) reproduces the observed experimental behaviors reasonably well [82].

For identifying a pore state, the mechanical tension, γ_{mech}, can be calculated. The value of γ_{mech} is calculated by integrating stress anisotropy along the normal direction to the membrane. The stress anisotropy profiles reveal the behavior of contracting stress (due to the hydrophobic interactions) and repulsive stress (due to the entropy of tails, in section 3.5) along the normal. These profiles are analysed near the tensionless state and pore state of the membrane. The pore state is characterized by a sudden decrease in γ_{mech} with an increase of a_f. The boundary value of a_f at which pore state is stabilized, $a_{f,\text{pore}}$, is characterized by the presence of both the pores and the intact state. An intact state is the opposite of pore state, characterized by the absence of a pore in the membrane. A slight increase in a_f in comparison with $a_{f,\text{pore}}$ leads to the stable pores in membranes and a slight decrease makes the intact membrane state stable. The value of γ_{mech}, at which pore state is stabilized, increases as the length of lipids, L_t, in the membranes is increased. Similarly, $a_{f,\text{pore}}$ also increases with L_t. This is in accordance with the behaviors observed in experiments and simulations found in literature, which points towards reliability of our highly accelerated and coarse-grained simulation results [76, 82].

At the moderate values of tensions, a relation $\gamma_{mech} = C_1\gamma_{fluc} + C_2$ is found, where C_1 is function of a_f and C_2 is a constant. This relation has been suggested by some of the previous analytical and simulation studies [93, 106]. However, in these studies, a membrane is considered to be a two dimensional surface and the effect of the thickness might change the final expression relating the both tensions. In our simulations, if C_2 is set to be positive, then, a collapse in the simulation data for thicker membranes ($L_t = 5$ and $L_t = 7$) could be observed. In the previous studies, C_2 was understood to be negative. The understanding of this unexpected behavior is an interesting problem for a future work.

The transition of the membrane into a stable pore state from an intact membrane state (with increasing a_f) can be explained by the polymer brush model (PBM). The PBM considers two contributions to the free energy of a flat membrane: (i) entropic energy of tails acting as free jointed polymers and (ii) hydrophobic interactions between tail and solvent monomers at the interface. The increased contacts at the interface with increasing a_f make the membrane shift to a pore state. The surface area decreases as the pore appears in the membrane, which relieves the energy generated by the hydrophobic contacts at the interface. The PBM suggests that the mechanical tension can be expressed in the terms of slope of internal energy per lipid and a_l curve, $\partial U_{lipid}/\partial a_l$, and the entropic force. The simulation data fits the analytical expression of mechanical tension driven from PBM at the magnitudes of tension where shape fluctuations are negligible. The contribution of total entropic force decreases with the increase in length of tails. The tails are more relaxed in the membranes with longer tails at positive values of stresses. The entropic force per lipid is found by assuming that it is proportional to the force generated by a ideal polymer chain. The entropic force generated by the polymer chain is the inverse Langevian function of its end to end distance, $\mathcal{L}^{-1}(R_e)$.

The solvent permeability, P_s, at a_f near $a_{f,0}$, is negligibly affected by the increase in a_f. The presence of pores leads to changes in the solvent permeability, P_s, and membrane thickness, w. As the pore state stabilizes, a further increase in the a_f leads to an abrupt increase in the P_s. The membrane acts as incompressible liquid, in the range $a_f > a_{f,0}$ and $a_f < a_{f,\text{pore}}$, the increase in value of a_f decreases the value of w. At $a_f > a_{f,\text{pore}}$, increase in a_f increases the w. The increase in lateral pressure in this range of a_f increases the membrane thickness in a constant area ensemble.

Chapter 4

Interaction of lipid Bilayer Membranes with Amphiphilic Copolymers

In this chapter, section 4.1 gives a general introduction and literature review of the problem of antimicrobial resistance. This section further describes the role of the antimicrobial peptides and the synthetic polymers in solving it. The section 4.2 introduces two systems which have been set up to analyze the interaction of amphiphilic copolymers with membranes. The section 4.3 describes the reasons for the choice of the specific type of copolymers used in the present work. All the results of the simulations and their interpretations are described in the section 4.5 and summarised in the section 4.6.

4.1 Introduction

The use of the modern antimicrobial materials has saved millions of lives since the last century. The advent of the modern antibiotics started with the discovery of *penicillin* by Alexander Fleming in 1928. However, as soon as 1950s, some species of bacteria resistant to penicillin were already found [119]. Since then, one by one micro-organisms like viruses, bacteria, fungi etc. have evolved to make many of the newly found antibiotics ineffective. The small life cycle of the micro-organisms makes their evolution faster than the current rate of the development of the new materials to fight against them. Micro-organisms use gene altering processes like horizontal gene transfer, mutation etc. to evolve into the species which have no effect from the drug. The practices like over prescribing of antibiotics by healthcare officials further promote such evolution of micro-organisms. The centre for disease control (CDC) of the USA, has announced in a report in 2013, that the "human race is in a post-antibiotic era" [120]. Furthermore, in the private sector, investment towards the invention of new antimicrobial materials is not incentivized as the effectiveness of any such materials is only short lived.

Therefore, there is a dire need to develop novel materials which can act as antimicrobial agents and also deal with the antimicrobial resistance. One of the commonly known agents against microbes are antimicrobial peptides (AMP) [121]. AMPs, also called the host defense peptides, are a part of the immune system of most organisms. With not much success in the clinical studies yet, AMPs have been extensively studied in the fundamental experimental studies. They are one of the most anticipated substances in the antibiotic research. In contrast to most of the presently used antibiotics, they enhance the immune response.

In Dubos 1939 [122], first reported AMP can be found. The *gramicidin* was extracted from a bacterium called *soil bacillus*. The author found that the extracted material can protect mice from infections caused by other bacteria. The *gramicidin* was also later used in the treatment of ulcers and wounds. In 1950s many animal-based AMPs like from rabbit leukocytes, cow milk etc. were found [123]. Since then, many more AMPs have been identified. The LAMP is a database linking all the AMPs. It has been created to increase the efficiency of collaborations between scientific groups for designing the novel antimicrobial materials [124]. It has collected more than 5000 identified AMPs till date and out of which about 1000 have been artificially synthesized.

Not long after discovering the first AMP, numerous studies in 1950-60s were finding the presence of AMPs in the human immune system. At the moment, 103 human AMPs are known, 90 of which are specialized against bacteria, 58 against fungi and 16 against viruses [125]. Along with the protection against microbes, they also play a role in the movement of the cells along the concentration gradient, programmed cell death and healing of wounds. Nowadays, it has been established that in human and in other animals, the skin cells use AMPs as the first line of defense against the microbes. In the general case, the skin cells, for example, always produce AMPs for their protection. However, there are also special scenarios by which cells can enhance the production of AMPs when environmental conditions (like a increase in microbes population) are changed [125].

AMPs are generally short sequences ($5 - 100$) of amino acids. They are known to exist in many different kinds of secondary structures. The two most abundant forms are the α helix and β sheet structures. However, both the simulation and experimental studies have been more focused on the helical structures. The helical structures have their hydrophobic and hydrophilic amino acid units distributed at different parts of a helix. In the coarse-grained simulations, helical structures are generally modeled by assuming a cylindrical surface and having different parts of this surface at different hydrophobicities [126], Fig.(4.1). Examples of some AMPs like *penetratin*, amyloid proteins, *indolicidin* etc. are also found in nature which have random coil structure in a solution, but change into active (α or β) structure upon the contact with the cell membrane of the target microbes [127]. The *penetratin* changes its structure first from globular to α on interacting with the membrane. It can then turn into β sheets if the cationic charge on lipids membrane is increased. The structural change also depends on the degree of unsaturation of lipids in the membranes [127].

Interaction of AMPs with membranes

The mechanism with which AMPs attack the micro-organisms involves a destruction of their cell membranes or a disruption of protein or DNA and RNA synthesis [121]. In the case of non-membrane active peptides, they still have to interact with the membrane in order to taken in by the cell. For the scope of this thesis, we are only interested in their interaction with the membranes. Interaction of the AMPs with the cell membranes is an extensively studied phenomenon in both simulations and experiments [128, 129]. Depending upon the structure and hydrophobicity distribution along the surface, different type of mechanisms have been suggested, Fig.(4.1):

- *Barrel stave model*: In Ehrenstein et. al. 1977 [130], many peptides in the form of α helix were identified to follow this model. Here it is assumed that the peptides align their hydrophobic parts with the membrane core and hydrophilic part towards the solvent medium of the pore. Other examples of peptides used in Ehrenstein et. al. 1977 were *alamethicin*, *suzukacillin* and *monazomycin*.

- *Toroidal pores*: In this model, the peptides are assumed to embedded in the membrane core, in contrast to *barrel stave* model, where they are assumed to be in solvent medium. Since its first introduction, *barrel stave* was assumed to be central mechanism for commonly known peptides like *melittin*, *magainin* etc. [131]. However, with the advancement of experimental techniques like oriented circular dichroism, it was possible to resolve the positions of lipids and peptides more accurately. Yang et. al. 2001 [132] claimed that *alamethicin* might be the only AMP which follows the *barrel stave*. The authors proved that in *melittin* induced pores, the centre of mellitin lies closer to the membrane core.

- *Carpet like action*: This model was introduced to explain the permeability increase in the mammalian membrane by the effect of peptide *cecropin P1*. The structure of this AMP is also α helical. However, using Fourier-transform infrared (FTR), the authors of Gazit et. al. 1996 [133] found that the orientation of these peptides when interacting with the bilayer was parallel to bilayer interface.

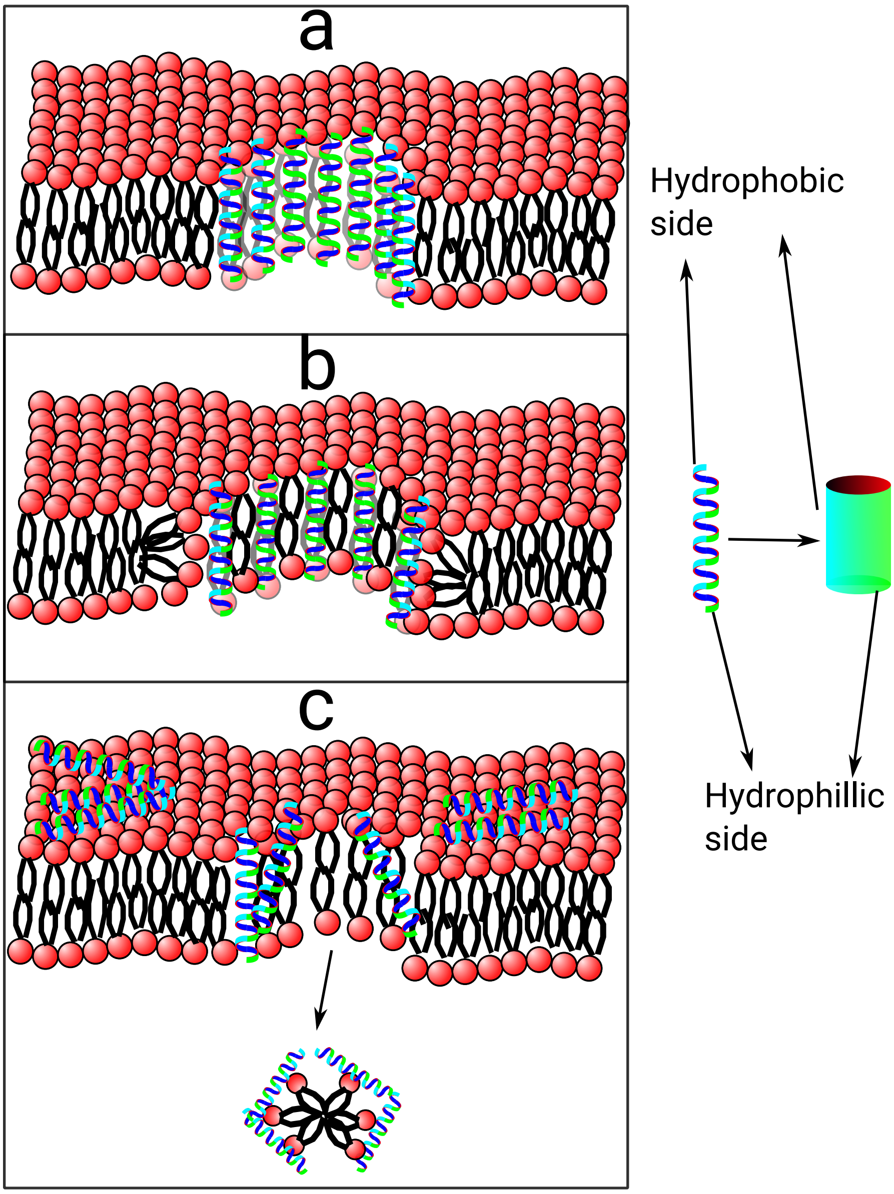

FIGURE 4.1 The schematic diagram of various models for the interaction of different kind of antimicrobial peptides with the membranes. (a) Barrel stave model (b) Toroidal pores (c) Carpet model (see text). The figure on the *right panel* shows the approximations of a helical AMP structure into a solid cylinder structure in the coarse-grained simulations by Illya et. al. 2008 [126].

Synthetic copolymers with antimicrobial action

In Cornell et. al. 1965 [134], one of the first artificially prepared copolymers was synthesized which had antibacterial activity. The authors aimed at testing the effects of polymerization of a antimicrobial compound called *tropolone*. The concept of synthesizing a polymer out of the antimicrobial compounds has been quite commonly used in experimental studies. This has been successful in some cases in increasing the activity of the materials and in other cases completely opposite results have been found. For example, a polymer of Penicillin V and Cephradine show prolonged activity [135]. However, the polymerization of *pyridinium* based antibiotics was found not to kill bacteria at all but just capture them by adsorption [136]. These copolymers were also found to be water-insoluble, therefore, alternatively were used in the water purification.

Another type of synthetic copolymers has the bioactive molecules attached to them, but the copolymer backbone is not active. The inclusion of antimicrobial material with the polymer serves various purposes, like long-term storage of the material, protection of against change of properties in temperature fluctuations, controlled release of substances etc. For example, *tetracyline*, a commonly used antibiotic polymerized with PVP shows the antibacterial activity for 4 weeks [137]. The release rate could be controlled in the range of 5 days to 5 weeks by using a different kind of backbone copolymers. Grunlan's group [138] have synthesized alternating copolymers with one monomer type as a natural and other monomer type being synthetic antimicrobial. Some of these synthesized copolymers retain the activity for even 3 months. The excellent reviews on the synthetic copolymers with and without bioactive molecules can be found in Bonilla et. al. 2012 [139] and Siedenbiedel et. al. 2012 [140].

The synthetic antimicrobial copolymers can also be synthesized by deriving different copolymers from natural peptides. In some cases, it has been found that the synthetic copolymers with the non-helical conformation of natural peptides act as better antimicrobial agents. Schmitt et. al. 2007 [141] found that a flexible copolymer with random sequence has about 5 fold activity in comparison with the naturally occurring peptides like *magnine*. Similar behaviors were shown by Werner et. al. 2015 [58] using BFM simulation. In Werner et. al. 2015, the copolymers with random sequences cause an increase in the solvent permeability in the model membranes. The *facially amphiphilic* are copolymers which have a side group attached to every monomer on the backbone. One face of the copolymer has a different amphillicity than the other face [142]. Few examples of these are typically polynorbornene and phenylene backbone derivatives, where the backbone is hydrophobic and side groups have hydrophilic [143], Fig.(4.2).

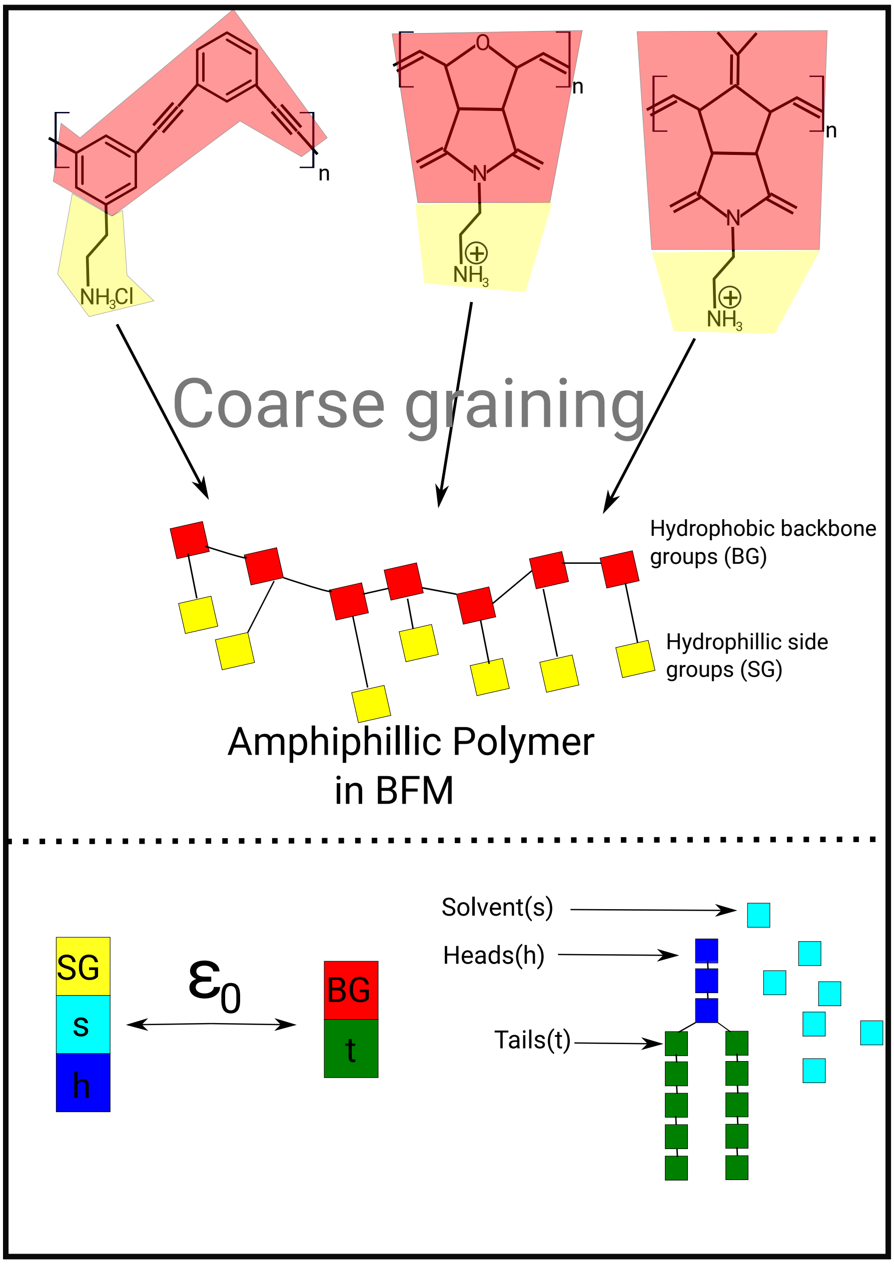

FIGURE 4.2 *Top panel*: The schematic diagram showing coarse-graining (section 1.3) of copolymers of phenylene ethylene backbones (*first*) and polynorbornene derivatives (*last two*) (synthesised by Gaberiel et. al. 2009 [143]) to the generic copolymers used in the BFM based simulations. In the *lower panel*: The schematic representation of the interaction model for lipids (h, t), solvent (s), and amphiphilic copolymers (SG, BG).

4.2 Simulation setup

In the simulations described, the length of lipid tails has been set as $L_t = 5$; mean lattice occupancy of 0.5 in a simulation box of size $64l \times 64l \times 64l$ has been used. The box has periodic boundaries in the plane of membrane, and non-periodic boundaries in the perpendicular direction. Two systems are investigated with number of lipids, N_{lipids}, and number of copolymers, N_p:

- *System A*: $N_{lipids} = 260$, N_p varying from $N_p = 0$ to $N_p = 40$.
- *System B*: $N_{lipids} = 270$, N_p varying from $N_p = 0$ to $N_p = 120$.

The choice of above two systems allows us to show that the copolymers can act on the line tension and form or stabilize pores. In the case of the system A, the pores are in metastable state, which exists at the boundary of pore state stabilisation, Fig.(3.8). An increase in tension via decrease of N_{lipids} will shift the membrane into a state where a pore is completely stable. For example, in Fig.(3.8), for $L_t = 5$, this would happen for $a_f > a_{f,\mathrm{pore}} = 31.5a^2$ ($N_{lipids} < 260$).
The system B is at a lower tension and a_f is lower than $a_{f,\mathrm{pore}}$, hence, the membrane is intrinsically closed.

4.3 Types of copolymers

The copolymers which mimic AMP consist of flexible chains with a backbone length, L, between 5 and 11 monomers, and one side group monomer (SG) attached to each of the backbone monomer (BG), see Fig.(4.2) and Fig.(4.3). There are two choices of copolymer possible: type-1 where BG is hydrophobic and SG is hydrophillic and type-2 where BG is hydrophillic and SG is hydrophobic. The simulation test run of bilayers with copolymer reveal that the copolymers of type-2 suppresses the probability of appearance of pore in a metastable pore of system A, Fig.(4.3). In contrast, type-2 do the opposite and increase this probability, also discussed in section 4.5.4. The histograms are prepared from the solvent permeability values collected from intervals of 15000MCS for the simulated systems of 10^8 MCS.

4.3.1 Micellization of copolymers

To understand the differences in Fig.(4.3), the two types of copolymers are further studied by simulating them in the pure solvent environment, Fig(4.4). In the pure solvent,

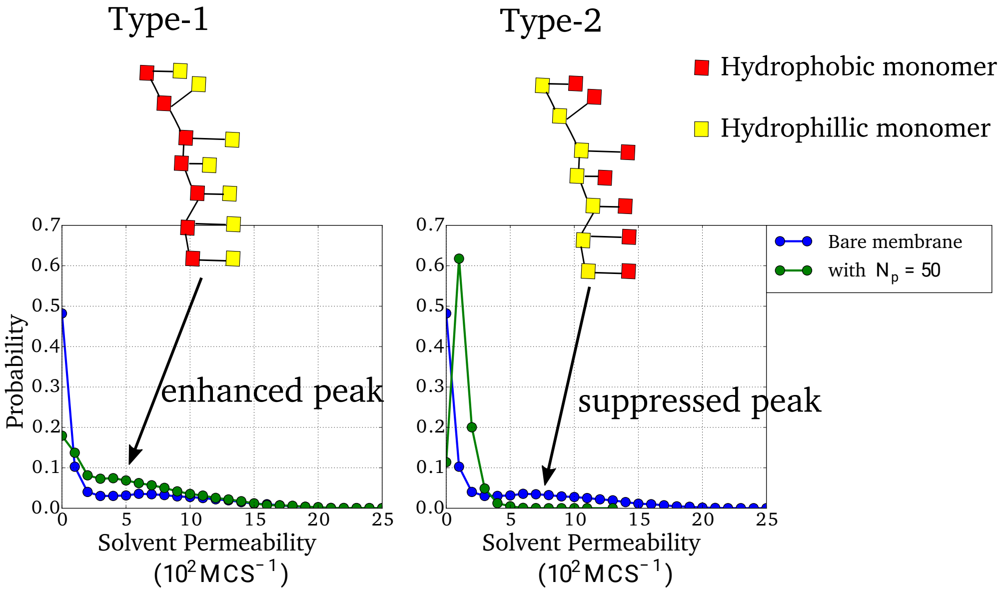

FIGURE 4.3 The probability distribution, $\mathcal{P}(P_s)$ of solvent permeability, P_s, in the interaction with different type of the copolymers with the membrane in system A. These plots show the effect of copolymers of type-1 and type-2 on $\mathcal{P}(P_s)$ of solvent permeability in comparison with $\mathcal{P}(P_s)$ of the bare membrane. The bell shaped peak at the higher values of P_s ($P_s \gg 0$) represents the presence of a pore. As one can observe, type-1 enhances the pore formation and whereas type-2 suppresses it. The length of the copolymer was chosen to be 7.

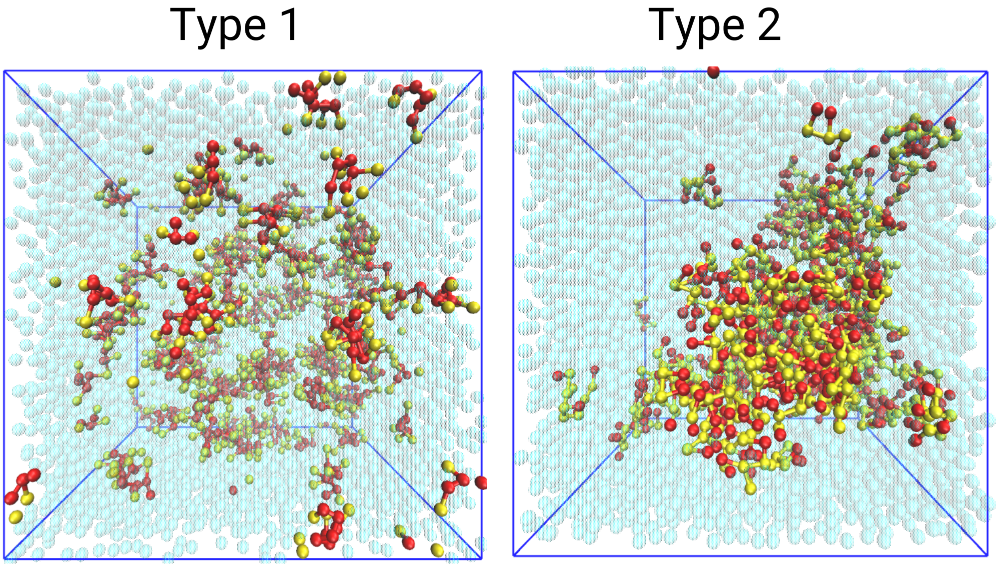

FIGURE 4.4 The snapshots of the two types of the copolymers simulated in a pure solvent environment. The red monomers are hydrophobic and the yellow monomers are hydrophillic, see Fig.(4.3), semi transparent blue monomers represent explicit solvent. Type-1 mostly stay as single copolymers, however type-2 form micelles. $N_p = 100$ for presented snapshots. The length of the copolymer was chosen to be 7.

the copolymers form micelles. The micelles are the self-assembled structures formed by amphiphilic molecules. The phospholipids also form micelles readily in aqueous solution. They are generally spherical in shape with the hydrophobic core, and hydrophilic monomers occupying the surface of the sphere and are in contact with the solvent. Their typical size varies from 2-20nm. The triblock copolymers like *poloxamers* also form micelles in water, following a dynamic equilibrium model. The micelles in the solution always have some individual molecules which are dynamically attaching and detaching from the micelle. The simulation snapshots of our *facially amphiphilic* (section 4.1, synthetic copolymers) copolymers show a similar process, Fig(4.4). They are generally in spherical form, however, they can connect through the periodic boundaries to form the cylindrical micelles.

In a dynamic equilibrium model, we consider multiple equilibria existing between the micelles with total of N copolymers in a system [144].

$$\mathrm{M_1 + M_1} \overset{\mathcal{K}_2}{\rightleftharpoons} \mathrm{M_2 + M_1} \overset{\mathcal{K}_3}{\rightleftharpoons} \ldots\ldots \mathrm{M_{N-1} + M_1} \overset{\mathcal{K}_\mathrm{N}}{\rightleftharpoons} \mathrm{M_N} \tag{4.1}$$

where M_i represents a micelle containing i copolymers and $\mathcal{K}_i$'s are the equilibrium constants. The first equation above represents the two micelles containing one copolymer each (single copolymers) add up to produce a micelle containing 2 copolymers or vice versa in equilibrium ($\mathrm{M_1 + M_1 \rightleftharpoons M_2}$). The second equation states that a micelle containing 2 copolymers add up with a single copolymer to produce a micelle containing 3 copolymers and vice versa in equilibrium ($\mathrm{M_2 + M_1 \rightleftharpoons M_3}$) and so on. The value of $\mathcal{K}_i$ is related to the products and reactants via

$$\mathcal{K}_i = \frac{c_i}{(c_1)^i} \tag{4.2}$$

where c_i is the concentration of a micelle containing i copolymers. Above relation could be understood by looking at the value of $i = 2$.

$$\mathcal{K}_2 = \frac{c_2}{(c_1)^2} \tag{4.3}$$

The value of $\mathcal{K}_i$ is the ratio of the multiplication of the concentrations of the products and of the reactants. In the simplest assumption, one can define

$$\mathcal{K}_1 = \mathcal{K}_2 = \mathcal{K}_3 .... = \mathcal{K}_N = \mathcal{K} \tag{4.4}$$

This assumption has generally shown agreeable results in the case of less branched and mostly linear copolymers with almost equal hydrophobic and hydrophilic components [144]. These conditions are well satisfied by the construction of our amphiphilic copolymers. The average degree of association is defined by

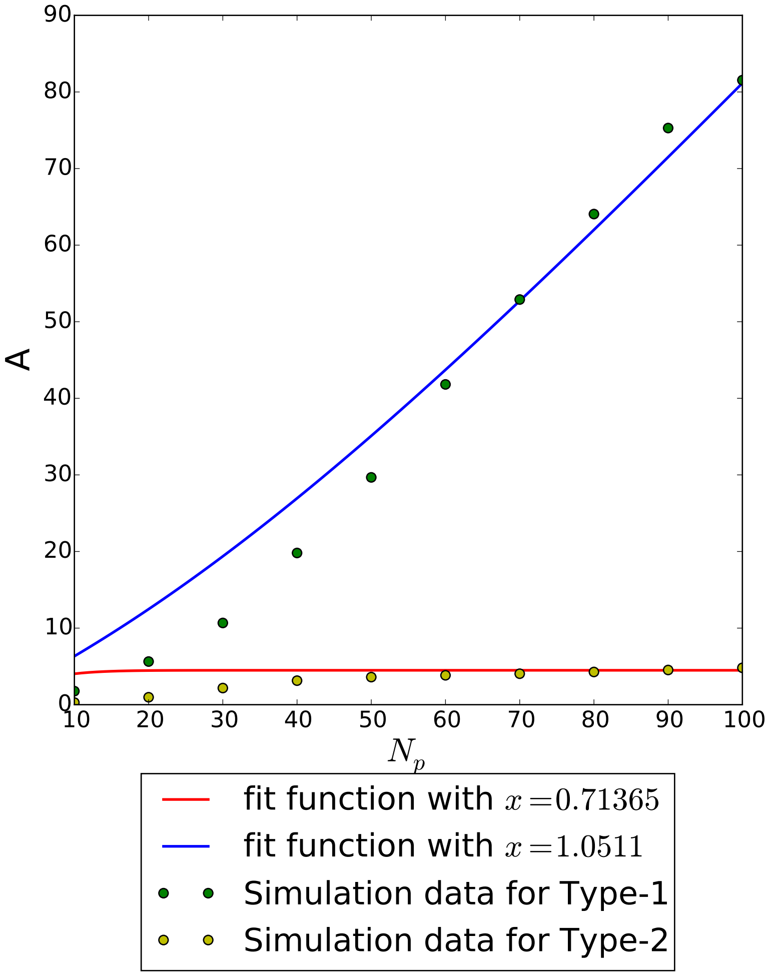

FIGURE 4.5 The average association number calculated using Eq.(4.5) from the simulations of type-1 and type-2 in the pure solvent environment. The fit functions have been calculated from the Eq.(4.7) and Eq.(4.6) using values of x described in legend. The length of the copolymer was chosen to be 7.

$$A = \frac{\sum_i ic_i}{\sum_i c_i} \tag{4.5}$$

The denominator in the above expression can be written as

$$\begin{aligned} A_D &= c_1 + c_2 + c_3 + c_4 + ...c_N \\ &= c_1 \left[1 + \mathcal{K}c_1 + (\mathcal{K}c_1)^2 + (\mathcal{K}c_1)^3 + ...(\mathcal{K}c_1)^{N-1}\right] \\ &= \frac{c_1(x^{N-1} - 1)}{x - 1} \end{aligned} \tag{4.6}$$

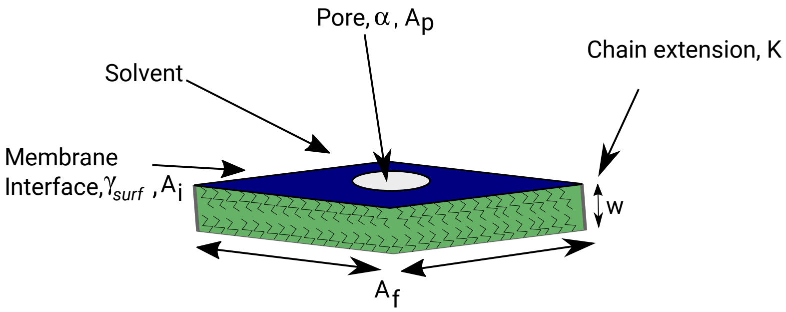

FIGURE 4.6 The model for the membrane characterized by the fixed area of frame, A_f; the area of pore, A_p; the line tension, α; the area of interface, A_i; the surface tension, γ_{surf}; the chain extension constant, K; and the width of the membrane, w.

where $x = \mathcal{K}c_1$. Similarly, the numerator can be written as

$$\begin{aligned} A_N &= c_1 \sum_{i}^{N-1} (i+1)x^i = c_1 \frac{\partial}{\partial x}\left(\frac{x(x^N - 1)}{(x-1)}\right) \\ &= c_1 \frac{Nx^{N+1} - (N+1)x^N + 1}{(x-1)^2} \end{aligned} \tag{4.7}$$

Using the expressions for A_D and A_N, A could be found. To show that the copolymers follow the model, we show the best fits for Eq.(4.5) calculated from the simulation and from the values of A_D and A_N in Fig.(4.5). The only fitting parameter is x for the expressions. The fitting values of x are given in the legend of Fig.(4.5). This indicates that micellization of copolymers in the solvent prevents them from being good pore inducing agents, Fig.(4.3). The readiness of micellization of a copolymer in pure solvent can be understood by comparing the $\mathcal{K}$ for both types. From Fig.(4.5), $x_{\text{type-1}} < x_{\text{type-2}}$ which means

$$(\mathcal{K}c_1)_{\text{type-1}} < (\mathcal{K}c_1)_{\text{type-2}} \tag{4.8}$$

implying $\mathcal{K}_{\text{type-1}} \ll \mathcal{K}_{\text{type-2}}$ as it is known that $(c_1)_{\text{type-1}} > (c_1)_{\text{type-2}}$ from the Fig.(4.4). Thus, in type-1, micelles are efficiently suppressed in comparison with type-2 copolymers. Therefore, all the copolymers refer to type-1 copolymers for the rest of the thesis.

4.4 Polymer brush model with a pore

As the systems described here involve membranes with a pore, the polymer brush model presented in section 3.5 has to be extended. A primary assumption of the model is that the membrane is flat. This is true for our systems, given by the fluctuation spectra, Fig.(3.3). The membrane is considered to be in an intact state, if the area of the pore, $A_p = 0$. In the first two terms on the right-hand side of the expression in Eq.(3.38), the area per lipid, a_l, has to be changed. As been already discussed $a_l = a_f - 2A_p/N_{lipids}$, and we shift to A_f instead of a_f for convenience. Hence, the area in the first term of Eq.(3.38) can rewritten as

$$F_{interface} = \gamma_{surf} \left(A_f - A_p\right) \tag{4.9}$$

Here, $A_f - A_p$ is the area of the interface, A_i. In the second term, the entropic contribution from the lipid tails, x as a function of A_p and A_f is

$$x(A_p, A_f) = \frac{a_{ext} N_{lipids}}{2(A_f - A_p)} \tag{4.10}$$

where N_t is number of tails in the system. The pore formation leads to a third contribution from the line tension, α, at the rim of the pore. The α is the energy per unit line, therefore, the free energy can be written by

$$F_{line} = 2\alpha\sqrt{\pi A_p} \tag{4.11}$$

The above expression is obtained by assuming a circular pore in the membrane. The radius of the pore, $r_p = \sqrt{A_p/\pi}$. The total free energy for a membrane with a pore is thus,

$$F = \gamma_{surf}(A_f - A_p) + K N_t F_{chains} + 2\alpha\sqrt{\pi A_p}\ . \tag{4.12}$$

where F_{chains} is given by Eq.(3.32), x in the F_{chains} is given by Eq.(4.10) and N_t is number of tails in the system. The free energy model mentioned above [145] has similarities with the model given by Tolpekina et. al. 2004 [146]. The authors in Tolpekina et. al. 2004 used harmonic approximation for the free energy of deformation the first two contributions on the right-hand side of Eq.(4.12).

A first conclusion from Eq.(4.12) is that tensionless state for a membrane attached to the frame does not allow a stable pore state in the membrane. At the tensionless state, the first two terms are in equilibrium with each other, and a pore of any size increases the last term, which increases the total free energy. A stable pore can only exist in a membrane if the total process leads to an overall decrease in the free energy. However, small unstable pores as a result of thermal fluctuations of the system are still possible. We study the systems, here, at a positive tension.

A membrane under positive tension can have a metastable pore state, which is stabilized by the line-tension active copolymers, thus switching between a closed and an open state. Amphiphilic copolymers can reduce the cost of opening a pore by occupying the space between tails and solvent and decreasing the line tension. The membrane thickness increases as the pore opens up, hence the line tension should be a function of pore radius. However, in the simplest approximation, we assume it to be only directly proportional to the number of copolymers, N_p, in the system. An observation from the simulations is that copolymers do not overcrowd the pore rim, but only weakly adsorb along the line. Thus,

$$\alpha(N_p) = \alpha_0 - \rho_{line} \cdot \Delta\alpha \tag{4.13}$$

where α_0 is the line tension of the membrane in a system without any copolymers, and ρ_{line} is the line density of copolymers. $\Delta\alpha$ is the reduction of line tension per copolymer which is directly related to the reduction in total free energy by copolymer adsorption on the pore. The value of α_0 is related to the bare membrane thickness and thus, also depends on the pore radius. The opening of the pore involves a nucleation free energy related to the rearrangement of lipids, as noted by Tolpekina et. al. 2004 [147]. This corresponds to a constant offset of free energy for the case of a single pore in Eq.(4.12). Thus, α_0 provides an averaged thermodynamic description of nucleation free energy of pore formation. The value of ρ_{line} is a monotonically increasing function of the copolymer concentration in the solvent and is given by the adsorption isotherm of copolymers at the boundary of the pore.

4.5 Results and discussions

4.5.1 Potential of mean force

In this section, we find out the free energy as a function of the area of the pore in our simulations, as suggested by Eq.(4.12). In order to quantify the area of a pore, we identify the lattice points in the projected membrane plane that are free of the tail monomers. A pore state is considered, if at least 10 such lattice points are connected. Since the small pores of $20\,l^2$ to $30\,l^2$ appear as a consequence of fluctuations even in the presence of the larger pores of the size $350\,l^2$ to $400\,l^2$, we use the weighted average (such that weights are equal to the pore sizes) of all the pore sizes appearing in a single configuration for the calculation of A_p. As a result we obtain the histograms representing the probability, $p(A_p)$, of finding a pore. For the calculations of the histogram we use a bin size of $20\,l^2$. The histograms are used to define the potentials of mean force according to

$$F(A_p)/k_BT = -\ln\left[p\left(A_p\right)\right] + const\ , \tag{4.14}$$

where the offset of the free energy is adjusted such that $F(0) = 0$. As the nucleation energy is involved in the opening of the pore, there is the option to use additional reaction coordinates for the free energy along with A_p for small pore sizes. Here, we follow a classical nucleation theory assumption and constrain free energy to be only described in the terms of A_p at all pore sizes. Moreover, as we observe only weak adsorption of copolymers in the intact state, it is adequate to assume that they do not affect the nucleation free energy of the bare membrane. The assumption $F(0) = 0$ sets up the reference value at $A_p = 0$ and provides a comparison of the free energy between the intact and pore state at the different concentration of polymers.

Discussion

The potentials of mean force obtained according to the Eq.(4.14) are displayed in the Fig. 4.7. We have compared the simulation results with the free energy model discussed in section 4.4

$$F(A_p) = \quad -\gamma_{surf} A_p - K N_t F_{chain} + 2\alpha(N_p) \cdot \sqrt{\pi A_p} \ , \tag{4.15}$$

where the closed state ($A_p = 0$) sets the free energy to $F(0) = 0$. The free energy model requires two adjustable parameters γ_{surf} and α, while A_f, B_t and N_t are given by the simulation setup. The area per lipid in the fully extended state, $a_{ext} = 10.30\, l^2$, and $K = 0.1$ as calculated in section 3.5. We use simulation data for $N_p = 0$ for least-square fits of γ_{surf} and α_0. Simulation results involving copolymers, $N_p > 0$, have been fitted by adjusting only the line tension, α. All parameters are summarized in table 4.1, and the results for $\alpha(N_p)$ are shown separately in Fig. 4.8(a).

In Fig. 4.7, we display the free energy as obtained using direct sampling with Eq.(4.14) as a function of the pore size. The upper row corresponds to system A (higher tension), and the lower row to system B (low tension). The left and the right site correspond to the shorter ($L = 7$) and the longer ($L = 11$) copolymers respectively. Without the presence of copolymers (black symbols in Fig. 4.7) system A shows a meta-stable pore-state at about $r_p \simeq 8l$, while in system B the pore-state is unstable. With the increasing number of copolymers, we observe a copolymer-induced stabilization effect of the pore-states as evidenced in the free energy profiles, Fig. 4.7, by a systematic reduction of the free energy for $r_p > 0$. For system A this corresponds to a deepening and a shift of the free energy of the pore state, denoted as F_p, in the following. In the system B, a finite copolymer concentration of about $N_p = 70 - 90$, depending of the copolymer length, is necessary to create a meta-stable pore-state, indicated by a local minimum in $F(r_p)$. Stable pores, $F_p < 0$, are observed for both systems A and B in the presence of a

parameter	system A	system B
A_f/l^2	4096	4096
N_t	520	540
a_{ext}/l^2	10.30	10.30
$\gamma_{surf}/(k_B T l^{-2})10^{-2}$	8	7.1
K	0.1	0.1

Table 4.1 Parameters applied when fitting Eq.(4.12) to simulation data (see text).

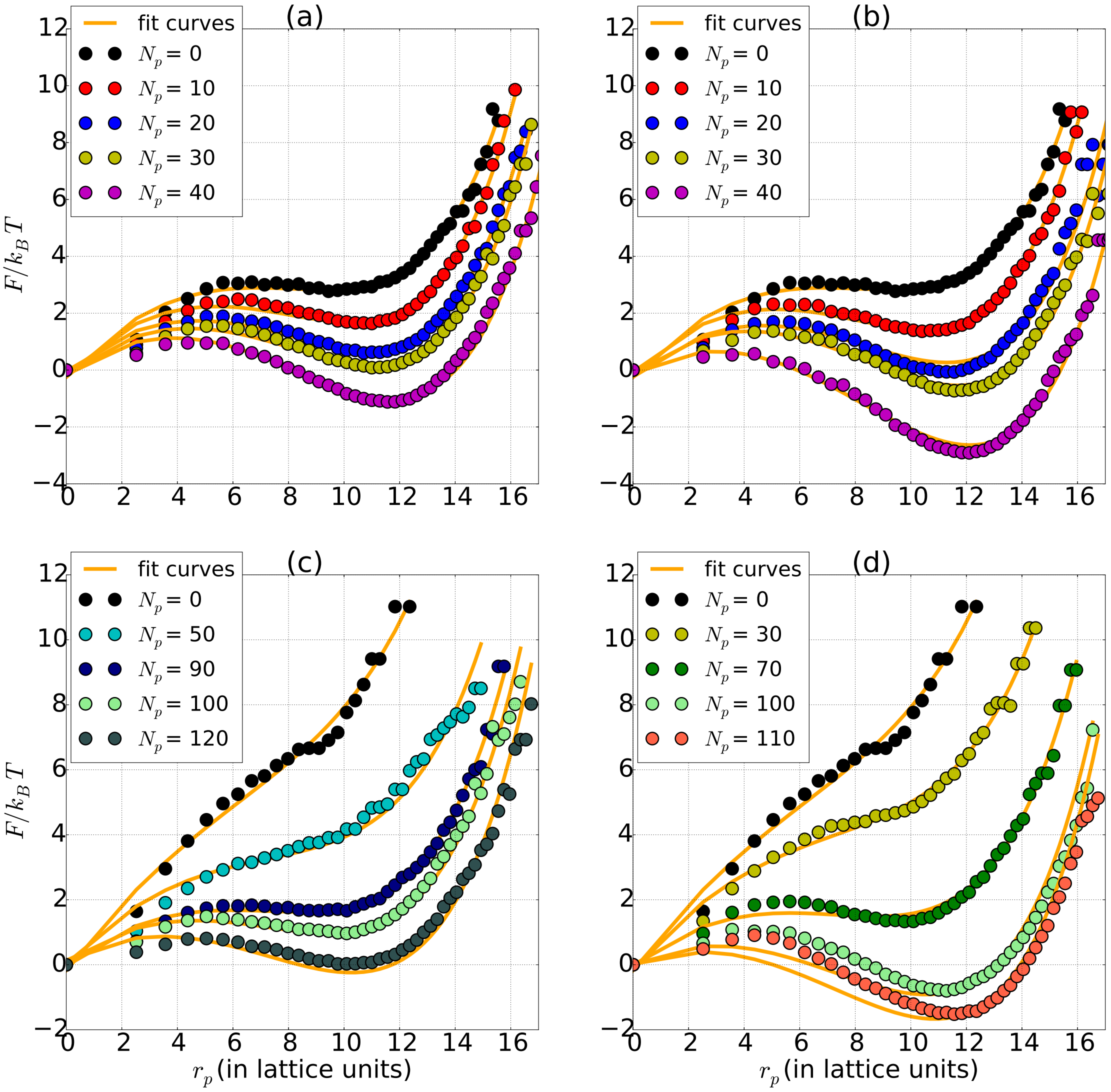

FIGURE 4.7 Potential of mean force versus radius of the pores as function of the length of the copolymers and the area of frame per tail (filled circles) and the fitted curves (orange lines). (a) system A, $a_f = 31.5l^2$, $L = 7$; (b) system A, $a_f = 31.5l^2$, $L = 11$; (c) system B, $a_f = 30.34l^2$, $L = 7$; (d) system B, $a_f = 30.34l^2$, $L = 11$.

sufficient number of copolymers. A similar discussion on the stability of pores was also reported by Tolpekina et. al. 2004 in their study of membrane pores induced by tension using an off lattice simulation model [147].

The enhanced stability of the pores observed with the increasing number of copolymers is consistent with the monotonically decreasing line tension $\alpha(N_p)$, as displayed in Fig. 4.8. The large pores, $r_p \gtrsim 14\,l$, can only be formed on the expense of an increase in the thickness of the membrane beyond its equilibrium value, and are thus suppressed. The finite size of the membrane limits the stable pore size at a value of about $12\,l$ here. System B displays metastable pores up to $N_p \simeq 100$, and stable pores occur eventually for $N_p \gtrsim 100$ for $L = 11$, and for $N_p \gtrsim 120$ for $L = 7$.

In Fig. 4.8(a), we display the best fits to the line tension $\alpha(N_p)$ using Eq.(4.15). The effect of the line tension reduction is stronger for larger L and thus the slopes for $L = 11$ are more negative than for $L = 7$ for both systems. The effect of copolymer length can be directly observed in Fig. 4.7: In the case of system A, for $N_p = 40$, the free energy difference between the pore and the intact state is $F_p \simeq -2k_BT$ for $L = 7$, and $F_p \simeq -4k_BT$ for $L = 11$. Similarly, system B reaches the coexistence state, i.e. $F_p \simeq 0\, k_BT$, for $N_p = 120$ with $L = 7$; while for $L = 11$ already with $N_p = 100$ one can observe a stable pore. Eventually for $N_p = 110$ the pore state is well pronounced with $F_p \simeq -2k_BT$. This dependence on L corresponds to the usual behavior of the adsorption isotherm of flexible polymers at an attractive interface [148, 149]. The longer chains lose a higher amount of free energy by adsorption on the expense of the translation degree of freedom only. Thus, one expects that $\Delta\alpha$ is increasing with L in Eq.(4.13). This corresponds to experiments by Kuroda et. al. 2009 [142] where an increase in the hemolytic activity has been reported, when the length of the copolymer chains is increased.

The higher stability of the closed state in system B, as compared to system A, can be directly seen by considering the number of copolymers, N_p, required for making the pore state coexist with the closed state, i.e. $F_p = 0$. Taking the example of $L = 7$ (lhs of Fig. 4.7) this requires about $N_p = 120$ for system B which is three times higher than the amount necessary to reach coexistence for system A ($N_p \simeq 40$). We note that the free energy barrier to form a pore in the absence of copolymers for system B is also about three times higher ($\approx 6k_BT$) as compared to system A ($\approx 2k_BT$). Another corollary for the stability of the membrane can be obtained from the line tensions of bare membranes, α_0, see Fig. 4.8. While for system A we obtain $\alpha_0 \simeq 0.59\, k_BTl^{-1}$, for system B it is $\alpha_0 \simeq 0.78\, k_BTl^{-1}$. A possible explanation is that larger line tension is the result of the thicker membrane in the case of system B which requires more contacts with the solvent for the same perimeter of the pore.

4.5.2 Size and probability of finding pores

Both the size and probability of appearance of the pore increase with the number of the copolymers, N_p. In Fig.(4.7), one can observe that potential barrier between the pore state ($r_p \simeq 12l$) and the closed pore state exists at around $r_p \simeq 4.5l$. Therefore, we consider small pores with $r_p \lesssim 4.5l = r_p^0$ as natural fluctuation of the closed state of the membrane, see Fig. 4.7. To analyze the pore distribution in the membrane we only consider events with $r_p > r_p^0$. In Fig. 4.9 and Fig. 4.10, we display the probability of an area element to belong to a pore with respect to the centroid of the pore as a color map. The procedure to obtain the distribution was as follows: After identifying all the

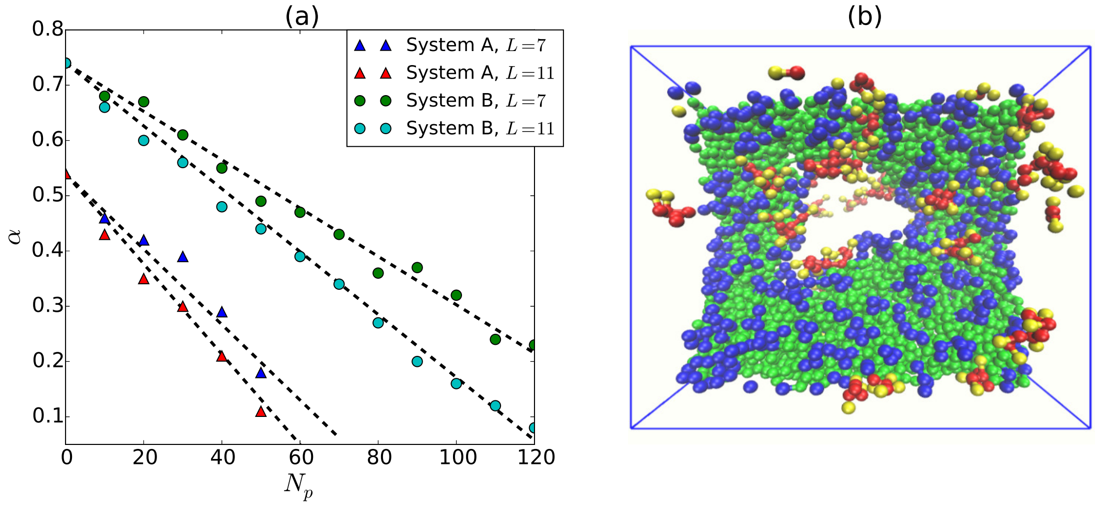

FIGURE 4.8 (a) Line tensions in systems A and B as functions of the number of copolymers in the simulation volume. The values of line tension have been calculated using least square fits of the of free energy plots, Fig. 4.7 with Eq.(4.15). The dashed lines corresponds to the best fits to Eq.(4.13) (b) A snapshot of an open pore state for system A with $N_p = 40$ and $L = 7$. The color scheme used for different monomer types is same as in Fig. 4.2. Solvent has been made invisible for convenience.

points of a pore with $r_p > r_p^0$, they are shifted such that the centroid (center of mass) of this set of points lies at the origin. This process is repeated and averaged over around 50,000 configurations which are each separated by 15000 MCS.

In Fig. 4.9, in the absence of copolymers, $N_p = 0$, there is a low probability, $p(r_p = 9\,l) \lesssim 0.4$ (light bluish), of finding a pore of radius about $r_p \simeq 9\,l$. This visualizes the metastability of the pore-state in the bare membrane under the tension. In Fig. 4.10, by contrast, for system B, there is only a weak pore activity even up to $N_p = 20$. If the number of copolymers is increased for system A, see $N_p = 10$ pores appear with moderate probability as indicated by the yellow region, $p(r_p) \gtrsim 0.6$. For $N_p = 40$ pores emerge with high probability (red region, $p(r_p) \gtrsim 0.8$). In the case of system B, pores with the moderate probability, $p(r_p) \gtrsim 0.6$, don't appear up to $N_p = 90$, and a high probability for pores can only be observed for $N_p = 120$.

4.5.3 Distribution of polymers with respect to the pore centroid

In Fig. 4.11 and Fig. 4.12, we show the 2D-pair correlation function between the centroid of the pore and the center of mass of the copolymers. To obtain the 2D-distribution of copolymers we have considered copolymers with their COM in a slit within a distance $\lesssim 10\,l$ from the midplane of the membrane. The resulting histograms have been rescaled with the surface density far away from the pore at distance $\gtrsim 25l$ from the centroid.

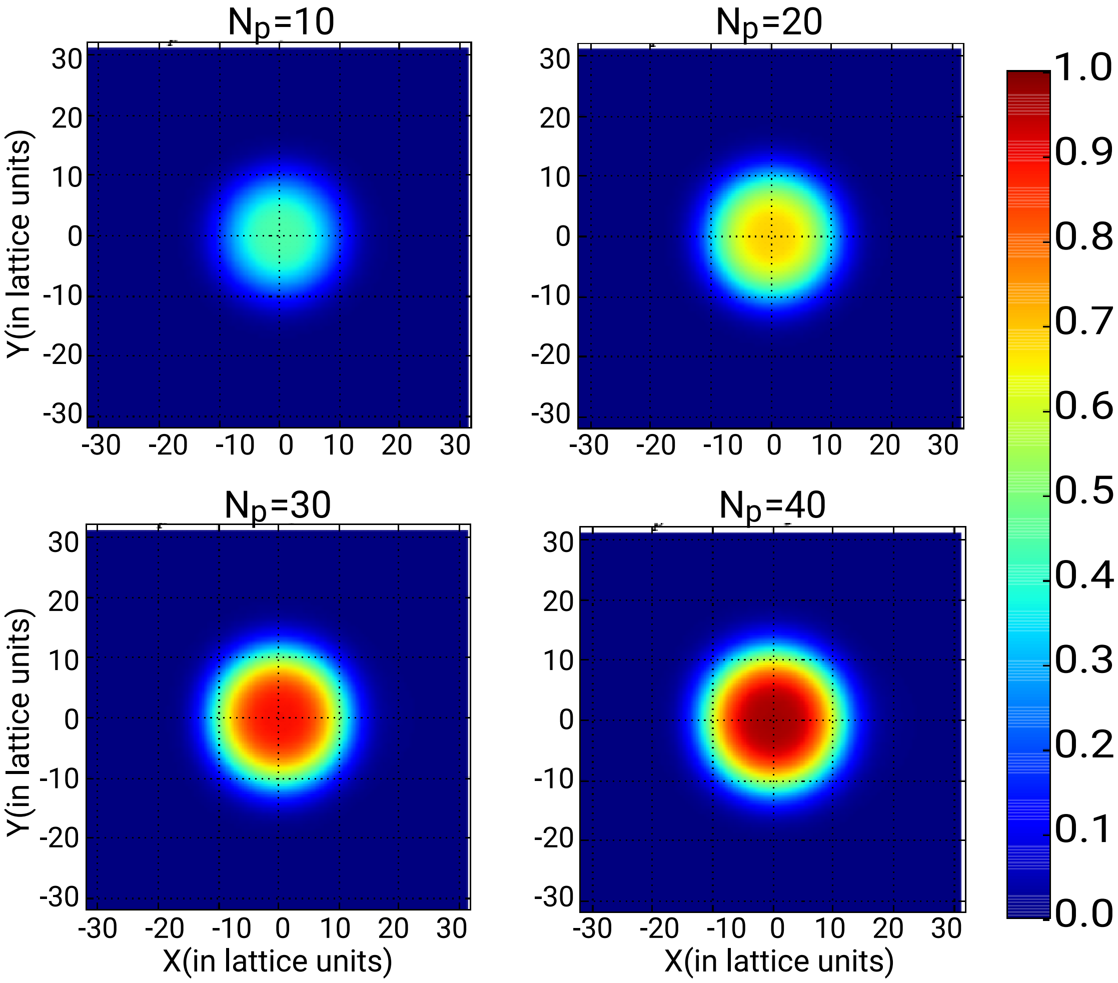

FIGURE 4.9 Probability for a point of the membrane to belong to a pore with the centroid of the pore at the origin as a function of the number of copolymers in the box. The color at coordinates (x, y) represents the probability (see colorbar) of finding a lattice point in a tail free region. These color plots are for system A (larger tension). The length of copolymers is chosen to be 7.

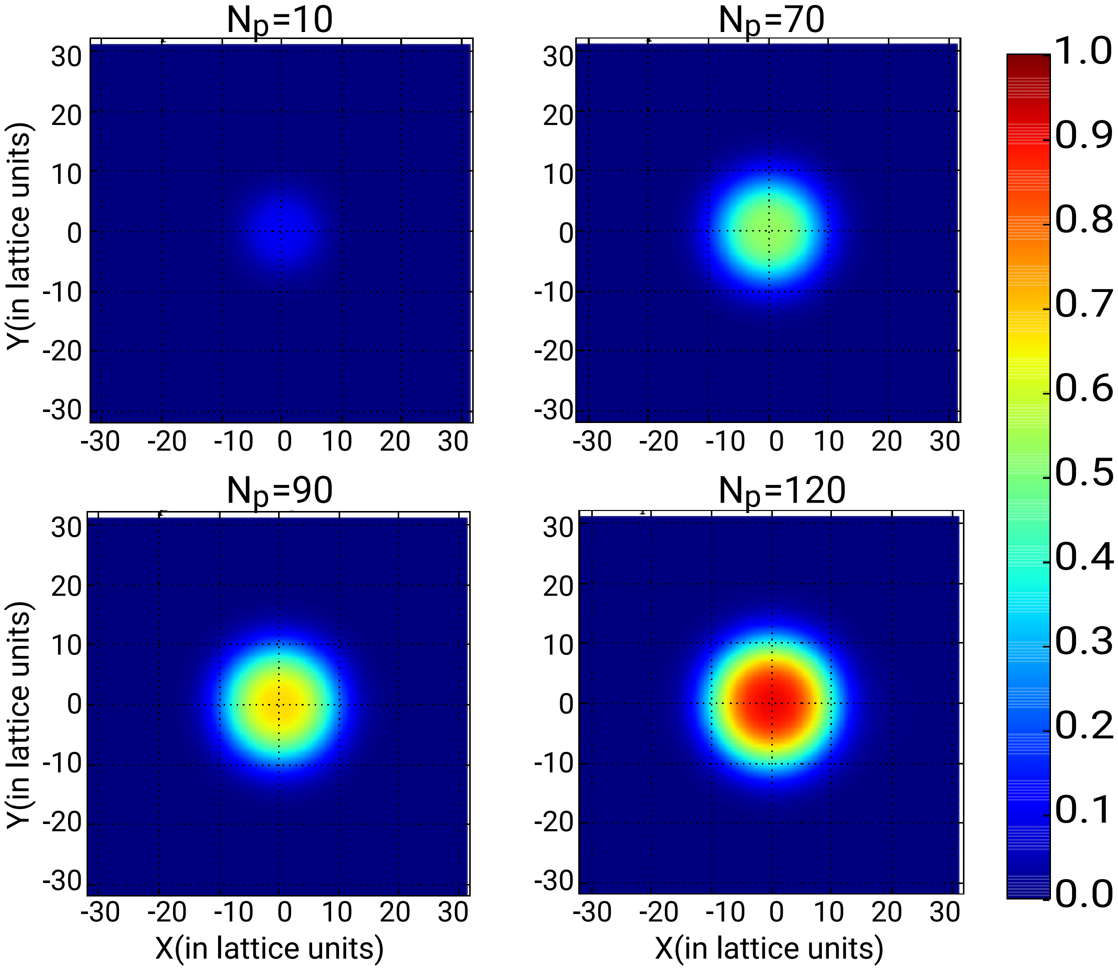

FIGURE 4.10 Probability for a point of the membrane to belong to a pore with the centroid of the pore at the origin as a function of the number of copolymers in the box. The color at coordinates (x, y) represents the probability (see colorbar) of finding a lattice point in a tail free region. These color plots are for system B (low tension). The length of copolymers is chosen to be 7.

Therefore, the results in Fig. 4.11 and Fig. 4.12 display the excess of the copolymer concentration in the pore region as compared to their concentration in the closed membrane area.

An enrichment of up to about 8 times in the pore-region as compared to the closed membrane state can be observed. This clearly indicates a physical adsorption process of the copolymers. Enrichment of copolymers takes place in ring-shaped forms at the rim of the pores. It is important to note that such rings should not be mistaken as "stave-like" arrangements as proposed for the operation of AMPs, Fig.(4.1). An individual snapshot of the pore would reveal only an occasional presence of copolymers, see Fig. 4.8 (b). The effect we observe here is the result of a weak dynamic adsorption process, which is still strong enough to reduce the line tension but does not lead to the dense packing of the copolymers. The maxima of the rings in Fig. 4.11 have comparable values, however, decreasing by about 10% with increasing pore sizes. This might be explained by increasing line and pore size fluctuations which smear out the distributions in the radial direction.

The different sizes of the pores are clearly reflected by the different ring diameters of the copolymer enrichment. The bluish yellow region in the interior of the pore indicates that copolymers also span the interior with moderate probabilities. It is interesting to note that the enrichment of copolymers can be well observed and is even most pronounced in the meta-stable state of the pore, which is particularly visible for system B with $N_p = 20$ (in Fig.4.12).

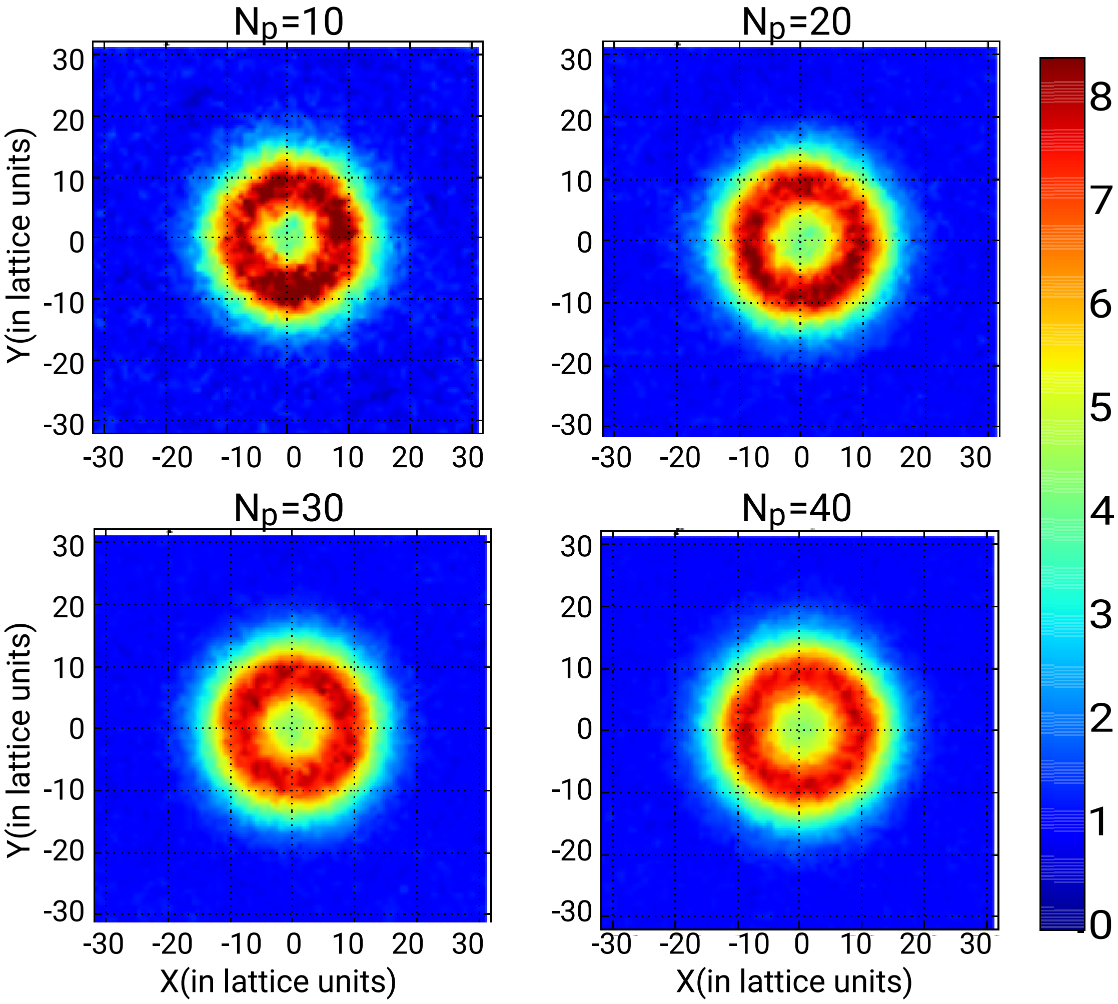

FIGURE 4.11 2-Dimensional pair correlation function between the centroid of the pore and the center of mass of the copolymers within a thin region in the proximity of the membrane surface. The value of unity (colorcode) corresponds to the natural appearance of copolymers in the proximity of the closed membrane. The plots presented are for system A (high tension). The length of copolymers is chosen to be 7.

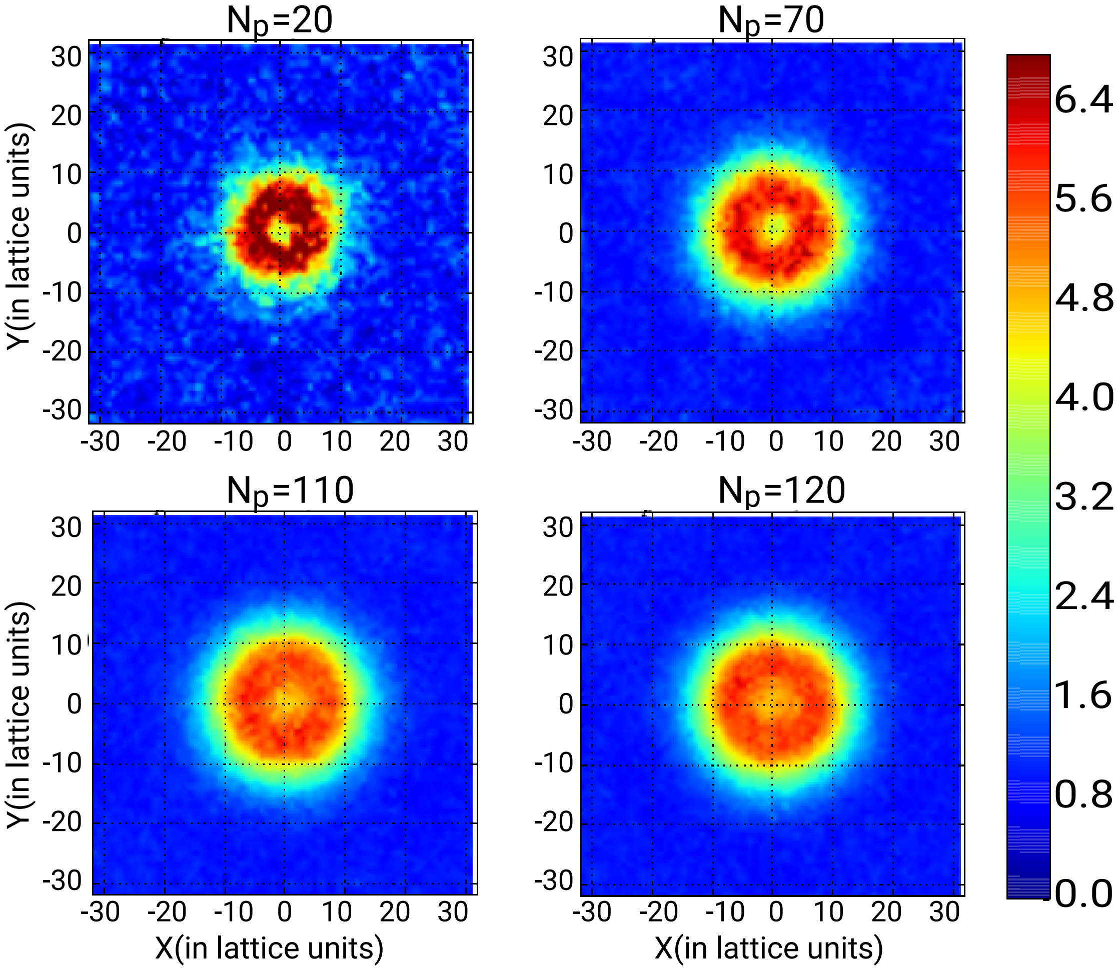

FIGURE 4.12 2-Dimensional pair correlation function between the centroid of the pore and the center of mass of the copolymers within a thin region in the proximity of the membrane surface. The value of unity (colorcode) corresponds to the natural appearance of copolymers in the proximity of the closed membrane. The plots presented are for system B (low tension). The length of copolymers is chosen to be 7.

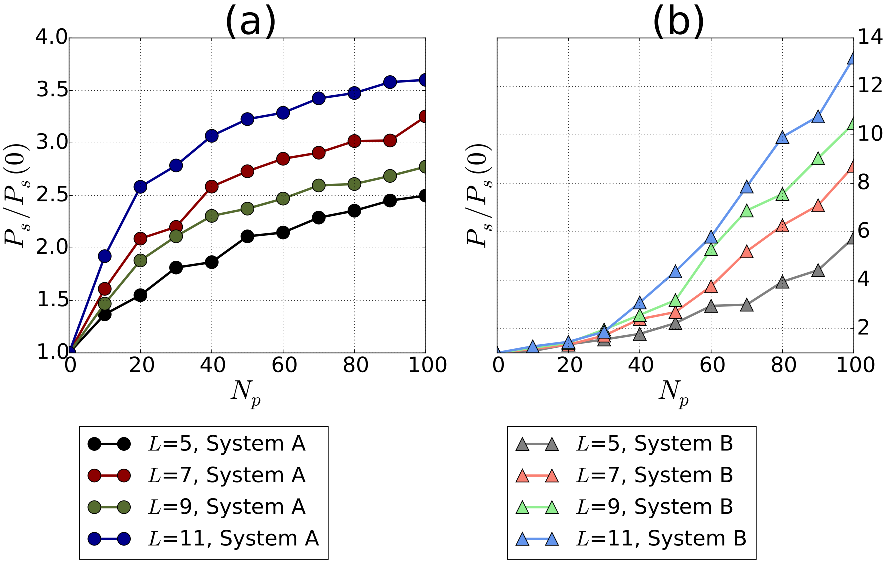

FIGURE 4.13 (a) Average rescaled permeability of solvent for system A and for system B in (b), P_s as a function of N_p. These permeabilities are rescaled with respect to the solvent permeability of bare membranes, i.e. $P_s(0)$. The solvent permeability is the measure of the number of solvent monomers passing from one side of the membrane to the other side per MCS as described in the text.

4.5.4 Average Solvent Permeability

This section illustrates the effect of copolymer length and concentration on the solvent permeability of the membranes at different tensions. In Fig. 4.13, we display the results obtained for the solvent permeability, P_s, rescaled by the permeability of solvent for the bare membrane, $P_s(N_p = 0)$, as a function of the number of copolymers, N_p. Here, we calculate the permeability of the solvent by the procedure as explained in section 3.6. Non-periodic conditions are implemented along the z axis for the convenience in the calculation of permeabilities. Potential of mean force calculations for bare membranes show that the free energy barrier for solvent permeation in system A is $3.27k_BT$ and in the system B is $4.01k_BT$. Hence, increasing the tension decreases the barrier, which also results in the values of $P_s(0)$ for system A, being about 6.5 times higher than for system B. Consequently, the $P_s(N_p)$, in the system B is always lower as compared to system A for the range of parameters studied. As expected, the permeability increases as N_p is increased. We note that P_s is the value averaged over the total membrane area. The excess of permeability is clearly much higher in the pore-region.

For system A, $P_s(N_p)$ displays a concave behavior while for system B it is convex. The rather weak effect of stable pores for $N_p > 20$ in system B is a consequence of the higher permeability in the intact state due to the occasional spontaneous opening of meta-stable pores, and due to the fact that pore sizes reach a maximum value in our finite system. In the case of system A the pore state is stabilized at $N_p = 40$, therefore the permeability saturates for higher copolymer concentrations. The enhancement in the stability of the pore-state with increasing length of the copolymer, L, is reflected by an earlier saturation for larger L.

System B displays a more dramatic behavior of the permeability with respect to the concentration of the copolymers which is expressed by an increase of about 14 times for the longer chains and highest copolymer concentrations. Moreover, the curvature of $P_s(N_p)$ is positive and even increases with the increase in L. We note that in system B a saturation of the pore size is not observed in our simulations, and thus a trend to increase the pore size with increasing copolymer concentration is maintained.

4.6 Conclusion

In this chapter, the lipid membranes interacting with facially amphiphilic copolymers are simulated. The structure of facially amphiphilic copolymers provides two simple choices of assignment of hydrophobicities; type-1, the backbone monomers are hydrophobic and side monomers are hydrophillic and type-2, the backbone monomers are hydrophillic and side monomers are hydrophobic. It is found that type-1 copolymers stabilize the pores. The type-2 copolymers occupy the pore, which could be observed by the reduction of solvent permeability as their concentration is increased. Thus, type-1 copolymers are used to investigate the pore formation in bilayers.

At sufficient concentrations of copolymers, a membrane with metastable pore state or an intact state shifts to stable pore state. This is also corroborated by the polymer brush model (extended to include a pore). The copolymers reduce the line tension by occupying the rim of the pore and reducing the unfavorable contacts between solvent and lipid tails. This is shown by color plots, Fig.(4.11-4.12), where a high probability of copolymers at the rim of pores (with respect to the intact membrane) can be observed. The increasing concentration of copolymers also enhances the size and probability of observing a pore in the membranes. The concentration required for observing stable pore in a membrane is higher for the membrane at a lower stress (lower a_f), in comparison with the membrane with the metastable pores (higher a_f). Furthermore, increasing the length of copolymer reduces the concentration of copolymers at which stable pores are observed in the membrane at the same stress.

The increased solvent permeability is observed as the pore state stabilizes. In the system with the membrane at weak tension, the relative increase in the solvent permeability (with respect to bare membrane) is stronger in comparison with membranes are higher tension (meta-stable pores). The solvent permeability in the system with the higher tension saturates at low concentrations of copolymers indicated by a concave shaped curve between solvent permeability and the number of copolymers in the simulation box.

Chapter 5

Summary and Outlook

5.1 Summary

In this work, coarse-grained Monte Carlo simulations have been used to understand the effects of length of lipids on the elastic properties of the membranes. The effect is specifically observed as a response of the surface tension of the membrane to different magnitudes of stresses. The interaction of the membranes with amphiphilic copolymers has also been investigated. The formation and stabilization of pores by the copolymers has been specifically demonstrated.

The simulations are performed in a periodic box of constant dimensions in the plane of the membrane. Varying the number of lipids, N_{lipids}, also varies the stress on the membrane. At high stresses (high a_f), the membrane shifts to a state where the pores are stable. At low stresses (low a_f), membrane assumes a buckling state. All these states are characterized by the changes in fluctuation tension, mechanical tension, solvent permeability and membrane thickness. The elastic constants like area compressibility and bending rigidity are found for investigated membranes. The simulations found larger values of the elastic constants for the membrane with longer tails. The increase in the bending rigidity and area compressibility with lipid tail length has also been observed in experiments by Rawicz et. al. 2000 [82].

In the case of weak stress with respect to the tensionless state, solvent permeability changes negligibility as the stress is increased. The simulation studies by Gauthier et. al. 2007 [111], fully atomistic simulations by Feller et. al. 1995 [112] and experiments by Vitkova et. al. 2004 [110] have shown similar behaviours of solvent permeability with respect to the stress. In this thesis, it is demonstrated, using Bond Fluctuation Method (BFM), that membranes with various lengths of tails have a similar region of weak stress where solvent permeability changes negligibility. Furthermore, a non linear increase with respect to stress is found at strong stresses. It is found that the membranes transit to pore state (as the stress is increased) more abruptly as the length of lipid tails is increased.

The stress anisotropy profile provides an insight to the variations of contracting stress and repulsive stress along the direction normal to membrane. These profiles have been investigated in the literature [100, 101, 150]. These studies have focused their analysis around the tensionless state. In this work, the profiles close to tensionless state reproduced the results from the literature. At positive surface tensions, the contraction stress due to hydrophobic interactions at the interface dominates in the whole membrane. At negative tensions, the repulsive stress due to the strong stretching of the lipid tails (in the direction normal to the interface) dominates the membrane. In a stable pore state, at the interface, contraction stress dominates whereas at the midplane, repulsive stress dominates due to presence of solvent in the pore. At the transition between the intact state (meta-stable pore state) and stable pore state, the stress anisotropy is almost zero at the midplane.

A polymer brush model (PBM) describes the transition of the membrane into the state with stable pores from the intact state with increasing stress. The surface tension derived from the PBM satisfies the simulation data reasonably well in the region of positive tension and at stresses where tails are weakly stretched. The analysis in this region suggests that the entropic contribution decreases as the length of tails is increased. The entropic part gives a repulsive contribution to the surface tension, favors the expansion of membrane with higher values of area per lipid. In contrast, the hydrophobic interactions favor lower area per lipid, thus, resist an increase in area per lipid. In the membranes with longer lipids, the tails are more relaxed in comparison with membranes with shorter tails. The decrease in the entropic repulsion increases the surface tension that the membrane can withstand before transiting into the pore state. The increased surface tension for longer lipids has also seen in the experiments of Rawicz et. al. 2000 [82]. This might potentially explain the reason that the micro-organisms like bacteria adapt to have longer tails in their cell membranes at extreme conditions like high pressure or temperature [16, 151]. In extremophiles, the longer tails help the microbes to resist higher stresses from the environment.

The formation of pores by spontaneous adsorption of copolymers (being in equilibrium with bulk) at the rim of the pore was directly sampled in the simulations presented in this work. This is difficult to achieve using more specific models [126, 128, 129, 152]. In comparison with the previous models which have been used to study this problem, here, only the hydrophobic effect was considered. The highly coarse grained nature of BFM reveals a universal mechanism for pore opening induced by amphiphilic flexible copolymers. The simulation method is able to reproduce the effects of other intrinsic parameters of the membrane like the surface tension, the effect of the length of copolymers, and the permeability of solvent, which have been observed in experiments and other theoretical studies.

The polymer brush model is extended by taking into account the line tension of a single pore. It suggests an increase in the stability of the pore state as the line tension is decreased. The amphiphilic copolymers act to reduce the line tension of the pore and, thus, switch the membrane from a meta-stable, or hidden, pore-state to a stable pore-state. In the weakly stressed membranes, a much stronger increase of solvent permeability due to the presence of copolymers was found in comparison with membranes which are already under higher stress. This happens as the membranes at higher stress display spontaneous opening of pores even in the absence of copolymers ($a_{f,\mathrm{pore}}$).

The membrane interchanges between the metastable and stable pore state at different concentration of the copolymers. This may explain the interchanging behavior of peptides between antimicrobial peptide (AMP) or cell-penetrating peptide (CPP), which has been reported in experiments [153]. An interesting scenario for the CPP-like behavior could be as follows: A transient (meta-stable) pore can be opened with the aid of a small concentration of CPP, which allows transport of cargo but does not lead to the destruction of the cell. However, an increased concentration of the copolymer turns the pore into a stable state, which is ultimately lethal for the living cell.

Furthermore, the variation of the membrane tension (or change in the area per lipid) influences the pore-formation by membrane active copolymers. An enhanced action of copolymers as the the stress is increased has been observed in experiments by Karal et. al. 2015 [154]. Increasing the length of copolymers also enhances the pore-forming capacity of the copolymers as also seen in experiments by Gaberiel et. al. 2009 [143], and which follows from the known physics of polymer adsorption. Finally, the analysis reveals that pore-formation via reduction of line-tension requires only weak adsorption of copolymers.

5.2 Outlook

A number of related future studies can be inspired from the present work. In the literature related to composition of cell membranes of extremophiles [16, 151], the unsaturation has been found to increase (along with the length) among the lipid tails. This could be investigated in future with the tools provided in the section 2.3, where bending potential could be set up such that bonded monomers prefer a non-collinear configuration. The interplay between the interaction and entropic contributions at different magnitudes of bending potential might give insights to reason that the extremophile microbes have tails with more unsaturated bonds in comparison with normal microbes. A hint to this behavior is given by the increase in area compressibility and bending rigidity with the length of tails. The increase is correlated to the decrease in flexibility of the membranes which is disadvantageous for functions of cell like fission, fusion etc [155]. Thus, there might be a balance point where unsaturation increases such that flexibility of the membrane is preserved, but at the same time, it can withstand larger stresses.

Generally in literature, the simulations [156] and other theoretical studies [157] related to pore formation in lipid bilayer (in the absence of copolymer interaction), suggest a nucleation process. Recently, this has also been described in terms of metastable prepores [158]. In the study described in chapter 4, nucleation part of mechanism of pore formation in membrane can be investigated in the future. Although, the polymer brush model fits reasonably well with the simulation data in the regions at large radii of pore, however, at low radii, it requires improvement. An understanding of the nucleation of pores by the copolymers might improve the fitting of simulation data at low radii. The copolymers might be spontaneously rearranging the lipids in the vicinity of region where the pore nucleates.

Appendices

A.1 Chemical potential of bilayer as a function of stress

A.1.1 Thermodynamic Integration

The thermodynamic integration is the method of calculating the free energy difference between states A and B. It is used when the path between A and B is expected to be a highly non linear or other complicated function of a parameter [39]. $\{r_i\}$ is the set of generalised coordinates on which these states depend upon. If the interaction energy at A is $U_A(\{r_i\})$ and at B is $U_B(\{r_i\})$, then a parameter $\lambda \in [0, 1]$ could be used to switch from one state to another.

$$U(\{r_i\}, \lambda) = (1 - \lambda)\ U_A + \lambda\ U_B \tag{A.1}$$

In simulations, λ is numerically increased from 0, where $U(\{r_i\}, 0) = U_A$ in small intervals of $\Delta\lambda$ to 1, where $U(\{r_i\}, 1) = U_B$. The chosen finite size of $\Delta\lambda$ decides the accuracy of the result of integration. If there is a path along one of the parameters, x_p, from A to B, the free energy, ΔF could be expressed as:

$$\Delta F = \int_{x_p(\lambda=0)}^{x_p(\lambda=1)} dx_p\ \frac{\partial F}{\partial x_p}\bigg|_{x_i=const.\text{ for } i\neq p} \tag{A.2}$$

Therefore, $\partial F/\partial x_p$ should to be non-divergent in the interval $[x_p(A), x_p(B)]$ for the integration to work. There could be more than one independent parameters along which free energy difference could be required. Few examples of x_i are volume, temperature, number of particles etc. and thus, $\partial F/\partial x_i$ would be pressure, entropy and chemical potential respectively. In general, if the integration along more than one parameter is required, then Eq.(A.2) is used sequentially one by one through all x_i's. The partition function (Eq.(2.2)) can be written in terms of λ.

$$Z(\lambda) = \int d\{r_i\}\ \exp(-U(\{r_i\}, \lambda)/k_B T) \tag{A.3}$$

The free energy is related to the partition function as

$$F = -k_B T \ln(Z) \tag{A.4}$$

From Eq.(A.3), $\partial F/\partial \lambda$ is given by

$$\frac{\partial F}{\partial \lambda} = \frac{1}{Z}\int d\{r_i\}\frac{\partial U}{\partial \lambda}\ \exp(-U(\{r_i\},\lambda)/k_B T) = \left\langle \frac{\partial U}{\partial \lambda} \right\rangle_\lambda \tag{A.5}$$

$\langle X \rangle_\lambda$ signifies ensemble average of X at a constant λ.

A.1.2 Ghost Chain Method

The chemical potential is the change in free energy with respect to exchange of particles, N.

$$\mu = \frac{\partial F}{\partial N} = \lim_{N\to\infty} \frac{F(N+1) - F(N)}{(N+1) - N} \tag{A.6}$$

using the relation in Eq.(A.4), $\mu = -k_B T \ln(Z(N+1)/Z(N))$. Here, $\mu = \mu_{id} + \mu_{ex}$, where μ_{id} is the ideal gas contribution containing only momentum part of Hamiltonian and μ_{ex} is excess contributions from potential energies the system.

$$\mu_{ex} = -k_B T \ln \int d\{r_i\} \exp(-(U(N+1) - U(N))/k_B T) = -k_B T \ln\langle \exp(U_t/k_B T)\rangle \tag{A.7}$$

where $U_t = U(N+1) - U(N)$ and $\langle .. \rangle$ signifies the ensemble average with respect to a system of N particles. Thus, μ_{ex} is the potential energy averaged over all the configurations of a inserted particle in a canonical ensemble of N particles with $N \to \infty$. This concept is exploited by the *Widom insertion method* [159] in simulations, where a particle is randomly inserted in the system of interest and the potential energy felt by it is sampled over large number of configurations. The calculation of μ_{ex} has been important to understand the phase behaviours of complex systems [160]. In the systems with low densities and single particles, Widom method gives acceptable results. However, in the dense polymer systems, there is a negligible probability of inserting a chain at random. In these system, widom method becomes unreliable. Some modified methods have been used to calculate μ in polymer systems, for example, *configuration bias monte carlo method* [161, 162] and *chain increment method* [163, 164]. Both of these methods rely on the increased probability of insertion if chain is “grown” within the simulation from the smaller chains. The method which is discussed in the present work uses “ghost chains” to calculate μ in the following. The method with “ghost chains” was first introduced by Müller et. al. 1994 [165] for athermal system and Wilding et. al. 1994 [166] for both athermal and thermal systems of polymers. In this method, there are N real chains and a ghost chain in the system. The ghost chain follows the restrictions governed by

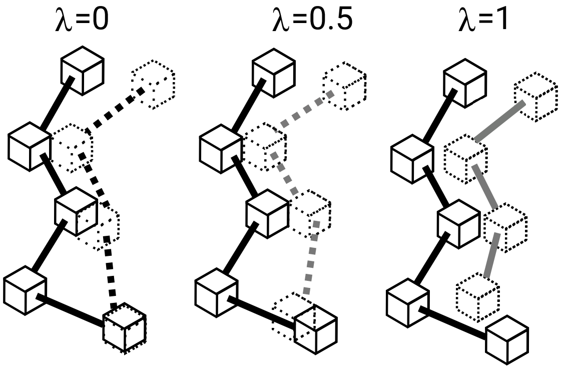

Figure A.1 The schematic diagram of the ghost chain method for the calculation of the chemical potential. The chain on the left (with the solid boundaries) is a real chain of a polymer system and on the right (with the dotted boundaries) is the ghost chain.

Eq.(2.7) on bond vectors and excluded volume for its own monomers. However, with the real chains it can overlap (partial excluded volume) and faces an effective repulsive potential of

$$U_{athermal} = -k_B T N_0 \ln(1-\lambda) \tag{A.8}$$

where N_0 are total number of doubly occupied lattice sites. Hence, at $\lambda = 0$, $U_{athermal} = 0$, the ghost chain does not interact with real chain at all and at $\lambda = 1$, $U_{athermal} \to \infty$, the ghost chain acts as any other real chain in the system. Similarly, the nearest neighbour interactions explained in the section 2.2.1 can also scaled with λ for the thermal potential.

$$U_{thermal} = \lambda U_N \tag{A.9}$$

where U_N is the interaction potential between the real chains of the system. If the values of λ are increased from 0 to 1, over M value of λ (with $M = 1/\Delta\lambda$), then the thermodynamic integration is performed and for large N, μ can be determined. The λ values can be changed from arbitrary λ_p to λ_q in set the $\{0, \lambda_1, \lambda_2 ... \lambda_{M-2}, 1\}$, by introducing a new metropolis move with transition probability:

$$\mathcal{T}(p \to q) = \min\{1, \exp(-\beta(N_0(\ln(1-\lambda_q) - \ln(1-\lambda_p)) + (\lambda_q - \lambda_p)U_{total}))\} \tag{A.10}$$

where U_{total} is the total interaction energy of the ghost chain before the move. However, as already discussed probability of insertion of the chain is low, $\mathcal{T}(p \to q)$ are negligible for almost all the values and system stays at $\lambda = 0$. To span the configuration space which is inaccessible by normal moves, positive weights, w_i have to be multiplied in calculating the probabilities.

$$\mathcal{T}_{weighted}(p \to q) = \min\{1, \mathcal{T}(p \to q) \times \exp(-(w_q - w_p))\} \tag{A.11}$$

To remove these weights from final value of μ, during the simulation, a histogram of probability at which each of M states is visited, $\mathcal{P}_i$, is created. For the simulation with weighted transition probabilities

$$\mathcal{P}_i = \frac{Z_i}{Z_{total}} \exp(w_i) \tag{A.12}$$

hence, the μ_{excess} from Eq.(A.6)

$$\mu_{excess} = \ln\left[\frac{\mathcal{P}_1 \exp(-w_1)}{\mathcal{P}_0 \exp(-w_0)}\right] \tag{A.13}$$

This method has been used in this work to calculate the chemical potential of the lipid membranes at different stresses. This has been described in Appendix A.1.3

A.1.3 Chemical potential of bilayer

Simulation details

The following parameters are varied for membranes with $L_t = 5$.

- $N_{lipids} = 250$ to $N_{lipids} = 300$

with one ghost lipid. There is another periodic box created in the larger periodic box ($64l \times 64l \times 64l$) which has the same dimension in xy plane (parallel to plane of membrane) but in z direction, with its centre at the midplane of membrane extends to $\pm 6l$($\sim$ membrane thickness), i.e. ($64l \times 64l \times 12l$). The new box is created to increase the accuracy in the calculation of chemical potential, μ. The smaller box only acts on the ghost lipid, Fig.(A.2(b)). Thus, it provides a continuous membrane environment to the lipid. In the case, if the smaller box is not implemented, the lipid leaves the bilayer and stays in the solvent, for all the values $\lambda < 0.7$, Fig.(A.2(a)). This is an artifact of the method of thermodynamic integration, as in real, $\lambda = 1$, lipids spend rarely any time in the bulk solvent environment.

In Müller et al. 1994 [165], the ghost box was not required. The polymer melt provides a homogeneous environment for ghost polymers. The simulations presented here were performed for 1×10^9MCS for all N_{lipids} and λ with the interval of $\Delta\lambda = 0.1$, Section **??**. The midplane for the ghost periodic box is updated after every 10000MCS.

Discussion

The calculation of chemical potential for lipid bilayers and micelles have been reported before in many simulation studies [167–170]. However, the effect of stress on chemical potential has been done only once by Grafmüller et. al. 2013[167]. In their study, authors

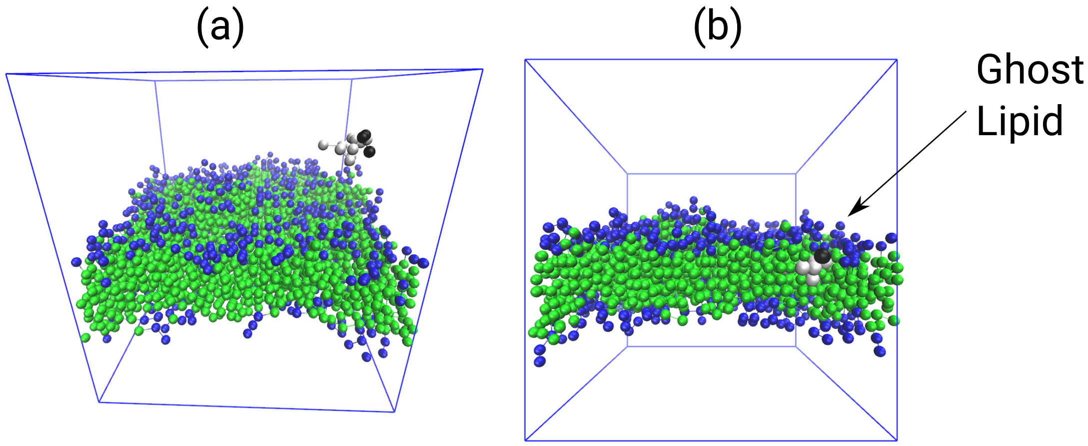

FIGURE A.2 (a) The snapshot from simulations showing the presence of ghost lipid without the periodic box for ghost lipid. (b) Same snapshot in (a) with ghost lipid periodic box implemented. System parameters, $L_t = 5$, $N_{lipids} = 300$ and 1 ghost lipid.

used the umbrella sampling method to find out the change in free energy for desorption, ΔF_{de}, of a lipid from a bilayer in tensionless state and a bilayer at positive tension state. They found that ΔF_{de} at a positive tension is more than in tensionless by an order of $7k_BT$. This decrease corresponds to BFM membranes Fig(A.3), however, the change in free energy ($\sim 1k_BT$) is quite low compared to Grafmüller et. al. 2013. This discrepancy could be potentially explained by coarse-graining in BFM, whereas Grafmüller et. al. 2013 performed atomistic simulations. A decrease in the chemical lipid with increasing tension is explained by polymer brush model, section 3.5. As observed in section 3.6 the membrane thickness decreases with tension. This relaxes the tail chains which decreases the stored entropic energy. It is known that entropic energy contributes largely to the chemical potential. Therefore, the chemical potential which is the free energy change from a good solvent environment to the bilayer environment is less for more relaxed chains when tension increases. The situation changes when the pore is stabilized. First, there is a different curvature at the pore rim which increases the insertion energy, also observed by Grafmüller et. al. 2013. The lipids face more nearest neighbor contacts with solvent at the interior of the pore, the free energy is averaged all the points in the membrane plane. The exploration of this technique to investigate further problems remains the subject of future work.

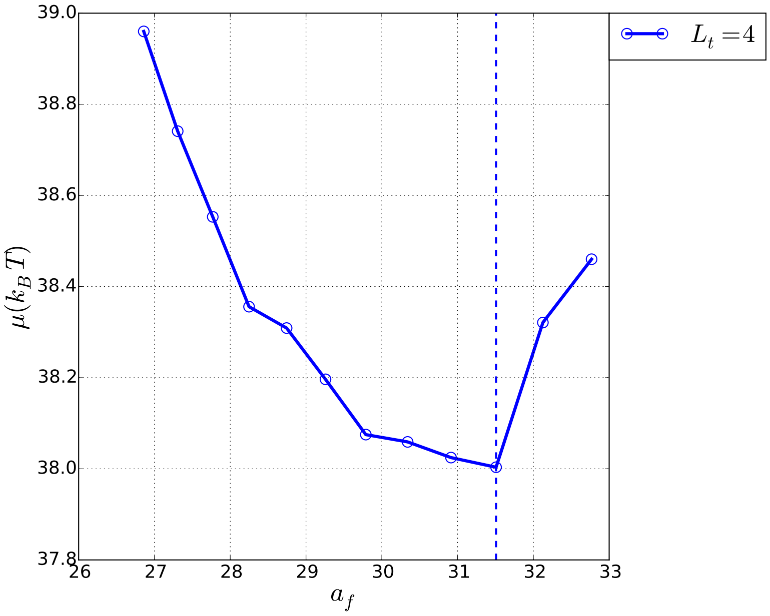

Figure A.3 Plot showing the change in the chemical potential with change in area per frame, a_f. The vertical dashed line shows the formation of the pore.

Bibliography

[1] T. Hartig. Das leben der pflanzenzelle, deren entstehung, vermehrung, ausbildung und auflösung. *Berlin: Albert Försterer*, 1844.

[2] C. Nägeli and C. Cramer. *Pflanzenphysiologische Untersuchungen.* Shulthess, Zrich, 1855.

[3] W. Pfeffer. *Osmotische Untersuchungen. Studien zur Zellmechanik.* W. Engelmann, 1877.

[4] C. E. Overton. *Studies of narcosis.* Chapman and Hall, 1991.

[5] E. Gorter and F. Grendel. On bimolecular layers of lipid on the chromacytes of the blood. *The Journal of experimental medicine*, 41(4):439–443, 1925.

[6] R. Brown. Observations on the organs and mode of fecundation in orchidae and asclepiadeae. *Trans Linn Soc (Lond).*, 16:685–743, 1833.

[7] W. Flemming. *Zellsubstanz Kern und Zelltheilung Leipzig.* FCW Vogel, 1882.

[8] J. D. Robertson. The ultrastructure of cell membranes and their derivatives. *Biochem. Soc. Symp.*, 16:3–43, 1959.

[9] J. F. Danielli and H. Davson. A contribution to the theory of permeability of thin films. *J. Cell Comp. Physiol.*, 5:495–508, 1935.

[10] S. J. Singer. *Structure and Function of Biological Membranes.* Academic Press, New York, 1971.

[11] M. Glaser, H. Simpkins, S. J. Singer, M. Sheetz, and S. I. Chan. Studies on freeze-etching of cell membranes. *Biochem. Soc. Symp.*, 721:65, 1970.

[12] S. Singer and G. L. Nicolson. The fluid mosaic model of structure of cell membranes. *Science*, 175:720–731, 1972.

[13] G. M. Cooper. *The cell, A molecular Approach, 2nd edition.* Sinauer Associates, Sunderland (MA), 2000.

[14] J. E. Rothman and J. Lenard. Membrane asymmetry. *Science*, 195(4280):743–53, 1977.

[15] T. Heimburg. *Thermal Biophysics of Membranes.* Wiley-VCH, 2007.

[16] J. L.C.M Vossenberg, A. J. M. Driessen, M. S. Costa, and W. N. Konings. Homeostasis of the membrane proton permeability in bacillus subtilis grown at different temperatures. *Biomembranes*, 1419:97–104, 1999.

[17] E. F. DeLong and A. A. Yayanos. Adaptation of the membrane lipids of a deep-sea bacterium to changes in hydrostatic pressure. *Science*, 228:1101–3, 1985.

[18] L. Tiefenauer and S. Demarche. Challenges in the development of functional assays of membrane proteins. *Materials*, 5(11):2205–2242, 2012.

[19] S. Demarche, K. Sugihara, T. Zambelli, L. Tiefenauer, and J. Vörös. Techniques for recording reconstituted ion channels. *Analyst*, 136:1077, 2011.

[20] N. J. Yang and M. J. Hinner. Getting across the cell membrane: An overview for small molecules, peptides, and proteins. *Methods Mol. Biol.*, 1266:29–53, 2015.

[21] H. Meyer. Zur theorie der alkoholnarkose.erste mittheilung. *Arch. fr Exp. Pathol. und Pharmakologie*, 42:109–118, 1899.

[22] T. Hanai and D. A. Haydon. The permeability to water of bimolecular lipid membranes. *Journal of Theoretical Biology*, 11:370–87, 1966.

[23] D. Mauzerall and A. Finkelstein. Light induced changes in the conductivity of thin lipid membranes in the presence of iodine and iodide ion. *Nature*, 224:690–692, 1969.

[24] H. Träuble. The movement of molecules across lipid membranes: A molecular theory. *The Journal of Membrane Biology*, 4(1):193–208, 1971.

[25] S. C. George and S. Thomas. Transport phenomena through polymeric systems. *Progress in Polymer Science*, 26:985–1017, 2001.

[26] A. Finkelstein and A. Cass. Permeability and electrical properties of thin lipid membranes. *The Journal of General Physiology*, 52(1):145–172, 1968.

[27] A. Missner and P. Pohl. 110 years of the meyeroverton rule: Predicting membrane permeability of gases and other small compounds. *ChemPhysChem*, 10:1405–1414, 2009.

[28] J. M. Diamond and Y. Katz. Interpretation of nonelectrolyte partition coefficients between dimyristoyl lecithin and water. *The Journal of Membrane Biology*, 17: 121–154, 1974.

[29] S.-J. Marrink and H. J. C. Berendsen. The movement of molecules across lipid membranes: A molecular theory. *The Journal of Physical Chemistry*, 98(15):4155–4168, 1994.

[30] A. H. Vries, I. Chandrasekhar, W. F. Gunsteren, and P. H. Hünenberger. Molecular dynamics simulations of phospholipid bilayers: influence of artificial periodicity, system size, and simulation time. *Journal of Physical Chemistry B*, 109(23):11643–11652, 2005.

[31] G. Zaccai, J. K. Blasie, and B. P. Schoenborn. Neutron diffraction studies on the location of water in lecithin bilayer model membranes. *Proceedings in National Academy of Science*, 72:376–380, 1975.

[32] R. Zwanzig. *Nonequilibrium Statistical Mechanics.* Oxford University Press, 2001.

[33] R. J. French. Unstirred layer effects on calculation of the potential difference across an ion exchange membrane. *Biophysical Journal*, 18:53–47, 1977.

[34] Y.-H. M. Chan and S. G. Boxer. Model membrane systems and their applications. *Current Opinion in Chemical Biology*, 11(6):581–587, 2007.

[35] G. W. Feigenson. Phase boundaries and biological membranes. *Annu Rev Biophys Biomol Struct*, 36:63–77, 2007.

[36] L. J. Pike. Model membrane systems and their applications. *The Journal of Lipid Research*, 44:655–667, 2003.

[37] T. Baumgart, A. T. Hammond, P. Sengupta, S. T. Hess, D. A. Holowka, B. A. Baird, and W. W. Webb. Large-scale fluid/fluid phase separation of proteins and lipids in giant plasma membrane vesicles. *Proceedings of the National Academy of Sciences*, 104:3165–3170, 2007.

[38] W. G. Noid. Perspective: Coarse-grained models for biomolecular systems. *The Journal of Chemical Physics*, 139:90901, 2013.

[39] D. Frenkel and B. Smit. *Understanding Molecular Simulation.* Academic Press, 2002.

[40] A. Arkhipov, P. L. Freddolino, and K. Schulten. Stability and dynamics of virus capsids described by coarse-graining modeling. *Structure*, 14:1767–77, 2006.

[41] J. C. Shelley, M.Y. Shelley, R. C. Reeder, S. Bandyopadhyay, and M. L. Klein. A coarse grained model for phospholipid simulations. *Journal of Physical Chemistry B*, 105:4464–4470, 2001.

[42] S. J. Marrink, A.H. de Vries, and A. E. Mark. Coarse grained model for semiquantitative lipid simulations. *Journal of Physical Chemistry B*, 108:750–760, 2004.

[43] G. S. Ayton and G. A. Voth. Hybrid coarsegraining approach for lipid bilayers at large length and time scales. *Journal of Physical Chemistry B*, 113:4413–4424, 2009.

[44] H. I. Ingólfsson, C. A. L. Jaakko, H. Jong J. U. D, S. M. Gopal, X. P., and S. J. Marrink. The power of coarse graining in biomolecular simulations. *WIREs Comput Mol Sci*, 14:225–248, 2014.

[45] R. K. Pathria and P. D. Beale. *Statistical Mechanics.* Elsevier, 1972.

[46] K. Kremer and K. Binder. The monte carlo simulation of lattice models for macromolecules. *Computer Physics Reports*, 7(6):259–310, 1988.

[47] J. Baschnagel, J.P. Wittmer, and H. Meyer. The monte carlo simulation of polymers: Coarse-grained models. *Computational Soft Matter*, 23:83–140, 2004.

[48] K. Binder and A. Milchev. Off-lattice monte carlo methods for coarse-grained models of polymeric materials and selected application. *Journal of Computer-Aided Materials Design*, 9:33–74, 2002.

[49] N. Madras and A. D. Sokal. Nonergodicity of local, length-conserving monte carlo algorithms for the self-avoiding walk. *J. Stat. Phys.*, 47:573, 1987.

[50] I. Carmesin and K. Kremer. The bond fluctuation method: a new effective algorithm for the dynamics of polymers in all spatial dimensions. *Macromolecules*, 21: 2819–2823, 1988.

[51] H. P. Deutsch and K. Binder. Interdiffusion and self diffusion in polymer mixtures: A monte carlo study. *J. Chem. Phys*, 94:2294, 1991.

[52] A. D. McNaught and A. Wilkinson. *IUPAC. Compendium of Chemical Terminology.* Oxford, 1997.

[53] G. Reddy and A. Yethiraj. Implicit and explicit solvent models for the simulation of dilute polymer solutions. *Macromolecules*, 39:8536–8542, 2006.

[54] M. Werner, J.-U. Sommer, and V. A. Baulin. Homo-polymers with balanced hydrophobicity translocate through lipid bilayers and enhance local solvent permeability. *Soft Matter*, 8:11714, 2012.

[55] M. Wengenmayr, R. Dockhorn, and J.-U. Sommer. Multicore unimolecular structure formation in single dendriticlinear copolymers under selective solvent conditions. *Macromolecules*, 49:9215–9227, 2016.

[56] C. Jentzsch, M. Werner, and J.-U. Sommer. Single polymer chains in poor solvent: Using the bond fluctuation method with explicit solvent. *J. Chem. Phys*, 138: 094902, 2013.

[57] S. Podogin, M. Werner, J. U. Sommer, and V. A. Baulin. Nanoparticle-induced permeability of lipid membranes. *ACS Nano*, 6:10555–10561, 2012.

[58] M. Werner and J.U. Sommer. Translocation and induced permeability of random amphiphilic copolymers interacting with lipid bilayer membranes. *Biomacromolecules*, 16:125–35, 2015.

[59] M. Müller and M. Schick. Structure and nucleation of pores in polymeric bilayers: A monte carlo simulation. *J Chem Phys.*, 105(18):8282–8292, 1996.

[60] J. Huang, Y. Wang, and C. Qian. Simulation study on the formation of vesicle and influence of solvent. *J Chem Phys.*, 131:234902, 2009.

[61] S. Ji and J. Ding. Spontaneous formation of vesicles from mixed amphiphiles with dispersed molecular weight: monte carlo simulation. *Langmuir*, 22:553–559, 2006.

[62] J. U. Sommer, M. Werner, and V.A. Baulin. Critical adsorption controls translocation of polymer chains through lipid bilayers and permeation of solvent. *Europhys. Lett.*, 98:18003, 2012.

[63] M. Werner, J. Bathmann, V. A. Baulin, and J.U. Sommer. Thermal tunneling of homopolymers through amphiphilic membranes. *ACS Macro. Lett.*, 6:247–251, 2017.

[64] H. Rabbel, M. Werner, and J. U. Sommer. Interactions of amphiphilic triblock copolymers with lipid membranes: Modes of interaction and effect on permeability examined by generic monte carlo simulations. *Macromolecules*, 48:4724–32, 2015.

[65] M. J. Field. *A Practical Introduction to the Simulation of Molecular Systems.* Cambridge University Press, 1999.

[66] A. R. Leach. *Molecular Modelling: Principles and Applications.* Prentice Hall, 2001.

[67] H.-D. Holtje, G. Folkers, W. Sippl, and D. Rognan. *Molecular Modeling: Basic Principles and Applications.* Wiley-VCH, 2003.

[68] W. L. Jorgensen and J. T. Rives. The opls [optimized potentials for liquid simulations] potential functions for proteins, energy minimizations for crystals of cyclic peptides and crambin. *J. Am. Chem. Soc.*, 110:1657–1666, 1988.

[69] W. L. Jorgensen, D. S. Maxwell, and J. T. Rives. Development and testing of the opls all-atom force field on conformational energetics and properties of organic liquids. *J. Am. Chem. Soc.*, 118:11225–11236, 1996.

[70] A. J. Markvoort, K. Pieterse, M. N. Steijaert, P. Spijker, and P. A. J. Hilbers. The bilayer-vesicle transition is entropy driven. *J. Phys. Chem. B*, 109:22649–22654, 2005.

[71] M. G. Martin and J. I. Siepmann. Transferable potentials for phase equilibria. 1. united-atom description of n-alkanes. *J. Phys. Chem. B*, 102:2569–2577, 1998.

[72] S. K. Nath, F. A. Escobedo, and J. J. de Pablo. On the simulation of vapor-liquid equilibria for alkanes. *J. Chem. Phys.*, 108:9905–9911, 1998.

[73] J. R. Errington and A. Z. Panagiotopoulos. A new intermolecular potential model for the n-alkane homologous series. *J. Phys. Chem. B*, 103:6314–6322, 1999.

[74] D. M. Bhawe, C. Cohen, and F. A. Escobedo. Formation and characterization of semiflexible polymer networks via monte carlo simulations. *Macromolecules*, 37: 3924–3933, 2004.

[75] H. P. Hsu. Monte carlo simulations of lattice models for single polymer systems. *J Chem Phys.*, 141:164903, 2014.

[76] K. Olbrich, W. Rawicz, D. Needham, and E. Evans. Water permeability and mechanical strength of polyunsaturated lipid bilayers. *Biophysical Journal*, 79: 321–327, 2000.

[77] S. Ollila, M. T. Hyvönen, and I. Vattulainen. Polyunsaturation in lipid membranes: dynamic properties and lateral pressure profiles. *The Journal of Physical Chemistry B*, 111:3139–3150, 2007.

[78] A. D.-Munoz, D. A. Fletcher, and O. D. Weiner. Use the force: Membrane tension as an organizer of cell shape and motility. *Trends Cell Biol.*, 23(2):4753, 2013.

[79] G. Soveral, R. I. Macey, and T. F. Moura. Membrane stress causes inhibition of water channels in brush border membrane vesicles from kidney proximal tubule. *Biology of the Cell*, 89:275–282, 1997.

[80] R. C. Shillcock and R. Lipowsky. Tension-induced fusion of bilayer membranes and vesicles. *Nature Materials*, 4:225–228, 2005.

[81] A. Grafmüller, J. Shillcock, and R. Lipowsky. Pathway of membrane fusion with two tension-dependent energy barriers. *Phys. Rev. Lett.*, 98:218101, 2007.

[82] W. Rawicz, K. C. Olbrich, T. McIntosh, D. Needham, and E. Evans. Effect of chain length and unsaturation on elasticity of lipid bilayers. *Biophysical Journal*, 79:328–339, 2000.

[83] W. Helfrich and R.-M. Servuss. Undulations, steric interaction and cohesion of fluid membranes. *Nuovo Cimento Soc. Ital. Fis. D*, 3:137–151, 1984.

[84] W. Helfrich. Steric interaction of fluid membranes in multilayer systems. *Z. Naturforsch.*, 33a:305–315, 1978.

[85] A. N. Pressley. *Elementary Differential Geometry.* Springer-Verlag London, 2010.

[86] D. Nelson, S. Weinberg, and T. Piran. *Statistical Mechanics of Membranes and Surfaces.* World Scientific Pub Co Inc; 2 edition, 2004.

[87] M. Deserno. Fluid lipid membranesa primer, 2007. URL `http://www.cmu.edu/biolphys/deserno/pdf/membrane_theory.pdf`.

[88] O. Farago. water-free computer model for fluid bilayer membranes. *The Journal of Chemical Physics*, 119(1):596–605, 2003.

[89] U. Seifert. Configurations of fluid membranes and vesicles. *Advances in Physics*, 46(1):13–137, 1997.

[90] I. R. Cooke and M. Deserno. Solvent-free model for self-assembling fluid bilayer membranes: Stabilization of the fluid phase based on broad attractive tail potentials. *The Journal of Chemical Physics*, 123:224710, 2005.

[91] R. Goetz, G. Gompper, and R. Lipowsky. Mobility and elasticity of self-assembled membranes. *Physical Review Letters*, 82:221–224, 1999.

[92] J. Stecki. Correlations in simulated model bilayers. *Journal of Chemical Physics*, 120:3508, 2004.

[93] A. Imparto. Surface tension in bilayer membrane with fixed projected area. *Journal of Chemical Physics*, 124:154714, 2006.

[94] Y. Y. Avital and O. Farago. Small membranes under negative surface tension. *Journal of Chemical Physics*, 142:1024902, 2015.

[95] W. Helfrich. Effect of thermal undulations on the rigidity of fluid membranes and interfaces. *J. Phys. France*, 46:1263–1268, 1985.

[96] L. Peliti and S. Leibler. Effects of thermal fluctuations on systems with small surface tension. *Phys. Rev. Lett.*, 54:1690–1693, 1985.

[97] K. Kleinert. Small membranes under negative surface tension. *Phys. Lett. B.*, 263: 114, 1986.

[98] M. Kummrow and W. Helfrich. Deformation of giant lipid vesicles by electric fields. *Physical Review A*, 44(12):8356–8360, 1991.

[99] R. Dimova. Recent developments in the field of bending rigidity measurements on membranes. *Advances in Colloid and Interface Science*, 208:225–234, 2014.

[100] E. Lindahl and O. Edholm. Spatial and energetic-entropic decomposition of surface tension in lipid bilayers from molecular dynamics simulations. *Journal of Chemical Physics*, 113:3882–3893, 2000.

[101] J. Gullingsrud and K. Schulten. Lipid bilayer pressure profiles and mechanosensitive channel gating. *Biophysical Journal*, 86:3496–3509, 2004.

[102] R. Goetz and R. Lipowsky. Computer simulations of bilayer membranes: Self-assembly and interfacial tension. *Journal of Chemical Physics*, 108:7397–7409, 1998.

[103] R. Phillips, T. Ursell, P. Wiggins, and P. Sens. Emerging roles for lipids in shaping membrane-protein function. *Nature*, 459:379–385, 2009.

[104] J. Stecki. Size dependence, stability, and the transition to buckling in model reverse bilayers. *Journal of Chemical Physics*, 125:154902, 2006.

[105] J.-B. Fournier and C. Barbetta. Direct calculation from the stress tensor of the lateral surface tension of fluctuating fluid membranes. *Physical Review Letters*, 100:078103, 2008.

[106] F. J. Schmid. Are stress-free membranes really "tensionless"? *European Physical Letters*, 95:28008, 2011.

[107] J. Neder, P. Nielaba, B. West, and F. Schmid. Coarse-grained simulations of membranes under tension. *The Journal of Chemical Physics*, 132:115101, 2010.

[108] W. Shinoda. Permeability across lipid membranes. *Biochimica et Biophysica Acta - Biomembranes*, 1858:2254–2265, 2016.

[109] A. Blicher, K. Wodzinska, M. Fidorra, M. Winterhalter, and T. Heimburg. The temperature dependence of lipid membrane permeability, its quantized nature, and the influence of anesthetics. *Biophysical Journal*, 96(11):4581–4591, 2009.

[110] V. Vitkova, J. Genova, and I. Bivas. Permeability and the hidden area of lipid bilayers. *European Biophysics Journal*, 33:706–714, 2004.

[111] A. Gauthier and B. Joos. Stretching effects on the permeability of water molecules across a lipid bilayer. *J. Chem. Phys.*, 127(10):105104–09, 2007.

[112] S. E. Feller, Y. Zhang, and R. W. Pastor. The tension of a curved surface from simulation. *Journal of Chemical Physics*, 103:10267, 1995.

[113] J. C. Mathai, S. T.-Nagle, J. F. Nagle, and M. L. Zeidel. Structural determinants of water permeability through the lipid membrane. *The Journal of General Physiology*, 131:69–76, 2008.

[114] O. Hamill and B. Martinac. Molecular basis of mechanotransduction in living cells. *The Journal of General Physiology*, 81:685, 2001.

[115] S. E. Feller, R. M. Venable, and R. W. Pastor. Computer simulation of a dppc phospholipid bilayer: structural changes as a function of molecular surface area. *Langmuir*, 13(24):6555, 1997.

[116] E. Evans, V. Heinrich, F. Ludwig, and W. Rawicz. Dynamic tension spectroscopy and strength of biomembranes. *Biophysical Journal*, 85:2342–2350, 2003.

[117] E. Evans, W. Rawicz, and B. A. Smith. Concluding remarks back to the future: mechanics and thermodynamics of lipid biomembranes. *Faraday Discuss.*, 161: 591–611, 2013.

[118] M. Rubinstein and R. H. Colby. *Polymer Physics.* Oxford University Press, 2003.

[119] C. L. Ventola. The antibiotic resistance crisis: Part 1: Causes and threats. *Pharmacy and Therapeutics*, 40(4):277–283, 2015.

[120] C. A. Michael, D. D. Howes, and M. Labbate. The antibiotic resistance crisis: causes, consequences, and management. *Front Public Health*, 2:145, 2014.

[121] A. A. Baharand and D. Ren. Antimicrobial peptides. *Pharmaceuticals*, 6:1543–1575, 2013.

[122] R. J. Dubos. Studies on a bactericidal agent extracted from a soil bacillus: I. preparation of the agent. its activity in vitro. *Journal of Experimental Medicine*, 70:1–10, 1939.

[123] J. G. Hirsch. Phagocytin: A bactericidal substance from polymorphonuclear leucocytes. *Journal of Experimental Medicine*, 103:589–611, 1956.

[124] X. Zhao, H. Wuand H. Lu, G. Li, and Q. Huang. Lamp: A database linking antimicrobial peptides. *PLoS One*, 8(6):18, 2013.

[125] G. Wang. Human antimicrobial peptides and proteins. *Pharmaceuticals*, 7(5): 545–594, 2014.

[126] G. Illya and M. Deserno. Coarse-grained simulation studies of peptide-induced pore formation. *Biophysical Journal*, 95:4163–73, 2008.

[127] C.-C. Lee, Y. Sun, and H. W. Huang. Membrane-mediated peptide conformation change from alpha-monomers to beta-aggregates. *Biophysical Journal*, 98(10): 2236–45, 2010.

[128] H. Leontiadou, A. E. Mark, and S. J. Marrink. Antimicrobial peptides in action. *Journal of American Chemical Society*, 128:12156–61, 2006.

[129] C. F. Lopez, S. O. Neilson, G. S. Srinivas, W. F. DeGrado, and M. L. Klein. Probing membrane insertion activity of antimicrobial polymers via coarse-grain molecular dynamics. *Journal of Chemical Theory and Computation*, 2:649–55, 2006.

[130] G. Ehrenstein and H. Lecar. Electrically gated ionic channels in lipid bilayers. *Quarterly Reviews of Biophysics*, 10(1):1–34, 1977.

[131] K. He, S. J. Ludtke, W. T. Heller, and H. W. Huang. Mechanism of alamethicin insertion into lipid bilayers. *Biophysical Journal*, 71:2669–79, 1996.

[132] L. Yang, T. A. Harroun, T. M. Weiss, L. Ding, and H. W. Huang. Barrel-stave model or toroidal model? a case study on melittin pores. *Biophysical Journal*, 81: 1475–85, 2001.

[133] E. Gazit, I. R. Miller, P. C. Biggin, M. S. Sansom, and Y. Shai. Structure and orientation of the mammalian antibacterial peptide cecropin p1 within phospholipid membranes. *Journal of Molecular Biology*, 258:860–70, 1996.

[134] R. J. Cornell and L. G. Donaruma. 2-methacryloxytroponones. intermediates for synthesis of biologically active polymers. *Journal of Medical Chemistry*, 8:388–90, 1965.

[135] A. Nathan, S. Zalipsky, S. I. Ertel, S. N. Agathos, M. L. Yarmush, and J. Kohn. Lysine and polyethylene glycol: A new family of functionalized drug carriers. *Bioconjugate Chemistry*, 4:54–62, 1993.

[136] N. Kawabata. Capture of microorganisms and viruses by pyridinium-type polymers and application to biotechnology and water-purification. *Progress in Polymer Science*, 17:1–34, 1992.

[137] L. E. Bromberg, D. K. Buxton, and P. M. Friden. Novel periodontal drug delivery system for treatment of periodontitis. *Journal of Controlled Release*, 71:251–259, 2001.

[138] J.C. Grunlan, J. K. Choi, and A. Lin. Antimicrobial behavior of polyelectrolyte multilayer films containing cetrimide and silver. *Biomacromolecules*, 6:1149–53, 2005.

[139] A. M.-Bonilla and M. F.-García. Polymeric materials with antimicrobial activity. *Progress in Polymer Science*, 37:281–339, 2012.

[140] F. Siedenbiedel and J. C. Tiller. Antimicrobial polymers in solution and on surfaces: Overview and functional principles. *Polymers*, 4:46–71, 2012.

[141] M. A. Schmitt, B. Weisblum, and S. H. Gellman. Unexpected relationships between structure and function in α,β-peptides: Antimicrobial foldamers with heterogeneous backbones. *Journal of American Chemical Society*, 126:6848–49, 2004.

[142] K. Kuroda, G. A. Caputa, and W. F. DeGrado. The role of hydrophobicity in the antimicrobial and hemolytic activities of polymethacrylate derivatives. *Chem. Eur. J.*, 15:1123–33, 2009.

[143] G. J. Gaberiel, J. A. Maegerlein, C. F. Nelson, J. M. Dabkowski, T. Eren, K. Nusslein, and G. N. Tew. Comparison of facially amphiphilic versus segregated monomers in the design of antibacterial copolymers. *Chem. Eur. J.*, 15:433–39, 2009.

[144] R. J. Hunter. *Foundations of Colloid Science.* Oxford Science Publications, 1990.

[145] A. Checkervarty, M. Werner, and J. U. Sommer. Formation and stabilization of pores in bilayer membranes by peptide-like amphiphilic polymers. *Soft Matter*, 14: 2526–2534, 2018.

[146] T. V. Tolpekina, W. K. D. Otter, and W. J. Briels. Simulations of stable pores in membranes: system size dependence and line tension. *Journal of Chemical Physics*, 121:8014–20, 2004.

[147] T. V. Tolpekina, W. K. D. Otter, and W. J. Briels. Nucleation free energy of pore formation in an amphiphilic bilayer studied by molecular dynamics simulations. *Journal of Chemical Physics*, 121:12060–66, 2004.

[148] E. Bouchaud and M. Daoud. Polymer adsorption: concentration effects. *J. Phys. France*, 48:1991–2000, 1987.

[149] R. Descas, J.U. Sommer, and A. Blumen. Concentration and saturation effects of tethered polymer chains on adsorbing surfaces. *Journal of Chemical Physics*, 125: 214702, 2006.

[150] C. L. Ting and M. Müller. Membrane stress profiles from self-consistent field theory. *The Journal of Chemical Physics*, 146:104901, 2017.

[151] M. F. Siliakus, J. van der Oost, and S. W. M. Kengen. Adaptations of archaeal and bacterial membranes to variations in temperature, ph and pressure. *Extremophiles*, 21(4):651–670, 2017.

[152] J. H. Lin and A. Baumgaertner. Stability of a melittin pore in a lipid bilayer: a molecular dynamics study. *Biophysical Journal*, 78:1714–24, 2000.

[153] N. B. Last, D. E. Schlamadinger, and A. D. Miranker. A common landscape for membrane-active peptides. *Protein Science*, 22:870–82, 2013.

[154] M. A. Karal, J. M. Alam, T. Takahashi, V. Levadny, and M. Yamazaki. Stretch-activated pore of the antimicrobial peptide, magainin 2. *Langmuir*, 31:3391–3401, 2015.

[155] M. B. Jackson. The journal of membrane biology. *Extremophiles*, 231:101–15, 2009.

[156] Z. Wang and D. Frenkel. Pore nucleation in mechanically stretched bilayer membranes. *The Journal of chemical physics*, 123:154701, 2005.

[157] S. A. Akimov, P. E. Volynsky, T. R. Galimzyanov, P. I. Kuzmin, K. V. Pavlov, and O. V. Batishchev. Pore formation in lipid membrane i: Continuous reversible trajectory from intact bilayer through hydrophobic defect to transversal pore. *Scientific Reports*, 7:12152, 2017.

[158] C. L. Ting, N. Awasthi, M. Müller, and J. S. Hub. Metastable prepores in tension-free lipid bilayers. *Physical review letters*, 120:128103, 2018.

[159] B. Widom. Some topics in the theory of fluids. *J Chem Phys.*, 39:2808, 1963.

[160] S. Kumar. *Computer Simulation of Polymers.* Longman Scientific, Harlow, UK, 1994.

[161] J. I. Siepmann. A method for the direct calculation of chemical potentials for dense chain systems. *Mol. Phys.*, 70:1145, 1990.

[162] D. Frenkel and B. Smit. Unexpected length dependence of the solubility of chain molecules. *Mol. Phys.*, 75:983, 1992.

[163] S.K. Kumar, I. Szleifer, and A.Z. Panagiotopoulos. Determination of the chemical potentials of polymeric systems from monte carlo simulations. *Phys. Rev. Lett.*, 66:2935, 1991.

[164] S.K. Kumar. A modified real particle method for the calculation of the chemical potentials of molecular systems. *J Chem Phys.*, 97:3550, 1992.

[165] M. Müller and W. Paul. Measuring the chemical potential of polymer solutions and melts in computer simulations. *J Chem Phys.*, 100:719, 1994.

[166] N. B. Wilding, M. Müller, and W. Paul. Accurate measurements of the chemical potential of polymeric systems by monte carlo simulation. *J Chem Phys.*, 101: 4324, 1994.

[167] A. Grafmüller, R. Lipowsky, and V. Knecht. Correlations in simulated model bilayers. *Physical Chemistry Chemical Physics*, 15:871–81, 2013.

[168] D. P. Tieleman and S. J. Marrink. Lipids out of equilibrium: Energetics of desorption and pore mediated flip-flop. *Journal of the American Chemical Society*, 128:12462–12467, 2006.

[169] N. Sapay, W. F. D. Bennett, and D. P. Tieleman. Thermodynamics of flip-flop and desorption for a systematic series of phosphatidylcholine lipids. *Soft Matter*, 5:3295–3302, 2009.

[170] W. F. Drew Bennett, J. L. MacCallum, and D. P. Tieleman. Thermodynamic analysis of the effect of cholesterol on dipalmitoylphosphatidylcholine lipid membranes. *Journal of the American Chemical Society*, 131:1972–1978, 2009.

List of Figures

1.1 Scheme of the model for the cell membranes suggested by Robertson 1959 [8] and Danielli et. al. 1935 [9]. Adapted from Robertson 1959. 2

1.2 Schematic representation of the fluid mosaic model showing phospholipids and proteins. Inspired by Singer et. al. 1972 [12] 3

1.3 *Top left*: A typical phospholipid containing head group represented by R_1 connected with glycerol molecule and two fatty alkane chains, represented by R_2 and R_3 connected with other two alcohol sites of the glycerol molecule. *Top right*: Examples of typical head groups *Bottom*: Examples of typical alkane chains. A more detailed review of the structure of the phospholipids can be found in Heimburg 2007 [15]. 4

1.4 Active transport proteins working against the concentration gradients by consuming energy. Adapted from Demarche et. al. 2011 [19] 5

1.5 The schematic diagram of the cargo transport through a membrane without the protein channels. *Left Panel*: Passive diffusion *Right Panel*: Active transport. Active transport without protein channels include processes like endocytosis and exocytosis 5

1.6 Passive transport in the direction of gradient (a) Passive transporter proteins (b) Voltage-gated ion channel (c) Ligand-gated ion channel (d) Mechanosensitive ion channel. Adapted from Demarche et. al. 2011 [19] . 6

1.7 (a) The concentration profile in between two concentration reservoirs with no barrier in between them. (b) The concentration profile when a membrane like barrier is placed in between the reservoirs. The sudden jump in concentration profile at the membrane interface is theoretically explained by the adsorption of solutes at the interface. However, a more gradual increase has been observed in experiments. 7

1.8 The density profiles of head, tail and water monomers in a self assembled membrane simulated using the bond fluctuation model, Chapter 2. The profiles are shown for a membrane at a tensionless state. 8

1.9 The four region model presented by Marrink et. al. 1994 [29]. The y axis represents the free energy of the water molecule at different positions normal to of membrane. Adapted from Marrink et. al. 1994 [29]. 11

1.10 Schematic diagrams of model systems related to the thesis. These systems have been studied in fundamental experimental studies to simplify the membrane related problems. *Left Panel*: A supported bilayer with substrate. *Right Panel*: Unilamellar Vesicles. Source: Wikipedia (public domain) 13

1.11 Coarse-grained model (a) by Shelley et. al. 2001 [41], absorbing $3CH_2$ into a single bead. (b) By Marrink et. al. 2004 [42] absorbing $4CH_2$ into a single bead. (c) By Ayton et. al. 2009 [43] absorbing all phospholipid into a single bead. Adapted from Ingólfsson et. al. 2014 [44] 14

2.1 Schematic representation of monomers as cubes on a simple cubic lattice in the bond fluctuation method. The thick black line connecting the cubes represents a bond. The green arrows denote where moves are possible for a certain monomer on the lattice and the black arrows represent where they are forbidden because of one of the two constraints, i.e. either the bond vectors or the excluded volume. 19

2.2 Schematic representation of the implementation of hydrophobic effect via nearest neighbour repulsion in a two-dimensional BFM. In this figure, the double-headed arrows represent the number of the nearest neighbour interactions between various monomers. 21

2.3 The schematic diagram of lipid structure showing 3 head monomers and two tails with 5 tails monomers each, $L_t = 5$, introduced by Werner et. al. 2012 [54]. The h_2 is the head monomer which is connected both the tails. This monomer is relevant for the discussion in section 2.3 and section 3.6. 22

2.4 Simulation snapshots showing the self-assembly of 300 lipids into a bilayer at 3×10^6 MCS after starting with a random configuration at 0 MCS in a periodic box of $64l \times 64l \times 64l$. The solvent has been made invisible for convenience. 23

2.5 The geometry of a polymer chain molecule. Monomer 1 is on the plane A and monomer 4 is on the plane B, whereas monomer 2 and 3 lie on the line formed by the intersection of planes A and B. r is the bond length, θ is the bending angle formed by monomers 2, 3 and 4 and ϕ is the torsional angle formed by monomers 1, 2, 3 and 4. 24

2.6 The implementation of the bending potential on a polymer chain in the MC simulations. Different bending angles are affected, depending on which monomer has been randomly chosen to be moved. (a) The monomer chosen is at the end of the chain. (b) The monomer chosen is at a position at one adjacent from the end of the chain. (c) The monomer chosen is neither at the position in (a) or (b). The red arrows show the chosen monomer and green arrows show the bending angles which would be affected. 25

2.7 Schematic diagram showing the orientational vector used in Eq.(2.14). . 27

2.8 Variance of internal energy $\langle (U - \langle U \rangle)^2 \rangle$ as a function of bending potential magnitude, k_{bend}. The vertical red indicates the k_{bend} at which the phase transition occurs. 28

2.9 Bond order parameter as a function of bending potential magnitude, k_{bend}. The vertical dashed red line indicates the k_{bend} at which the phase transition occurs. 28

2.10 Diffusion constant of lipids as a function of bending potential magnitude, k_{bend}. The vertical dashed red line points indicates the k_{bend} at which phase transition occurs. 29

3.1 Simulation snapshots showing different states that membrane can assume depending on N_{lipids} in a constant projected area. (a) $N_{lipids} = 250$ (b) $N_{lipids} = 318$ (c) $N_{lipids} = 330$. Length of tails, $L_t = 5$. The solvent is not shown. 33

3.2 The schematic representation of the surface and the local angles it forms with xy plane. The R_1 and R_2 are the radii of two circles formed by the surface at an arbitrary point along the principal directions which are x and y axis in this case. The dotted circle is perpendicular to the plane of the paper. The tangents along these directions are denoted by red arrows. The θ is the angle formed by the local surface tangent with xy plane. . . 34

3.3 Spectral intensity, $\langle Z(q)^2 \rangle$, as a function of wave number, $\mathbf{q}$, for different values of a_f. The legends are in order of decreasing a_f, thus, are also with decreasing stress. The tensionless state is at $a_f = 24.38l^2$ shown with black filled symbol, and the continuous black line shows the best fit of $\langle Z(q)^2 \rangle$ obtained from simulation with the Eq.(3.13) at the tensionless state. The fit parameters give the values of $\gamma_{fluc} \simeq 0$ and $\kappa \simeq 1.3k_BT$. The value of γ_{fluc} and κ for different values of a_f can be found in Fig.(3.4) and Fig.(3.5) respectively. The length of tail has been chosen as $L_t = 4$. . 37

3.4 (a) Fluctuation tension as a function of area per lipid imposed by frame, a_f and L_t. The dark red vertical dashed lines point to the a_f where $\gamma_{fluc} \to 0$ (tensionless state), $a_{f,0}$. The black dashed line shows the linear behaviour of γ_{fluc} with a_f. The lines have been generated by least square fits for linear polynomial with the simulation data (only considering points which are $a_f > a_{f,0}$). (b) γ_{fluc} as a function of area expansion with respect to the tensionless state for each L_t respectively. The dashed black lines are best linear fits for all simulations the above the tensionless state. The magnitudes of slopes of these lines represent the area compressibility, K_A. 38

3.5 Bending rigidity, κ, as a function of the a_f for different length of tails, L_t. The black vertical dashed lines represent the tensionless state $a_{f,0}$. The horizontal lines represent the average of κ considering only points which are at $a_f > a_{f,0}$. 38

3.6 The stress profiles with different components, $-\tau_n$ and τ_t as a function of the distance from the midplane for $L_t = 5$ at different a_f compared to the tensionless state, $a_{f,0}$. The plots with dotted lines above x axis (positive) represent $-\tau_n$, solid lines below x axis (negative) represent τ_t and dashed lines in the middle represent a measure of anisotropy of the stress, $\tau_t - \tau_n$. The colors represent different tensions of the membrane. The blue color represents the membrane at a positive tension, $a_f > a_{f,0}$, red color represent the tensionless state, $a_f \simeq a_{f,0}$, and green color represent the membranes at a negative tension, $a_f < a_{f,0}$. The inset on right lower side shows results from molecular simulations by Goetz et. al. 1998 [102] available at http://www.mpikg.mpg.de for a tensionless state. This image shows the effect on stress profiles by considering Lennard Jones interactions between water-tail and tail-head monomers which is similar to nearest neighbour interaction in BFM. 42

3.7 (a) $\tau_t - \tau_n$ profiles enlarged from Fig.(3.6) at different stresses close to tensionless state, here $a_f = 25.76l^2$ is tensionless state and thus, $a_f = 24.82l^2$ has a_f slightly smaller than tensionless state and $a_f = 27.12l^2$ is at the a_f slightly larger than tensionless state. (b) $\tau_t - \tau_n$ profiles close to the pore stabilisation state, $a_{f,\text{pore}}$(see text), $a_f = 31.75l^2$ is at $a_{f,\text{pore}}$, $a_f = 32.77l^2$ is slightly larger than $a_{f,\text{pore}}$ and $a_f = 29.467l^2$ is slightly smaller than $a_{f,\text{pore}}$ 42

3.8 (a) The mechanical tension as a function of area per lipid imposed by frame, a_f, and L_t. The dark red vertical dashed lines points to the a_f where $\gamma_{mech} \to 0$ (tensionless state), $a_{f,0}$. The grey dashed line shows the area of pore state stabilisation, $a_{f,\text{pore}}$. (b) γ_{mech} as a function of area expansion with respect to the tensionless state for different L_t. The dashed black lines are best linear fits for all the points on x-axis as are considered in Fig.(3.4). The magnitudes of slopes of these lines represent the area compressibility, K_A. 43

3.9 The plots showing the comparison between γ_{fluc} and γ_{mech} for different L_t. The open blue circles represent γ_{fluc} and closed green represent the γ_{mech}. 44

3.10 The plots show the collapse of data via the transformations of the form $\gamma_{mech} = C_1\gamma_{fluc} + C_2$ (see text) for different L_t. The grey lines show the old positions of tension as can be observed in Fig.(3.9). For $L_t = 4$, the transformation has been done from old γ_{fluc} (grey line) to the $C_1\gamma_{fluc}+C_2$ (open red circles). In this case $C_1 = \langle A \rangle / A_f$ chosen from Eq.(3.25) and $C_2 = -0.005k_BT/l^2$. A similar value of C_1 has been chosen for $L_t = 5$ and $L_t = 7$, open black circles represent $C_1\gamma_{fluc}$ for these L_t. The old values of γ_{mech} is for $L_t = 5$ and $L_t = 7$ are shown by the grey lines. The transformation $\gamma_{mech} - C_2$ is shown by closed green dots for $L_t = 5$ and $L_t = 7$. The value of $C_2 = 0.01k_BT/l^2$ for $L_t = 5$; and $C_2 = 0.017k_BT/l^2$ for $L_t = 7$. 45

3.11 (a) The schematic diagram showing the force balance required at a small area element, dA. (b) The representation shows the difference in the confinement of tails in a general situation with area a, and in the reference state in which tail chains are maximally extended with area a_{ext}. 47

3.12 (a) Internal energy per lipid, U_{lipid}, considering only the tail and solvent contacts, as a function of a_f for different L_t. The vertical dashed lines represent the tensionless state, $a_{f,0}$. (b) U_{lipid} as a function of real area per lipid, a_l. 49

3.13 The blue dots represent the $\partial U_{lipid}/\partial a_l$ and red dots represent the γ_{mech} (see Eq.(3.42)) for different L_t. The value of $\partial U_{lipid}/\partial a_l$ is calculated by finding the slope of curves in Fig.(3.12(b)). The yellow fit curves corresponds to the finding best fits of K in Eq.(3.42). The value of K obtained for the fits for $L_t = 4$ is 0.24, $L_t = 5$ is 0.1 and $L_t = 7$ is 0.094. 50

3.14 The schematic diagram showing the contribution of interaction and entropic part to the free energy of lipids tail in the membrane in the case of (a) $a_f < a_{f,0}$; entropic free energy is larger than interaction free energy (b) $a_f \simeq a_{f,0}$; entropic free energy almost balances the interaction free energy (c) $a_f > a_{f,0}$; interaction free energy is larger than entropic free energy. 51

3.15 The solvent permeability as a function of the tail chain length L_t and a_f. The horizontal black dashed lines represent average of P_s for different L_t, where the P_s changes less than 10% of its value near the tensionless state. The range of a_f where P_s is constant with respect to a_f, $\Delta a_{f,P_s=c}$, is indicated by double headed arrows for $L_t = 4$ and $L_t = 7$. Similarly, the range of a_f where P_s changes non linearly with a_f, $\Delta a_{f,P_s \neq c}$, has been also indicated with double headed arrows for the same L_t. The vertical orange line represent the position of $a_{f,\text{pore}}$ for all the L_t. 53

3.16 The fraction of lattice sites occupied by lipid monomers (heads + tails) in the plane of membrane (xy plane) as a function of distance from the midplane of the membrane (z direction). The presented graphs are for the membranes at different stresses (i) $a_f = 25.76l^2$ (red curve) is close to the tensionless state (ii) $a_f = 27.12l^2$ (blue curve) and $a_f = 29.05l^2$ (green curve) have increasing a_f (stress), but they are in the region $\Delta a_{f,P_s=c}$ (iii) $a_f = 30.8l^2$ (yellow curve) has the highest stress but is in region $\Delta a_{f,P_s \neq c}$ (see text). The value of L_t is chosen to be 5. 54

3.17 Membrane thickness as a function of the a_f and tail length. The black vertical dashed lines point to the tensionless state, $a_{f,0}$. The dark red dashed line shows the area of pore state stabilisation, $a_{f,\text{pore}}$. 55

3.18 The schematic diagram showing membrane at different a_f with respect to $a_{f,\text{pore}}$. The membrane thickness decreases from $a_f > a_{f,\text{pore}}$ to $a_f = a_{f,\text{pore}}$. The pore stabilizes at $a_f > a_{f,\text{pore}}$, thus, the solvent is filled in the pore. This increases the membrane thickness. 56

4.1 The schematic diagram of various models for the interaction of different kind of antimicrobial peptides with the membranes. (a) Barrel stave model (b) Toroidal pores (c) Carpet model (see text). The figure on the *right panel* shows the approximations of a helical AMP structure into a solid cylinder structure in the coarse-grained simulations by Illya et. al. 2008 [126]. 62

4.2 *Top panel*: The schematic diagram showing coarse-graining (section 1.3) of copolymers of phenylene ethylene backbones (*first*) and polynorbornene derivatives (*last two*) (synthesised by Gaberiel et. al. 2009 [143]) to the generic copolymers used in the BFM based simulations. In the *lower panel*: The schematic representation of the interaction model for lipids (h, t), solvent (s), and amphiphilic copolymers (*SG*, *BG*). 64

4.3 The probability distribution, $\mathcal{P}(P_s)$ of solvent permeability, P_s, in the interaction with different type of the copolymers with the membrane in system A. These plots show the effect of copolymers of type-1 and type-2 on $\mathcal{P}(P_s)$ of solvent permeability in comparison with $\mathcal{P}(P_s)$ of the bare membrane. The bell shaped peak at the higher values of P_s ($P_s \gg 0$) represents the presence of a pore. As one can observe, type-1 enhances the pore formation and whereas type-2 suppresses it. The length of the copolymer was chosen to be 7. 66

4.4 The snapshots of the two types of the copolymers simulated in a pure solvent environment. The red monomers are hydrophobic and the yellow monomers are hydrophillic, see Fig.(4.3), semi transparent blue monomers represent explicit solvent. Type-1 mostly stay as single copolymers, however type-2 form micelles. $N_p = 100$ for presented snapshots. The length of the copolymer was chosen to be 7. 66

4.5 The average association number calculated using Eq.(4.5) from the simulations of type-1 and type-2 in the pure solvent environment. The fit functions have been calculated from the Eq.(4.7) and Eq.(4.6) using values of x described in legend. The length of the copolymer was chosen to be 7. 68

4.6 The model for the membrane characterized by the fixed area of frame, A_f; the area of pore, A_p; the line tension, α; the area of interface, A_i; the surface tension, γ_{surf}; the chain extension constant, K; and the width of the membrane, w. 69

4.7 Potential of mean force versus radius of the pores as function of the length of the copolymers and the area of frame per tail (filled circles) and the fitted curves (orange lines). (a) system A, $a_f = 31.5l^2$, $L = 7$; (b) system A, $a_f = 31.5l^2$, $L = 11$; (c) system B, $a_f = 30.34l^2$, $L = 7$; (d) system B, $a_f = 30.34l^2$, $L = 11$. 73

4.8 (a) Line tensions in systems A and B as functions of the number of copolymers in the simulation volume. The values of line tension have been calculated using least square fits of the of free energy plots, Fig. 4.7 with Eq.(4.15). The dashed lines corresponds to the best fits to Eq.(4.13) (b) A snapshot of an open pore state for system A with $N_p = 40$ and $L = 7$. The color scheme used for different monomer types is same as in Fig. 4.2. Solvent has been made invisible for convenience. 75

4.9 Probability for a point of the membrane to belong to a pore with the centroid of the pore at the origin as a function of the number of copolymers in the box. The color at coordinates (x, y) represents the probability (see colorbar) of finding a lattice point in a tail free region. These color plots are for system A (larger tension). The length of copolymers is chosen to be 7. 76

4.10 Probability for a point of the membrane to belong to a pore with the centroid of the pore at the origin as a function of the number of copolymers in the box. The color at coordinates (x, y) represents the probability (see colorbar) of finding a lattice point in a tail free region. These color plots are for system B (low tension). The length of copolymers is chosen to be 7. 77

4.11 2-Dimensional pair correlation function between the centroid of the pore and the center of mass of the copolymers within a thin region in the proximity of the membrane surface. The value of unity (colorcode) corresponds to the natural appearance of copolymers in the proximity of the closed membrane. The plots presented are for system A (high tension). The length of copolymers is chosen to be 7. 79

4.12 2-Dimensional pair correlation function between the centroid of the pore and the center of mass of the copolymers within a thin region in the proximity of the membrane surface. The value of unity (colorcode) corresponds to the natural appearance of copolymers in the proximity of the closed membrane. The plots presented are for system B (low tension). The length of copolymers is chosen to be 7. 80

4.13 (a) Average rescaled permeability of solvent for system A and for system B in (b), P_s as a function of N_p. These permeabilities are rescaled with respect to the solvent permeability of bare membranes, i.e. $P_s(0)$. The solvent permeability is the measure of the number of solvent monomers passing from one side of the membrane to the other side per MCS as described in the text. 81

A.1 The schematic diagram of the ghost chain method for the calculation of the chemical potential. The chain on the left (with the solid boundaries) is a real chain of a polymer system and on the right (with the dotted boundaries) is the ghost chain. 91

A.2 (a) The snapshot from simulations showing the presence of ghost lipid without the periodic box for ghost lipid. (b) Same snapshot in (a) with ghost lipid periodic box implemented. System parameters, $L_t = 5$, $N_{lipids} =$ 300 and 1 ghost lipid. 93

A.3 Plot showing the change in the chemical potential with change in area per frame, a_f. The vertical dashed line shows the formation of the pore. 94

List of Tables

3.1 The table showing the values of area per lipid enforced by frame at which tensionless state exists, $a_{f,0}$, slope of γ_{fluc} vs a_f curve, $\partial\gamma_{fluc}/\partial a_f$, bending modulus, κ, and area compressibility, K_A, for membrane with different L_t (see text). 37

4.1 Parameters applied when fitting Eq.(4.12) to simulation data (see text). . 72

Erklärung

Hiermit versichere ich, dass ich die vorliegende Arbeit ohne unzulässige Hilfe Dritter und ohne Benutzung anderer als der angegebenen Hilfsmittel angefertigt habe; die aus fremden Quellen direkt oder indirekt übernommenen Gedanken sind als solche kenntlich gemacht. Die Arbeit wurde bisher weder im Inland noch im Ausland in gleicher oder ähnlicher Form einer anderen Prüfungsbehörde vorgelegt.

Die Arbeit wurde angefertigt unter Betreuung von Prof. Dr. Jens-Uwe Sommer am Leibniz-Institut für Polymerforschung Dresden e.V., Hohe Strasse 6, 01069 Dresden.

Es haben betreffend meiner Person keine früheren erfolglosen Promotionsverfahren stattgefunden.

Weiter erkläre ich hiermit, dass ich die Promotionsordnung vom 23.02.2011 der Fakultät Mathematik und Naturwissenschaften der Technischen Universität Dresden anerkenne.

Ankush Checkervarty